

A lipid-based parallel processor for chemical signals

Idil Cazimoglu

New College

University of Oxford

A thesis submitted for the degree of

Doctor of Philosophy

2021

Acknowledgements

Countless people have paved this path that I am walking - some no longer with us. I am deeply grateful to each and every person.

Prof Hagan Bayley and Dr Michael Booth have trained me to become an independent scholar. I appreciate their time and guidance. In addition, Dr Michael Booth taught me many of the techniques used in this work and has been a constant source of support throughout the years for which I am deeply grateful.

I also thank Bayley and Booth groups who provided company in and outside the lab. In particular, I thank Dr Alessandro Alcinesio for insightful discussions, contact angle analyses and assistance with fluorescence microscopy.

I was able to carry out the work in this thesis thanks to funding by the University of Oxford, the EPSRC & BBSRC Centre for Doctoral Training in Synthetic Biology, the Clarendon Fund Scholarship, and the Oxford-Broomhead Graduate Scholarship from New College. I extend my thanks to Sophie Nixey, Prof Antonis Papachristodoulou and Prof Robert Carlisle for their help.

To my family who have supported me throughout the years, thank you. Your sacrifices have made this possible.

I thank my friends in Oxford for the enjoyable times together, and my friends away from Oxford for being there for me even when we are physically apart.

Finally, I am thankful to my examiners Prof Eleanor Stride and Prof Friedrich Simmel for their time and valuable comments.

Abstract

A key goal of drug delivery and bottom-up synthetic biology is to construct structures that interact with their environment. Biological cells and tissues can process several external chemical signals, often in parallel, without cross-talk. However, so far, cell- and tissue-like structures with only one signalling pathway have been generated. Here, using lipid-bounded aqueous compartments, we build a three-compartment processor with an architecture analogous to that of dual-core central processing units. Each compartment is optimised for a distinct task such as signal transmission, sensing, and enzymatic processing. Recombinantly generated pore-forming membrane protein alpha-hemolysin in the signal transmission compartment enables fast exchange of chemicals between the processing compartments and the external environment. The processor can receive two chemical signals from the environment, process them orthogonally, and produce an output for each signal. The output can be fluorescence or the production and release of a molecule into the external environment. We build the processor from the bottom up, in a modular fashion. In two compartment processors containing a signal transmission compartment and another compartment of varying contents, we demonstrate signal release, signal intake, enzymatic DNA cleavage and enzymatic hydrolysis. We then combine various compartments to build three-compartment processors able to process chemical signals in parallel.

Contents

List of Figures iii

List of Tables v

List of Abbreviations vii

1 Introduction 1
- 1.1 Synthetic compartment models . . . 2
- 1.2 Lipid-based structures . . . 6
  - 1.2.1 Single-compartment structures . . . 6
    - 1.2.1.1 Drug delivery vehicles . . . 6
    - 1.2.1.2 Synthetic cell mimics . . . 8
  - 1.2.2 Multi-compartment structures . . . 10
    - 1.2.2.1 Structures in oil . . . 10
    - 1.2.2.2 Structures in water . . . 13
- 1.3 Design of a lipid-based parallel processor . . . 18
- 1.4 Thesis scope and summary . . . 20

2 Fast molecular diffusion through α-hemolysin heptamerised in situ 23
- 2.1 Introduction . . . 23
- 2.2 Purification of αHL . . . 25
  - 2.2.1 Purification using a centrifugal filter device . . . 25
  - 2.2.2 Fast Protein Liquid Chromatography (FPLC) Purification . 30
- 2.3 Fast molecular diffusion through αHL heptamerised in situ . . . 33
- 2.4 Effect of fatty acyl chain branching on in situ αHL heptamerisation 34
- 2.5 Additional observations on molecular diffusion through αHL heptamerised in situ . . . 36
- 2.6 Additional considerations on molecular diffusion across DIBs . . 38
  - 2.6.1 Diffusion between compartments . . . 38
  - 2.6.2 Effect of DIB size . . . 41
  - 2.6.3 Effect of compartment size . . . 42
  - 2.6.4 Estimation of αHL pore number and density . . . 44
- 2.7 Conclusion . . . 46

3 Exchange of chemical signals with the external environment 49
3.1 Introduction . . . 49
3.2 Signal release to an external aqueous environment by two-compartment structures . . . 50
3.3 Signal intake and sensing from an external aqueous environment by two-compartment processors . . . 51
3.4 Conclusion . . . 54

4 Two-compartment processors 55
4.1 Introduction . . . 55
4.2 Enzymatic process with a fluorescence output: DNA cleavage . . . 56
4.2.1 Reaction design . . . 56
4.2.2 Reaction tests in bulk . . . 58
4.2.3 Encapsulation in two-compartment processors . . . 59
4.3 Enzymatic process with a molecular output: Hydrolysis . . . 62
4.3.1 Reaction and product detection . . . 62
4.3.2 Reaction tests in bulk . . . 64
4.3.3 Encapsulation in two-compartment processors . . . 66
4.4 Conclusion . . . 69

5 Three-compartment processors 71
5.1 Introduction . . . 71
5.2 Effect of Ca^{2+} and Mg^{2+} input signals on glucose detection . . . 72
5.3 Orthogonal processing in three-compartment processors . . . 73
5.4 Simultaneous processing by enzymes in three-compartment processors . . . 75
5.5 Conclusion . . . 77

6 Conclusions 79

7 Experimental Details 87
7.1 Materials and Instruments . . . 87
7.2 Compositions of solutions . . . 90
7.3 αHL expression and purification . . . 91
7.4 αHL buffer exchange attempts using centrifugal filtration devices 93
7.5 Formation of DIBs . . . 93
7.6 Formation of processors and processor mimics . . . 93
7.7 Fluorescence output detection and analysis . . . 94
7.8 Glucose detection and analysis . . . 95
7.9 Contact angle measurements . . . 95

7.10 EcoRI assays 96
7.11 Code for Image Analyses 96
7.11.1 Compartment Detection 96
7.11.2 Compartment Measurement 97
7.11.3 Contact Angle Measurement and Fluorescence Analysis . 98

References **103**

List of Figures

1.1 Synthetic compartment models. 3
1.2 Liposomes as drug delivery vehicles. 7
1.3 Liposomes as synthetic cell and organelle mimics. 9
1.4 Droplet interface bilayers (DIBs). 11
1.5 Droplet networks in oil and internal chemical communication. . . 12
1.6 Droplet networks in oil and external signals. 13
1.7 Multisomes. 15
1.8 IVTT expression of αHL-4H and controlled release of multisome contents. 16
1.9 Multi-compartment liposomes. 17
1.10 The three-compartment parallel processor. 19
1.11 Signalling in the three-compartment parallel processor. 20

2.1 SDS-PAGE gel of elutions after His-tag purification of αHL. 26
2.2 SDS-PAGE gels of **α**HL ran through centrifugal filtration columns with cutoff values of 3K and 50K. 27
2.3 SDS-PAGE gels of **α**HL ran through centrifugal filtration columns with cutoff values of 30K with 0.006% w/v or no SDS. 28
2.4 SDS-PAGE gels of **α**HL ran through centrifugal filtration columns with cutoff values of 50K with or without SDS. 29
2.5 SDS-PAGE gels of **α**HL ran through centrifugal filtration columns with cutoff values of 30K, 50K and 100K with 0.06% w/v SDS. . 30
2.6 FPLC trace of αHL purified with size exclusion chromatography. . 31
2.7 SDS-PAGE gel of elutions after an example purification of αHL by size exclusion chromatography. 32
2.8 Fast molecular diffusion through **α**HL heptamerised in DIBs. . . . 34
2.9 Diffusion of 2-NBDG through in-situ heptamerised **α**HL with various lipid conditions. 35
2.10 Molecular diffusion through **α**HL pores followed by mixing inside the receiving compartment. 37
2.11 Simultaneous DIB expansion and molecular diffusion through αHL pores. 38

2.12 Equilibration of a chemical signal between compartments under various scenarios. 39
2.13 Distances in a DIB system. 40
2.14 Effect of bilayer area on the equilibration time of a chemical signal across a DIB permeabilised by αHL. 43
2.15 Effect of compartment size on the equilibration time of a chemical signal across a DIB permeabilised by αHL. 45

3.1 Output of a molecular signal from two-compartment structures to an external aqueous environment. 52
3.2 Intake and sensing of an external ionic signal by two-compartment structures. 53

4.1 Mg^{2+}-activated DNA cleavage by EcoRI with a fluorescence output. 57
4.2 DNA cleavage activity of EcoRI at various pH values, with or without Mg^{2+}. 59
4.3 DNA cleavage activity of EcoRI at various with various concentrations of BSA, with or without Mg^{2+}. 60
4.4 Enzymatic DNA cleavage in two-compartment processors with a fluorescence output. 61
4.5 Fluorescence in the signal transmission compartment after enzymatic DNA cleavage in two-compartment processors. 62
4.6 Enzymatic processing with a molecular output. 62
4.7 Enzymatic conversion of glucose into fluorescent resorufin. . . . 63
4.8 Detection of glucose standards without or with lactose at various pH conditions. 65
4.9 Glucose production by β-galactosidase at various pH values without and with lactose. 66
4.10 Enzymatic hydrolysis in two-compartment processors with a molecular output. 67

5.1 Effect of $CaCl_2$ on detection of glucose standards. 74
5.2 Effect of $MgCl_2$ on detection of glucose standards. 75
5.3 Orthogonal processing of two input signals in three-compartment processors. 76
5.4 Simultaneous enzymatic processing of two input signals in three-compartment processors. 77

6.1 A versatile multi-compartment parallel processor with several processing units. 84
6.2 Self-assembly of a multi-compartment processor mimic with several processing units. 85

List of Tables

2.1 Effect of bilayer area A_{DIB} on 2-NBDG equilibration by diffusion across a DIB permeabilised by αHL, with constant compartment size. 42
2.2 Effect of bilayer area on 2-NBDG equilibration by diffusion across a DIB permeabilised by αHL, with constant compartment size. . . 43

7.1 List of materials and sources. 87
7.2 List of instruments and manufacturers. 89

List of Abbreviations

αHL	α-hemolysin
αHL-4H	Zn^{2+}-sensitive α-hemolysin with residues 123, 125, 133, 135 replaced with histidines
αHL-R104C-CNB	α-hemolysin with residue 104 replaced with cysteine attached to the photocage α-carboxy-2-nitrobenzyl
β-gal	β-galactosidase
θ	Contact angle in a DIB
2-NBDG	2-[*N*-(7-nitrobenz-2-oxa-1,3-diazol-4-yl) amino]-2-deoxy-D-glucose
3D	Three-dimensional
ADP	Adenosine diphosphate
ATP	Adenosine triphosphate
BAPTA	1,2-bis(o-aminophenoxy)ethane-N,N,N',N'-tetraacetic acid
BNPA	2-bromo-2-(2-nitrophenyl)acetic acid
BHQ-3	Black hole quencher-3
BR	Bacteriorhodopsin
BSA	Bovine serum albumin
CNB	α-carboxy-2-nitrobenzyl
CPU	Central processing unit
CUG	3-carboxyumbelliferyl-β-D-galactopyranoside
Cy5	Cyanine 5
d	Diameter of an aqueous compartment
D-gal	D-galactose
DABYCL	4-(dimethylaminoazo)benzene-4-carboxylic acid
DFHBI	3,5-difluoro-4-hydroxybenzylidene imidazolinone
DIB	Droplet interface bilayer

DNA . . . . . Deoxyribonucleic acid

DPhPC 1,2-diphytanoyl-s*n*-glycero-3-phosphatidylcholine

dsDNA . . . . . Double-stranded DNA

EcoRI-HF . . . . . High fidelity EcoRI variant with increased specificity for target sequence

EDTA . . . . . Ethylenediaminetetraacetic acid

EGTA . . . . . Ethylene glycol-bis(β-aminoethyl ether)-N,N,N',N'-tetraacetic acid

FPLC . . . . . Fast protein liquid chromatography

FRET . . . . . Förster resonance energy transfer

GDP . . . . . Guanosine diphosphate

GTP . . . . . Guanosine triphosphate

GUV . . . . . Giant unilamellar vesicle

IPTG . . . . . Isopropyl β-d-1-thiogalactopyranoside

IVTT . . . . . In vitro transcription and translation

L . . . . . Centre-to-centre distance of two aqueous compartments

LacY . . . . . Lactose permease

LB . . . . . Lysogeny broth

LUV . . . . . Large unilamellar vesicle

MMP2 . . . . . Matrix metalloproteinase-2

MES . . . . . 2-(N-morpholino)ethanesulfonic acid

mRNA . . . . . Messenger RNA

MscL . . . . . Large conductance mechanosensitive ion channel

MW . . . . . Molecular weight

n . . . . . Number of repeats for each experiment

NTA . . . . . Nitrilotriacetic acid

PEG . . . . . Polyethylene glycol

PMF . . . . . Proton motive force

PMMA . . . . . Poly(methyl methacrylate)

PNIPAAm . . . . . Poly(N-isopropylacrylamide)

PR . . . . . Proteorhodopsin

PSII . . . . . Photosystem II

R . . . . . Radius of an aqueous compartment

RNA . . . . . Ribonucleic acid

SDS . . . . . Sodium dodecyl sulfate

ssDNA . . . . . Single-stranded DNA

SUV . . . . . Small unilamellar vesicle

TAMRA . . . . . 5(6)-carboxytetramethylrhodamine

Tris . . . . . Tris(hydroxymethyl)aminomethane

UV . . . . . Ultra-violet

w/o/w . . . . . Water-in-oil-in-water

1 Introduction

Contents

1.1 Synthetic compartment models 2
1.2 Lipid-based structures 6
1.2.1 Single-compartment structures 6
1.2.1.1 Drug delivery vehicles 6
1.2.1.2 Synthetic cell mimics 8
1.2.2 Multi-compartment structures 10
1.2.2.1 Structures in oil 10
1.2.2.2 Structures in water 13
1.3 Design of a lipid-based parallel processor 18
1.4 Thesis scope and summary 20

Synthetic aqueous compartments are a versatile platform for building drug delivery vehicles as well as cell- and tissue-like structures. They can be used for protection, targeted delivery and controlled release of drug molecules[1]. Hydrophilic molecules can be encapsulated within synthetic aqueous compartments to prevent their degradation, early activation and dilution in the body[2–5]. Some synthetic aqueous compartments have a hydrophobic membrane which can be used as a carrier for hydrophobic drugs[3]. Synthetic aqueous compartments can be designed to target specific tissues, increasing on-target activity while reducing off-target toxicity of drugs[3]. These compartments can also be engineered to release their contents in a controlled manner through

semipermeable membranes[6,7], passive biodegradation[6–9], or biodegradation upon external triggers such as pH, ultrasound or enzymatic activity on the membrane[6–14]. A slow and sustained release may reduce the drug's toxicity while increasing its efficacy[3,15–17]. In addition, as the drug dosage regimen can be less frequent, it may increase patient compliance[15].

In bottom-up synthetic biology, aqueous compartments serve as the starting point to build cell- and tissue-like structures from simple building blocks[18,19]. Underpinning cellular life is compartmentalisation in terms of both separation of intracellular compartments from the extracellular environment by a lipid bilayer and sub-cellular organisation into membraneless and membrane-bound compartments. Therefore, to build synthetic cell- and tissue-like structures, bottom-up synthetic biology employs compartmentalisation. Even though the field takes inspiration from biological cells, a diverse range of synthetic and natural building blocks are used to build the compartments. Therefore, the engineered compartments do not necessarily mimic those found in nature, but present a plethora of applications such as understanding membrane dynamics and building microreactors and bioinspired devices.

In this chapter, we summarise the most common synthetic compartment models and their applications. We then focus on lipid-based compartments. We first review single-compartment models and their applications in drug delivery and as cell-like structures. We then review multi-compartment structures within external oil and water environments. Finally, we present the design of our lipid-based parallel processor and outline the sections of this thesis.

1.1 Synthetic compartment models

Synthetic aqueous compartments have applications in drug delivery as well as bottom-up synthetic biology. Like biological compartments, synthetic compartments can be categorised into membraneless and membrane-bound compartments.

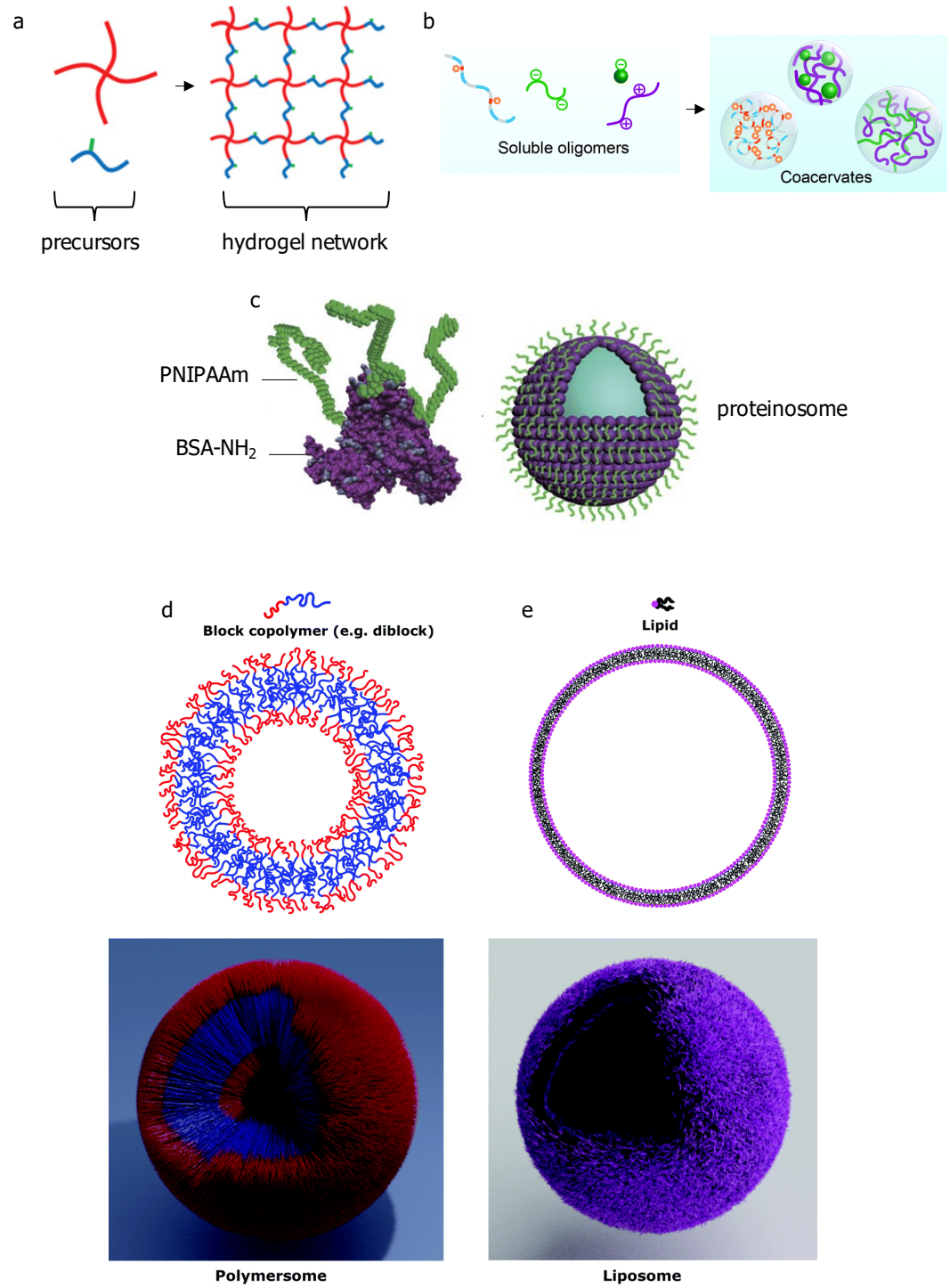


Figure 1.1: Synthetic compartment models. a. Hydrophilic polymer chains (left) are cross-linked to form a meshed hydrogel network (right)[20]. **b.** Soluble oligomers (left) phase separate from the surrounding water due to charge-charge interactions or other attractive interactions, forming coacervates (right)[21]. **c.** Conjugated poly(N-isopropylacrylamide) (PNIPAAm) polymer chains and bovine serum albumin (BSA) (left) self-assemble to generate proteinosomes (right)[22]. **d.** Block copolymers with hydrophilic and hydrophobic groups (top) self-assemble to form polymersomes. Cross-section (middle) and 3D structures (bottom) of polymersomes are depicted[14]. **e.** Amphiphilic lipid molecules (top) self-assemble to form liposomes. Cross-section (middle) and 3D structures (bottom) of liposomes are depicted[14].

Membraneless compartments include hydrogel particles and coacervates. Hydrogel particles are made of 3D networks of cross-linked hydrophilic polymers (Fig. 1.1a)[20]. These particles are highly porous due to the meshes in the polymer network, and can therefore exchange molecules with their environment. The mesh size can range between 5 and 200 nm[23–26]. These large mesh sizes prevent encapsulation of small molecules in hydrogel compartments[27]. Cell-free protein expression has been shown in DNA hydrogels where the cross-linked polymers are DNA encoding for the protein[28,29] or where His-tagged protein expression machinery has been immobilized on a polymer backbone with anti-His-tag aptamer grafts[30]. They have also been generated to contain another hydrogel as a subcompartment and carry out cell-free protein expression in response to molecules generated by different hydrogel compartments[29].

Coacervates form spontaneously due to liquid-liquid phase separation between a condensed and a dilute aqueous phase (Fig. 1.1b)[21]. The phase separation occurs due to attractive interactions between molecules such as polypeptides, polynucleotides, polysaccharides and ATP[31]. Their formation can be regulated by temperature, light and chemical reactions[32]. Coacervates tend to coalesce into larger droplets or exhibit macroscopic phase separation under many conditions, therefore hybrid coacervates with various membranes have also been developed[13,31,33–35].

Membrane-bound compartments are formed by the characteristic self-assembly of amphiphilic molecules into micelles and vesicles, and include liposomes, polymersomes, proteinosomes and hybrid compartments. Proteinosomes are bounded by a closely packed monolayer of protein-polymer conjugates (Fig. 1.1c)[22] where the proteins can also be active enzymes[36]. These compartments have been shown to carry out enzymatic reactions, disassemble upon protease activity[37], and encapsulate sub-compartments to store and release molecules in a hierarchical manner[38]. Using a click reaction, these compartments have also been linked to form multi-compartment structures (prototissues) that contract and expand in response to temperature changes[39]. However, the intrinsic

permeability of these structures is hard to control. The pores allow diffusion of chemicals up to 40 kDa in molecular weight[22], meaning that many small biological molecules would immediately leak into the environment.

Polymersomes are vesicles formed by the self-assembly of block copolymers containing hydrophobic and hydrophilic blocks (Fig. 1.1d)[14,40]. They have been shown to perform enzymatic reactions[41], degrade to release contents as a response to external stimuli[7,14], and encapsulate sub-compartments[42,43]. Block copolymer-stabilized water-in-oil-in-water (w/o/w) double emulsions have been used to form multi-compartment polymersomes[44]. Polymersomes have also been engineered with subcompartments[45]. Polymersome membranes have very low permeability, which limits applications that rely on diffusion of small molecules through the membrane[14]. As polymersome membranes are often too thick, a limited range of natural trans-membrane channels has been incorporated into them[14,46]. For example, three membrane proteins commonly used in synthetic compartments, the pore-forming toxin alpha hemolysin (αHL), mechanosensitive ion channel (MscL) and proton pump bacteriorhodopsin (BR) have transmembrane regions approximately 5 nm[47], 4-5 nm[48,49] and 3 nm[50,51] in length, respectively. On the other hand, polymersome membranes typically range from 5 to 50 nm in thickness[14]. Transmembrane channel proteins OmpF, Tsx, FhuA and complex I have so far been incorporated into single-compartment polymersomes[14,46,52].

Liposomes are formed by the self assembly of lipid molecules to form lipid bilayers (Fig. 1.1e)[14]. The amphiphiles that form cell membranes are lipids. Phospholipids, with a polar phosphate head group and two hydrophobic hydrocarbon tails, are the most abundant membrane lipids. Importantly, cell membranes also contain a plethora of integral and peripheral membrane proteins making up almost 50% of the membrane[53]. Therefore, lipid-based compartments, with the ability to incorporate membrane proteins are of special interest to the fields of drug delivery, biomimetics and synthetic biology. Unlike hydrogels and proteinosomes, lipid-based compartments are not inherently permeable,

enabling encapsulation of drugs[9], reactions[14], and cell-free transcription and translation machinery[54]. On the other hand, unlike polymersomes, lipid-based compartments more readily incorporate membrane channels and pores, allowing for selective passive diffusion and active transport of external chemicals. Unlike coacervates, they are protected with a membrane reducing the coalescence into larger compartments. In addition, lipid-based compartments can both serve as and contain sub-compartments. For example, they have been encapsulated in polymersomes[55] and hydrogels[56], and have been shown to encapsulate other lipid-based compartments[57,58] and coacervates[34].

1.2 Lipid-based structures

1.2.1 Single-compartment structures

Single-compartment aqueous structures can exist within an oil environment, but have limited applications as individual compartments that cannot interact with other compartments or the environment. Therefore, most single-compartment lipid-based structures are interfaced with an external aqueous environment through a lipid monolayer or bilayer. Those with a lipid monolayer are micellar structures that can carry a hydrophobic drug in the middle[59]. Those with a lipid bilayer, termed liposomes, can be unilamellar with a single bilayer or multilamellar with multiple concentric bilayers[60]. Unilamellar liposomes are divided into three groups according to their diameters: small unilamellar vesicles (SUVs) range between 0.02 µm and 0.2 µm, large unilamellar vesicles (LUVs) between 0.2 µm and 1 µm, and giant unilamellar vesicles (GUVs) above 1 µm[61]. Liposomes are often used as drug delivery vehicles and synthetic cell mimics.

1.2.1.1 Drug delivery vehicles

Lipid-based compartments can be engineered to deliver drugs to both extracellular and intracellular targets[62] and several are already in clinical use[3,9,17]. Micellar structures can encapsulate a hydrophobic drug in the middle[59]. Liposomes can

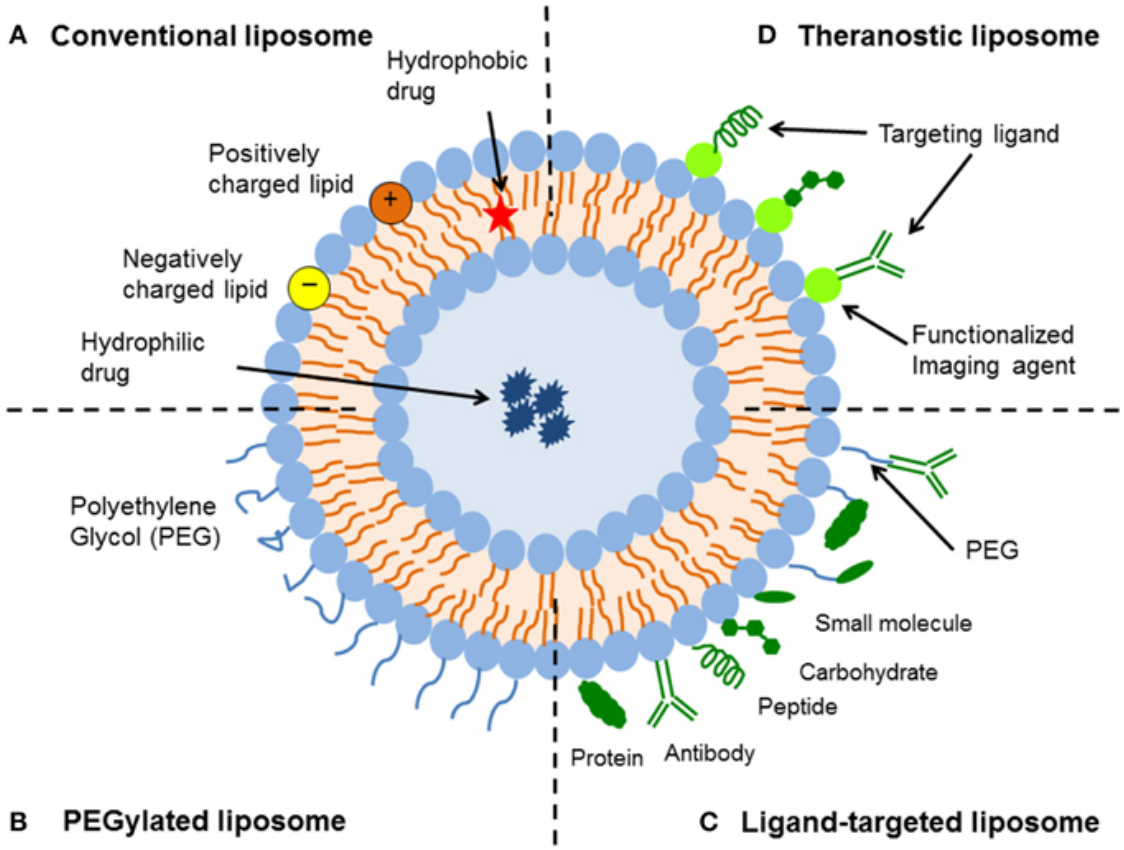


Figure 1.2: Liposomes as drug delivery vehicles. **a.** Conventional liposomes are vesicles with an aqueous core that can carry hydrophilic drugs surrounded by a lipid membrane that can carry hydrophobic drugs[3]. **b.** PEGylated liposomes, with polyethylene glycol grafted on their surfaces, have longer circulation in the body[3]. **c.** Ligands can be attached on liposomes to target drug delivery to specific sites[3]. **d.** Theranostic liposomes carry both therapeutic and diagnostic components[3].

encapsulate drugs in their hydrophilic core and/or hydrophobic membrane (Fig. 1.2)[3]. They often release the encapsulated drugs upon passive biodegradation in vivo[3,9]. Lipid-based drug delivery vehicles mostly accumulate in the liver and spleen as they are cleared from the body by the cells of the reticuloendothelial system[3]. To increase the site specific accumulation of these vehicles, some compartments have also been engineered with ligands that target specific cells and sub-cellular compartments[3,17]. An alternative or addition to site-specific accumulation is site-specific release. Compartments have been engineered to degrade or become permeable upon external triggers, such as temperature and ultrasound, or internal triggers, such as pH and enzymatic activity[3].

Arguably, the most well-known lipid-based carriers as of 2021, are those

that deliver mRNA encoding for the SARS-CoV-2 spike glycoprotein into human cells in vivo[63,64]. Such carriers efficiently encapsulate the therapeutic to protect it from degradation in circulation. They localise at the membrane of the target cells, followed by endocytosis[65]. During endocytosis, part of the cell membrane surrounds the lipid-based carrier, then buds off inside the cell to form an endosome, a vesicle containing the carrier[66]. In the cytosol, the therapeutic escapes both barriers, the lipid-based carrier and the endosome, before carrying out its therapeutic function[65].

1.2.1.2 Synthetic cell mimics

With increasing sophistication, single compartments start approaching synthetic cells in terms of both architecture and function. Lipid-based compartments containing smaller, organelle-like compartments have been generated. The organelle mimics can be membraneless such as coacervates[34,68] or membrane-bound such as other lipid-based compartments[57,58,67,69,70].

Synthetic cell mimics may employ membrane proteins or channels to exchange chemicals with their environment. For example, pore-forming toxin alpha hemolysin (αHL)[70,71] and the lytic peptide melittin[72,73] have been used to release contents from single compartments into their surroundings. Large conductance mechanosensitive ion channel (MscL)[74] variants were reconstituted in single-compartment lipid vesicles to regulate flow of ions or molecules with light[75] chemicals[76], or lipase activity on the lipid membrane[70]. Other membrane proteins and channels such as annexin V[77], a voltage gated K^+ channel[78], and many others[57,67,79–82] including synthetic channels[83,84] have been functionally reconstituted in lipid compartments.

Single compartments have also been shown to activate internal biochemical processes based on receipt of environmental signals. For example, photosynthetic proteins and protein complexes have been incorporated in lipid compartments for light-dependent ATP synthesis[85] which has then been coupled to carbon fixation, actin polymerisation (Fig. 1.3a, b)[57] and protein expression

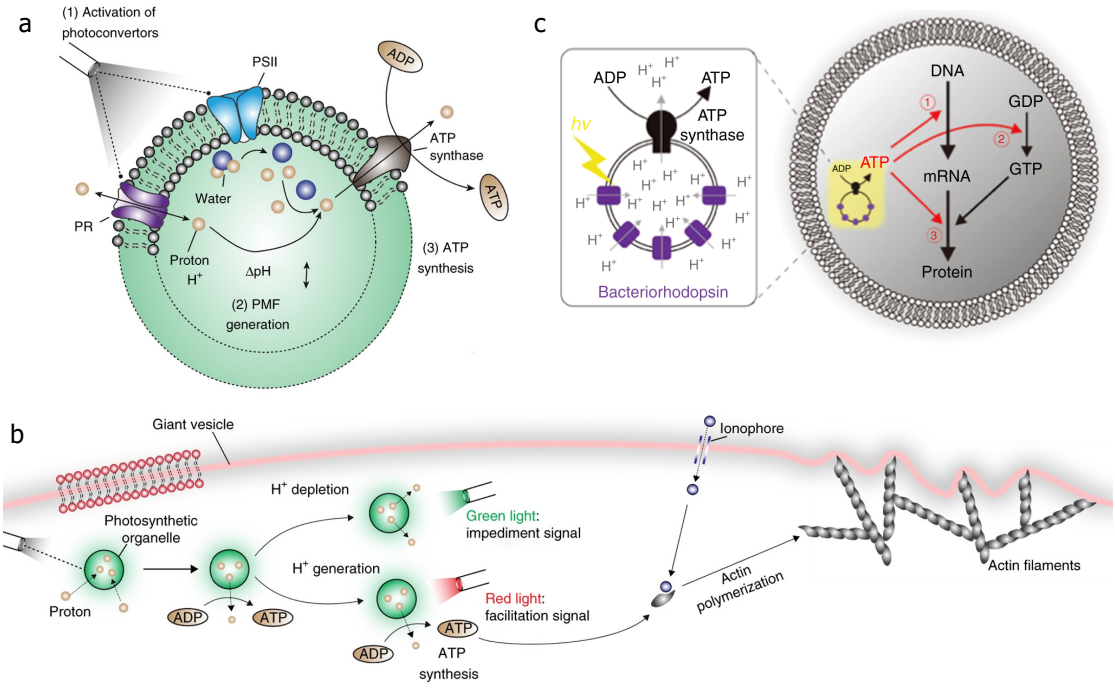


Figure 1.3: Liposomes as synthetic cell and organelle mimics. a. An SUV as an artifical organelle. Upon illumination, the coordinated action of photosystem II (PSII), proteorhodopsin (PR) and ATP synthase converts ADP to ATP[57]. **b.** A GUV as a synthetic cell mimic containing SUVs from (a) as artifical organelles. The encapsulated organelles drive ATP-dependent actin polymerization inside the synthetic cell mimic[57]. **c.** A GUV as a synthetic cell mimic containing SUVs as artifical organelles. Upon illumination, the coordinated action of bacteriorhodopsin (BR) and ATP synthase converts ADP to ATP. The ATP is then used for mRNA production, conversion of guanosine diphosphate (GDP) to guanosine triphosphate (GTP), and protein synthesis inside the cell mimic[67].

(Fig. 1.3c)[67] inside the compartments. A bacterial quorum sensing molecule has been used to initiate the expression of the pore-forming membrane protein perfringolysin O in lipid compartments[86]. A synthetic beta cell mimic has been generated that receives and enzymatically processes glucose from the environment, leading to exocytosis of pre-encapsulated insulin[87]. Synthetic cell mimics that interact with other synthetic cell mimics[88] or with biological cells have also been constructed[86,89].

In addition to signalling and internal processes, simple analogues to other cell-like features, including growth[90], division[90,91] and chemotaxis[90,92] have been demonstrated in lipid compartments.

1.2.2 Multi-compartment structures

Even though most of the drug delivery or cell-like functionalities have been demonstrated in single compartments, multi-compartment structures might carry out more complex functions. For example, a structure with a higher number of compartments can perform a higher number of individual functions encapsulated by each compartment. In addition, these compartments can also exhibit collective properties, thereby acting as synthetic tissues.

1.2.2.1 Structures in oil

Work on multi-compartment structures has mostly been carried out in an external oil environment. Aqueous droplets placed in a lipid-oil external environment become surrounded by a lipid monolayer (Fig. 1.4a). When such droplets are brought together, the monolayers in the middle of each pair of droplets form a droplet interface bilayer (DIB)[98] (Fig. 1.4b). Such multi-compartment structures can be formed by generating and bringing individual droplets together manually or by 3D-printing of individual droplets in close proximity of one another. 3D-printing enables fabrication of networks with thousands of droplets with desired 3D arrangements[94,99]. Networks of droplets have been shown to exhibit collective properties as biobatteries[95], rectifiers[100] or folding structures[94].

Droplet interface bilayers have been functionalised with various membrane proteins and channels to enable communication between two compartments and between the compartments and the environment.

For example αHL has been used to enable diffusion of chemicals across DIBs connecting compartments[93,101,102]. Diffusion of chemical signals across DIBs has been used to engineer complex signalling mechanisms and mediate protein expression in droplet networks (Fig. 1.5)[93]. An MscL variant has been incorporated in DIBs to regulate flow of molecules with a chemical activator[103]. The sugar transporter lactose permease (LacY) has been incorporated into DIBs for active transport of a fluorescent sugar molecule from one droplet to

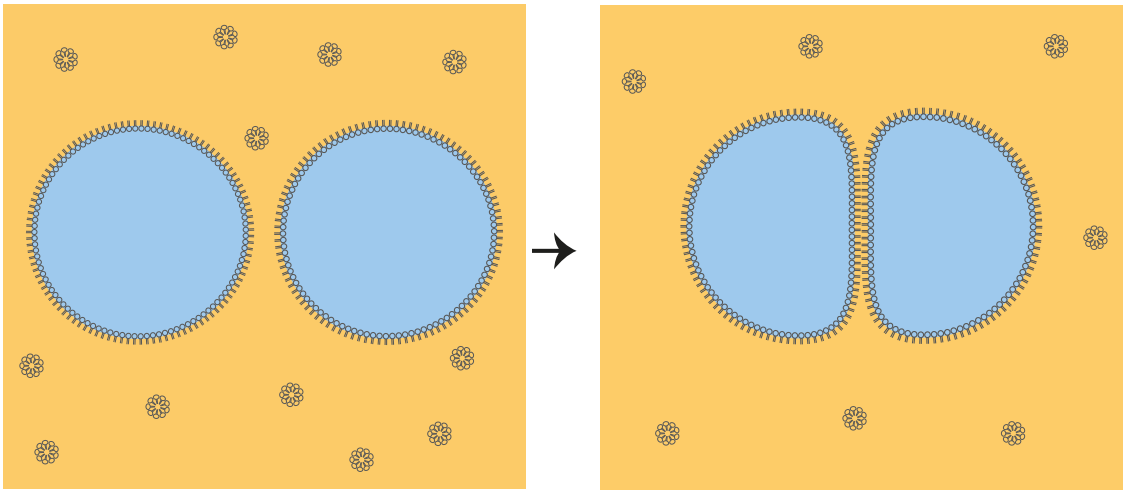


Figure 1.4: Droplet interface bilayers (DIBs). a. When aqueous droplets are placed in lipid-containing oil, a lipid monolayer forms around each droplet. **b.** When two such droplets are brought together, the monolayers in the middle form a lipid bilayer termed droplet interface bilayer.

another[104]. A combination of streptolysin O and αHL have been used to configure a droplet system that computes logic gate operations with DNA[105].

Multi-compartment structures in oil have been shown to receive electrical (Fig. 1.6a), light (Fig. 1.6b,c) and mechanical (Fig. 1.6d) signals from the environment. Variants of αHL[94,95,99,100], MscL[103], and the voltage gated K^+ channels[106,107] have been reconstituted in DIBs and shown to conduct electrical signals upon applied voltage. The proton pump bacteriorhodopsin (BR) has been used to generate light-driven current across the DIBs of droplet networks[95]. Light has also been used to activate protein expression inside droplet networks by removing photocleavable groups from the promoter[98,102].

Mechanical perturbation of a 'hair' in a droplet of a DIB has been shown to change the area of the DIB, and therefore its capacitance, generating current. In this way, a mechanical signal from the environment was converted into an electrical signal[97,108]. A variant of MscL has also been incorporated into DIBs and shown to regulate an external electrical signal based on the axial compressions/decompressions applied on the droplets[109].

Even though multi-compartment structures in oil have been shown to respond to electrical, mechanical and light stimuli from the environment, they cannot

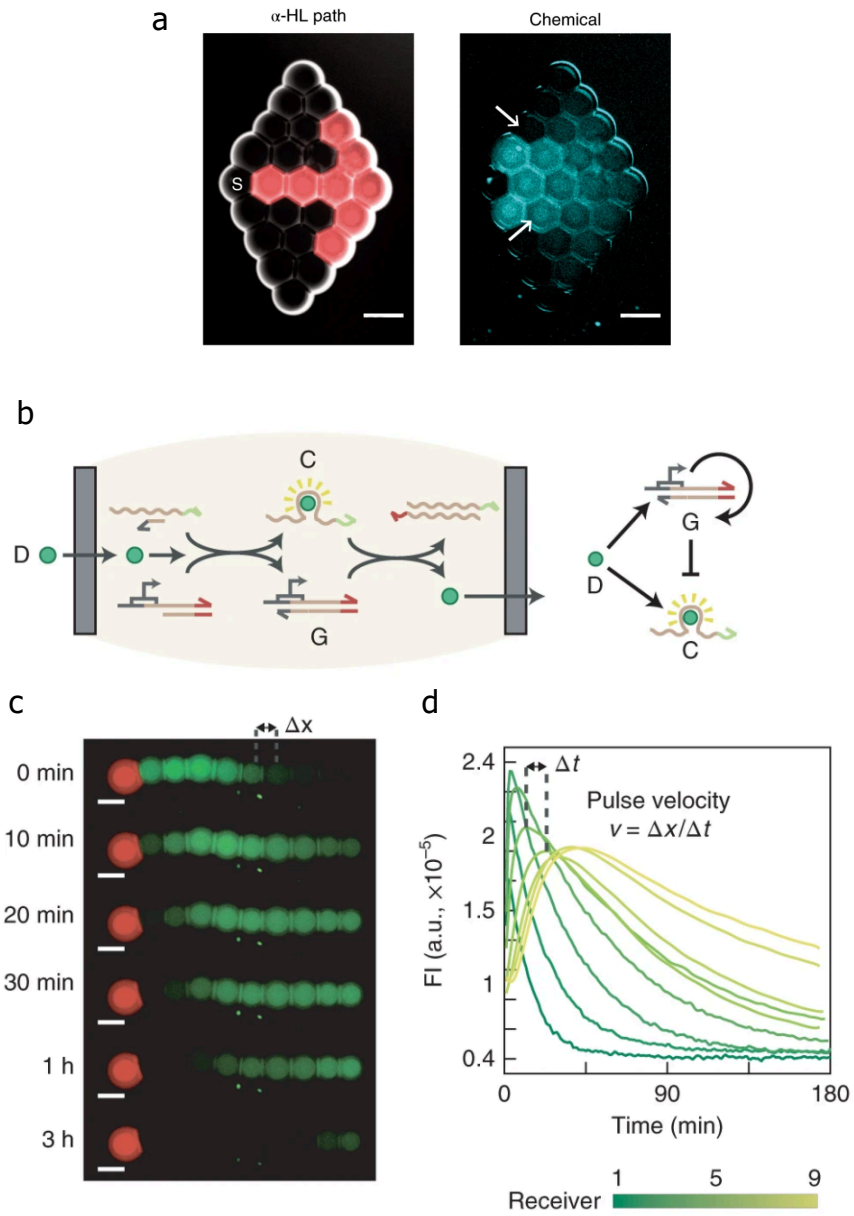


Figure 1.5: Droplet networks in oil and internal chemical communication. **a.** A network of droplets containing αHL along the red path. Guanine from the sender compartment (S) diffuses through the αHL pores into receiver droplets, where it binds a bifunctional aptamer which then binds 3,5-difluoro-4-hydroxybenzylidene imidazolinone (DFHBI), generating fluorescence. Scale bars = 200 μm[93]. **b-d.** Pulse generation by an incoherent feedforward loop circuit in droplet networks. **b.** Each receiver droplet contains an RNA aptamer (curved line) bound to a single-stranded DNA (ssDNA, straight line), and a double-stranded DNA missing a section of one of the strands (dsDNA). DFHBI diffuses through the lipid bilayers, without a need for αHL pores and binds the aptamer, generating fluorescence. The released ssDNA completes the dsDNA, initiating transcription of an antisense-RNA, which then displaces DFHBI from its RNA aptamer, and decreases the observed fluorescence. Therefore, the mechanism acts as an incoherent feedforward loop[93]. **c.** The feedforward loop from b exhibited in a droplet network. Scale bars = 200 μm[93]. **d.** Fluorescence intensity over time in the receiver compartments in c. Pulse velocity v = Δx/Δt where Δx = distance and Δt = time between two pulse maxima[93].

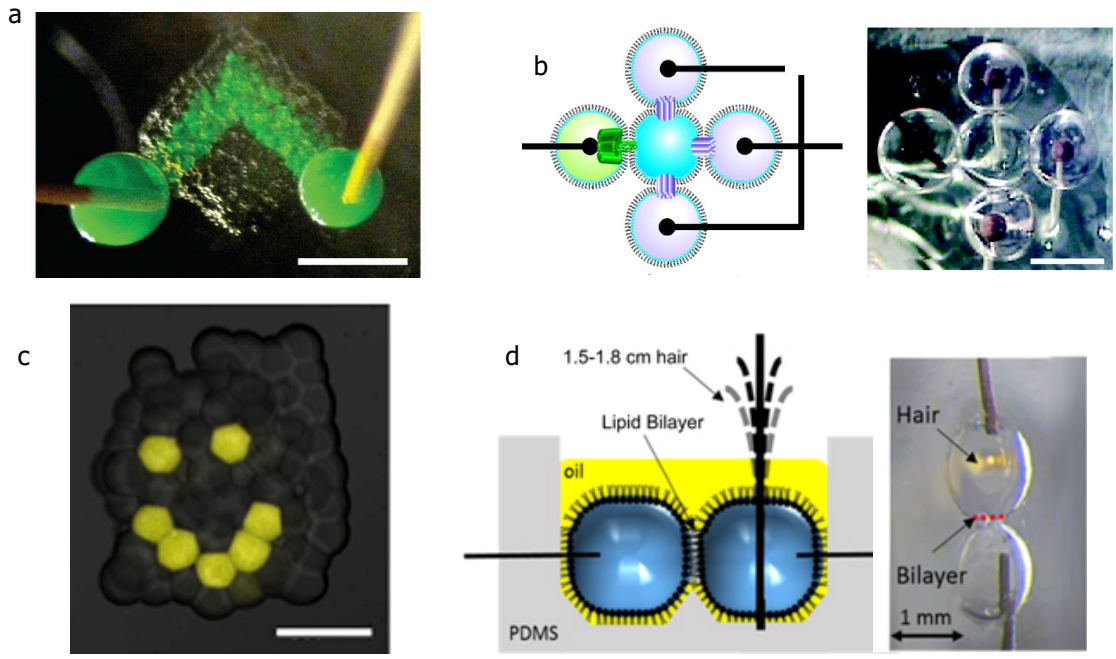


Figure 1.6: Droplet networks in oil and external signals. a. A 3D-printed droplet network with a conductive pathway containing αHL (green droplets and electrode-impaled green drops). Scale bar = 500 µm[94]. **b.** A light-sensing droplet network. Three droplets containing bacteriorhodopsin (BR) (purple) are connected to a central droplet (blue) which is connected to a droplet containing αHL (green). Upon illumination, each BR droplet generates a current which is recorded using electrodes attached to the BR and αHL droplets. Scale bar = 700 µm[95]. **c.** Light-activated fluorescent protein expression in a 3D-printed synthetic tissue. Scale bar = 200 µm[96]. **d.** A DIB that responds to mechanical perturbations of a hair inside one of the droplets. The vibration of the hair changes the DIB area, leading to changes in measured capacitance[97].

exchange water-soluble chemical signals with their environment. To act as drug delivery vehicles or synthetic tissues, or to be interfaced with living tissues, these structures must operate within an external aqueous environment and able to send and receive chemical signals.

1.2.2.2 Structures in water

To overcome limitations of an oil environment, multi-compartment lipid-based structures that operate in water have been engineered. These structures contain bilayers between the compartments as well as bilayers between the compartments and the external water environment.

An early example of a multi-compartment lipid-based structure with an

external aqueous environment is the DepoFoam[9,110]. Drugs pre-loaded in closely-packed lipid compartments are released slowly, by permeation of the through the bilayers and by coalescence of the compartments. More sophisticated multi-compartment structures in water have also been generated: multisomes and multi-compartment vesicles.

Multisomes, aqueous compartments within a lipid-oil drop suspended in an external aqueous environment (Fig. 1.7a) have been generated manually (Fig. 1.7b)[12], by 3D-printing[94] (Fig. 1.7c, d), and by microfluidics (Fig. 1.7e, f)[111]. Multisomes can be supported on a plastic or wire loop[12,112]. αHL has been used to enable transmission of electrical signals and diffusion of Ca^{2+} ions from the external aqueous environment into an internal compartment. Temperature- and pH-sensitive lipids have been used for triggered coalescence of the internal compartments to the external aqueous environment, releasing pre-loaded cargo molecules[12].

Multisomes have also been shown to support protein expression inside the compartments and selective permeabilisation of the internal bilayer with the mutant pore-forming protein αHL-4H (Fig. 1.8)[112]. αHL-4H is a Zn^{2+}-sensitive variant of αHL that is blocked in presence of Zn^{2+} and re-opened when a chelator such as ethylenediaminetetraacetic acid (EDTA) is added to remove the Zn^{2+}[113]. The ability to block and open external αHL-4H pores in this way while keeping the internal pores open has been shown in multisomes (Fig. 1.8a)[112]. To combine this ability with protein expression, multisomes of two compartments were formed and suspended on a Teflon-coated silver wire within an external aqueous environment containing Zn^{2+}. One internal compartment contained the enzyme β-galactosidase along with an in-vitro transcription and translation (IVTT) system and DNA encoding for the αHL-4H, while the other compartment contained the substrate molecule (Fig. 1.8b). Expression of αHL-4H enabled internal diffusion and reaction of the substrate in the enzymatic compartment without leaking of the substrate and product into the external environment (Fig. 1.8c). EDTA was then added to controllably release the product (Fig. 1.8d).

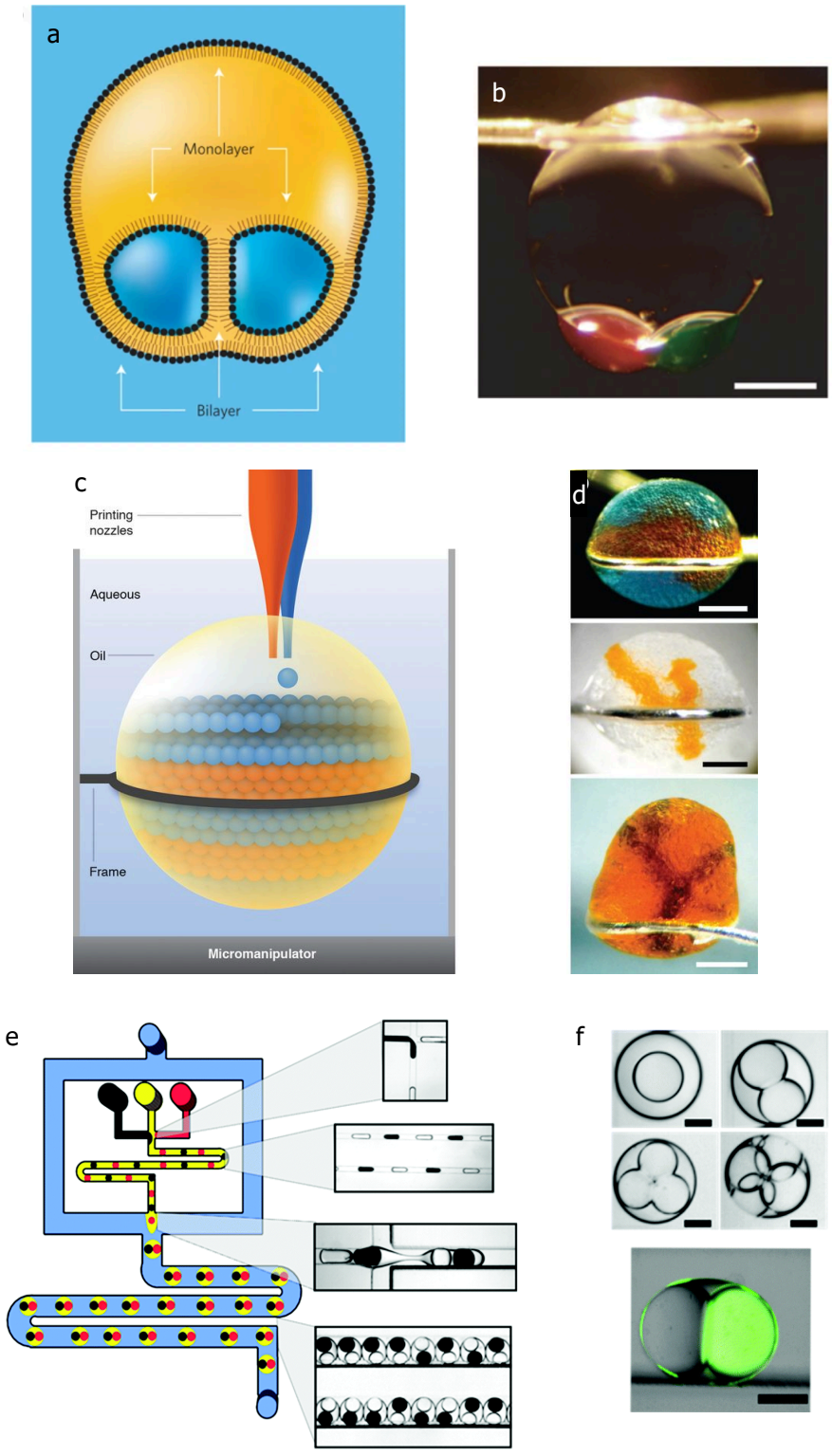


Figure 1.7: Multisomes. a-b. Multisomes generated manually. **a.** Bilayers form between the internal aqueous compartments and the aqueous compartments and the external aqueous environment[12]. **b.** Side view of a multisome containing two internal aqueous compartments[12]. **c-d.** Multisomes generated by 3D-printing. **c.** 3D-printing of multisomes[94]. **d.** Examples of 3D-printed multisomes containing various 3D patterns[94]. **e-f.** Multisomes generated by microfluidics. **e.** Microfluidic generation of multisomes[111]. **f.** Examples of multisomes containing 1-4 internal aqueous compartments, generated by microfluidics[111].

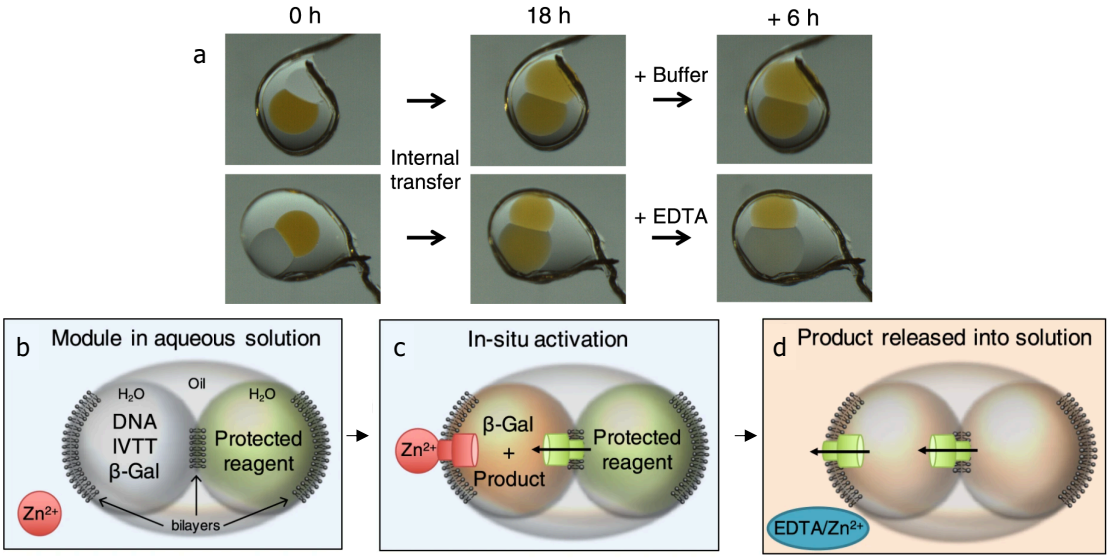


Figure 1.8: IVTT expression of αHL-4H and controlled release of multisome contents. **a.** αHL-4H is expressed by IVTT inside one of the compartments and cargo molecules are encapsulated in the other compartment. Presence of Zn^{2+} in the external solution blocks the external αHL-4H pores while internal pores remain open. Encapsulated cargo molecules freely diffuse internally, but can diffuse out into the external environment only upon EDTA addition. **b.** αHL-4H is expressed by IVTT inside a compartment that also contains the enzyme β-galactosidase to deprotect a reagent of interest. **c.** Pores form in the internal bilayer connecting the αHL-4H compartment to the protected reagent compartment, but not in the bilayer to the external environment. The reagent diffuses to the β-galactosidase compartment without leakage to the external environment and undergoes enzymatic deprotection. **d.** EDTA added to the external environment removes the Zn^{2+}, enabling pore formation to release the product[112].

Multi-compartment structures in water, not encapsulated within an oil drop, can also be generated and are referred to as multi-compartment vesicles. One way of forming such vesicles is by phase transfer of aqueous droplets from a lipid-oil environment into an aqueous environment mediated by gravity (Fig. 1.9a, b)[114]. αHL has been used to show diffusion of Ca^{2+}ions between the compartments and into the external aqueous environment[114]. Proteins have been synthesised by encapsulating an IVTT system inside the compartments[54]. In this case, the compartments did not interact with the external environment. An enzymatic cascade reaction has also been demonstrated in multi-compartment vesicles[115]. αHL has been used for the diffusion of a substrate molecule from the environment into the compartments, leading to a the production of a fluorescent molecule[115]. Multi-compartment vesicles have also been made by microfluidic

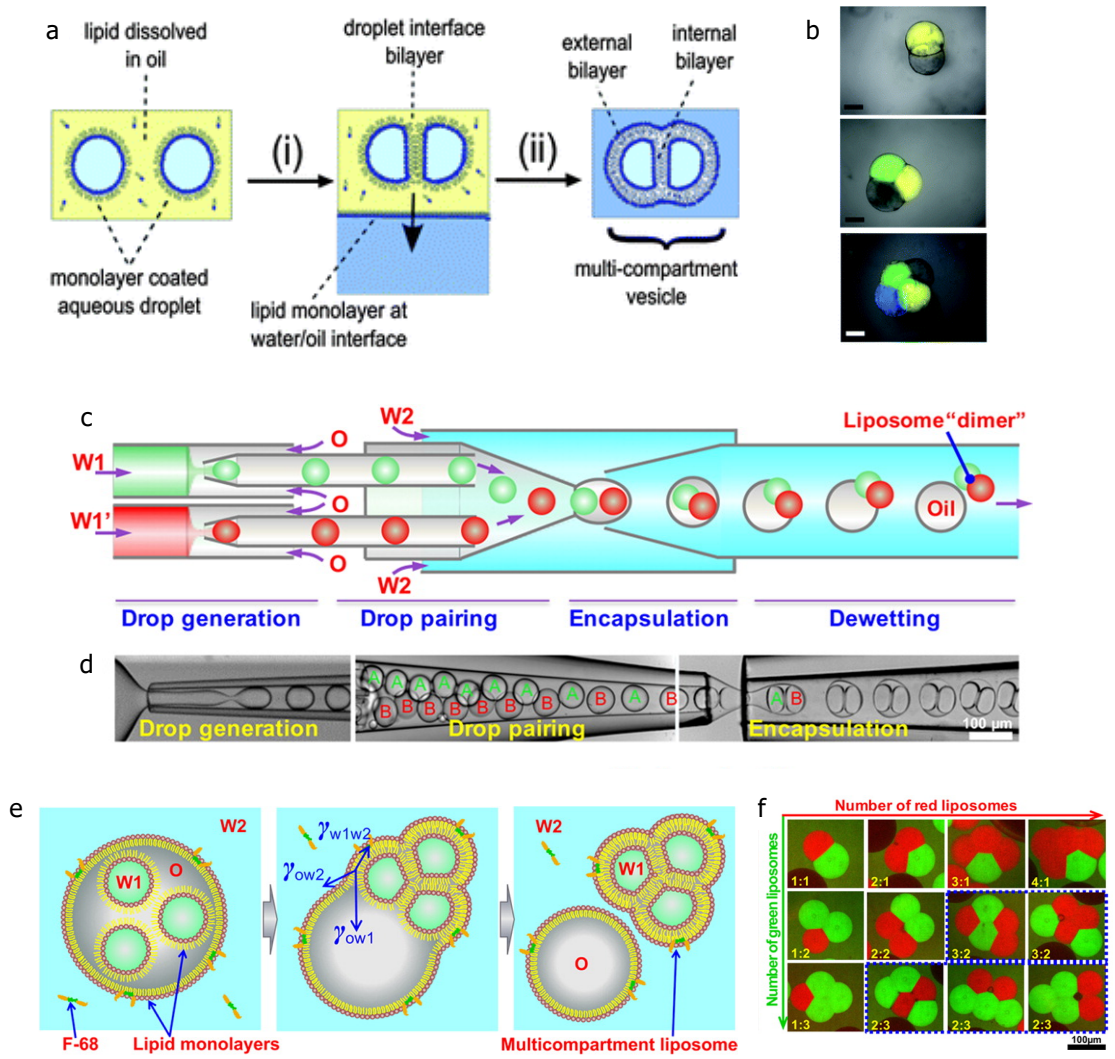


Figure 1.9: Multi-compartment liposomes. a-b. Multicompartment liposomes generated by gravity-mediated phase transfer. **a.** Generation of multi-compartment liposomes by phase transfer of droplets connected by DIBs from an external oil phase into an aqueous phase. Lipid bilayers form at the interface of the droplets with the external aqueous phase, resulting in multi-compartment liposomes. **b.** Fluorescence images of multi-compartment liposomes with 2, 3 and 4 compartments. Scale bars = 250 µm[114]. **c-f.** Multicompartment liposomes generated by microfluidics and surfactant-assisted dewetting. **c.** Generation of two-compartment liposomes by dewetting of w/o/w double emulsions by microfluidics. **d.** Snapshots of the process in c showing generation and pairing of droplets in an oil phase and encapsulation of the pair in an oil phase within an external aqueous phase. **e.** Surfactant-assisted dewetting of w/o/w double emulsions from d to generate multi-compartment liposomes. **f.** Multi-compartment liposomes of various numbers of compartments generated with the dewetting method described in **c-e**. Scale bars = 100 µm[73].

generation of internal aqueous compartments connected by DIBs within a lipid-oil drop (Fig. 1.9c, d), and dewetting of this multi-compartment structure from the lipid-oil drop assisted by a surfactant (Fig. 1.9c, e, f)[73]. αHL has been used to show diffusion of molecules from compartments into the external aqueous environment[73].

Lipid-based multi-compartment structures generated so far have shown poor stability to coalescence in a water environment[112,114]. The yield of two-compartment structures with no internal cargo had a yield of formation 43% and a lifetime of 60 minutes[114].

All synthetic structures generated so far, regardless of their number of compartments or the materials they are based on, have contained a single signalling pathway and performed a single task. Biological cells and tissues receive, process and produce multiple chemical signals simultaneously and without cross-talk[116–118]. Synthetic structures that process multiple external signals to perform multiple tasks have not been engineered.

1.3 Design of a lipid-based parallel processor

In this work, we design and produce a multi-compartment processor from the bottom-up in a modular fashion. Each compartment is optimised for a distinct task such as signal transmission, sensing or enzymatic processing (Fig. 1.10a). For our processors, we employ the multisome platform on a Teflon-coated silver wire (Fig. 1.10b). When three aqueous compartments sink inside the lipid-oil drop, lipid bilayers form between each compartment and between each compartment and the external aqueous environment. αHL in the signal transmission compartment self-inserts into all of the bilayers surrounding the compartment. Therefore, the formed pores connect the signal transmission compartment both to the external environment and to the two internal processing compartments (Fig. 1.10a). The signal transmission compartment exchanges

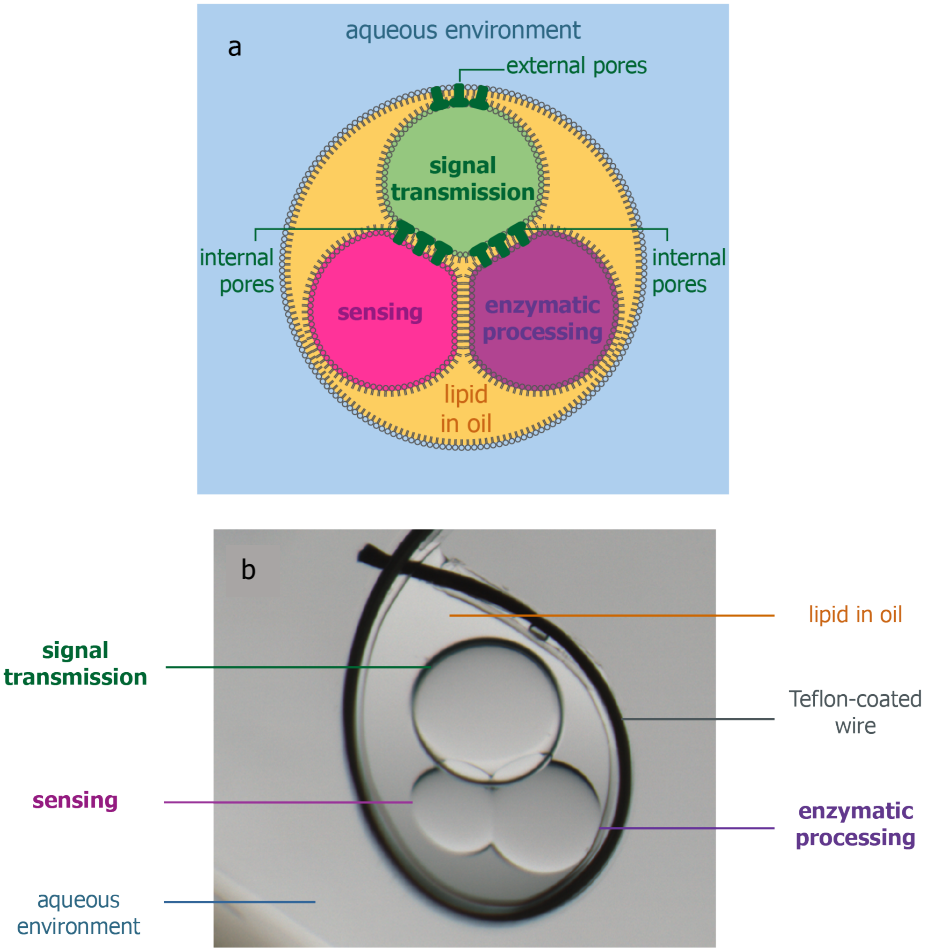


Figure 1.10: The three-compartment parallel processor. a. The processor comprises a signal transmission compartment and two processing compartments: sensing and enzymatic processing. Chemical communication with the external environment is enabled by internal and external pores. **b.** Top view of a three-compartment processor in an oil drop supported by a Teflon-coated wire loop in an external aqueous environment. Wire diameter = 76 μm.

chemicals with the external environment through the external pores and with the two processing compartments through the internal pores.

Our processors receive and process external chemical signals independently or simultaneously, and produce a distinct output for each signal (Fig. 1.11). They generate a fluorescence output suitable for sensing applications and a molecular output suitable for chemical communication and drug delivery applications. When chemical input signal 1 is introduced to the external aqueous environment, it diffuses through the external and internal pores to reach both processing compartments, and produces a fluorescence output in the sensing

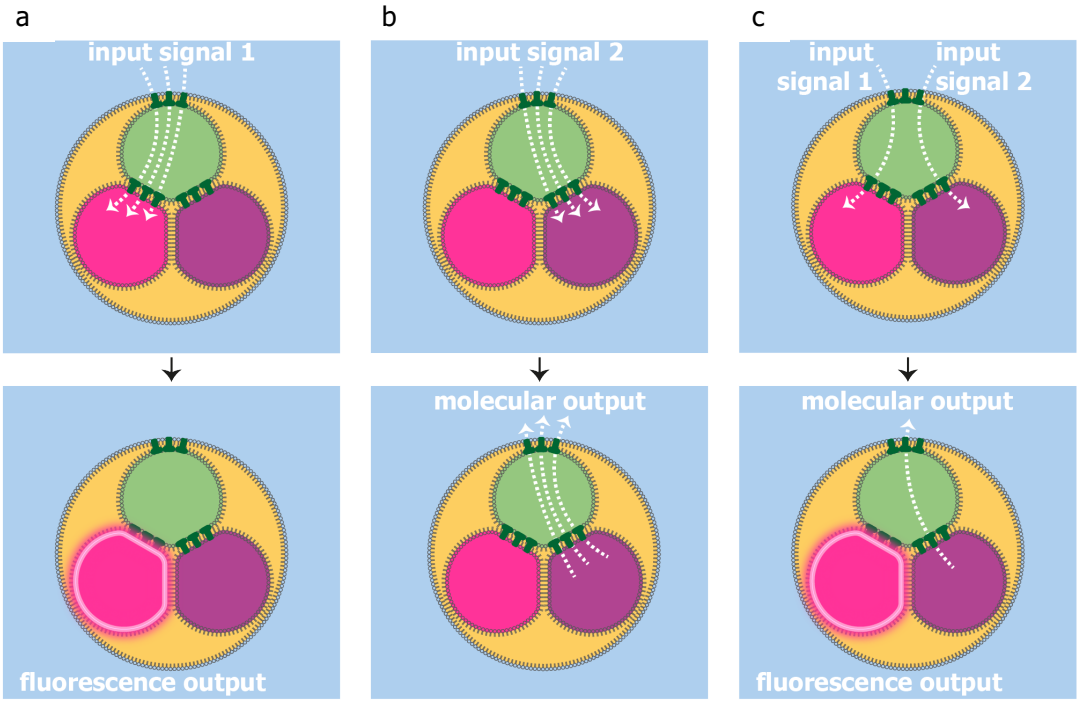


Figure 1.11: Signalling in the three-compartment parallel processor. a. Input signal 1 added into the external environment diffuses through the αHL pores and produces a fluorescence output signal in the sensing compartment. **b.** Input signal 2 added into the external environment diffuses through the αHL pores and undergoes a reaction in the enzymatic processing compartment. The product molecule diffuses through the αHL pores and is released into the external environment as a molecular output signal. **c.** Input signals 1 and 2 added into the external environment generate both fluorescence and molecular output signals.

compartment (Fig. 1.11a). Similarly, chemical input signal 2 reaches both processing compartments, and reacts in the enzymatic processing compartment. The product diffuses through the internal and external pores, and is released into the external environment as a molecular output (Fig. 1.11b). When both chemical input signals 1 and 2 are introduced, both outputs are simultaneously generated (Fig. 1.11c). In the absence of input signals, no output signals are produced.

1.4 Thesis scope and summary

In this work, we optimise the application of αHL nanopores to enable fast molecular diffusion between synthetic compartments. This rapid chemical

communication, which is crucial for building synthetic tissues and devices with complex functions, allows us to build a multi-compartment droplet processor that can carry out multiple reactions in response to input signals. Synthetic biological systems to date have been constructed with no more than one signalling pathway. Therefore, the multi-compartment processor in this thesis represents the first bottom-up synthetic biological system with independent and simultaneous processing of more than one signal. We build this processor from the bottom-up in a modular fashion.

In Chapter 2, we establish signal transmission between aqueous compartments. Using recombinant αHL, we show fast molecular diffusion across DIBs for the first time. We also study the processes of molecular diffusion across αHL pores and DIB formation over time. We then discuss scenarios of chemical signal diffusion with no membrane, with a membrane and with a membrane permeabilised by αHL pores. We calculate the permeability of the DIBs in our setup to the molecular signal in this work. We discuss the effect of DIB size and compartment size on the diffusion of chemical signals. We also calculate the number and density of the αHL pores incorporated into the DIBs in our system.

In Chapter 3, we build two-compartment structures that exchange chemicals with the external aqueous environment. In two-compartment structures with signal transmission and signal release compartments, we show fast release of molecules into the external aqueous environment. We also show intake and processing of ions to produce a fluorescence output by two-compartment structures with signal transmission and sensing compartments.

In Chapter 4, we build two-compartment processors with signal transmission and enzymatic processing compartments, and couple exchange of chemical signals to enzymatic processes. We first show the intake of ionic signals to activate a DNA cleavage reaction by the endonuclease EcoRI, and the production of a fluorescence output. We then show the intake of lactose molecules and their hydrolysis by β-galactosidase to produce and release glucose to the external aqueous environment.

In Chapter 5, we bring various compartments from previous chapters to build three-compartment processors. We combine the sensing and β-galactosidase compartments to show orthogonal processing of all possible combinations of input signals, and production of fluorescence and molecular outputs. We also combine the EcoRI and β-galactosidase compartments to demonstrate simultaneous enzymatic processing of input signals.

In Chapter 6, we discuss the outcomes of this work and its implications for sophisticated sensors, micro-reactors, drug delivery vehicles, and synthetic and hybrid tissues in the future.

We provide all experimental details in Chapter 7.

2

Fast molecular diffusion through α-hemolysin heptamerised in situ

Contents

2.1 Introduction 23
2.2 Purification of αHL 25
2.2.1 Purification using a centrifugal filter device 25
2.2.2 Fast Protein Liquid Chromatography (FPLC) Purification 30
2.3 Fast molecular diffusion through αHL heptamerised in situ . . . 33
2.4 Effect of fatty acyl chain branching on in situ αHL heptamerisation 34
2.5 Additional observations on molecular diffusion through αHL heptamerised in situ 36
2.6 Additional considerations on molecular diffusion across DIBs . 38
2.6.1 Diffusion between compartments 38
2.6.2 Effect of DIB size 41
2.6.3 Effect of compartment size 42
2.6.4 Estimation of αHL pore number and density 44
2.7 Conclusion 46

2.1 Introduction

The most crucial requirement for processing chemical signals is effective signal transmission. In our system, signal transmission relies on passive diffusion of molecules through size-selective αHL pores. Chemical input signals from the

external environment must diffuse through two bilayers to reach a processing compartment. If an output signal is released, it must also diffuse through two bilayers to reach the external environment. For this case, passive diffusion of chemicals across a total of 4 bilayers is required. In addition, a released chemical output signal becomes highly diluted once it mixes with the external environment. For example, a typical compartment in a multisome generated manually is ~50 nL and the external aqueous environment 1 mL[112]. Contents released from the compartment into the external environment would undergo a ~20,000-fold dilution. Therefore, fast molecular diffusion, enabled by efficient insertion of a high number of pores into the bilayers, is vital.

Pore-forming membrane protein αHL is secreted as water soluble monomers of ~33 kD from *S. aureus*[119]. On a range of cell membranes, the monomers assemble to form a heptameric pore[120]. The transmembrane domain is a 100 Å-long β-barrel with an effective diameter of 1.14 nm[47]. Diffusion through αHL pores in synthetic compartments has been shown with Ca^{2+} ions and a range of small molecules using heptamers purified from *S. aureus* by a lengthy procedure, commercially sourced monomers from *S. aureus*, or monomers obtained by cell-free expression at high cost and with variable yields. Ca^{2+} diffusion was shown from an external aqueous environment into multisomes[12], multicompartment vesicles[114] and GUVs[70]. Diffusion of molecules including pyranine[101], guanine[93], glucose[115], and 3-carboxyumbelliferyl-β-D-galactopyranoside (CUG)[112], was shown in DIBs, across two compartments of a multicompartment vesicle, and from multisomes to an external aqueous environment. In these cases, incomplete diffusion was reported over tens of minutes, hours or days. We required much faster diffusion rates to make our processors feasible. Here, we express and purify recombinant αHL and employ fast protein liquid chromatography (FPLC) to purify monomers and heptamers separately. We demonstrate fast rates of molecular diffusion when our monomers are heptamerised in the DIB.

2.2 Purification of αHL

We expressed His-tagged recombinant αHL in *E. coli* cells and isolated it with His-tag purification (Fig. 2.1). Similar to the αHL previously obtained from *S. aureus*[100], we obtained a mixture of αHL monomers and spontaneously heptamerised αHL.

2.2.1 Purification using a centrifugal filter device

We initially attempted to separate the monomers and heptamers as well as exchange the buffer using centrifugal filter devices. We used devices with a cellulose membrane and various cutoff values (Amicon, Millipore). The sample is loaded on the membrane, and 'washed' a selected number of times with a new buffer, with the help of centrifugation. During these washes, the molecules with molecular weight below the cutoff value pass through the membrane and are discarded, while the molecules with molecular weight above the cutoff value (in kD, represented as K on the devices) are retained. In this way, centrifugal filtration devices may separate biomolecules by molecular weight, concentrate them, and exchange their buffer.

As αHL has a molecular weight of ~33.2 kD per monomer and ~232.4 kD per heptamer[47], we expected the columns with cutoff values of 3K and 30K to retain both the monomers and heptamers while removing the original buffer and exchanging it with the new buffer. On the other hand, columns with cutoff values of 50 or 100K should remove the monomers together with the original buffer, and retain the heptamers in the new buffer. We initially attempted to exchange the buffer of our αHL after Ni-NTA purification using the centrifugal columns with cutoff values of 3K or 50K. We used 10 mM Tris pH 8.0, 200 mM NaCl as the new buffer with which to replace the Ni-NTA purification buffer. After washing the samples twice, we detected no protein with SDS-PAGE gel electrophoresis (Fig. 2.2). To determine whether the protein was being lost during the washing process, we concentrated the filtrates by centrifugation in a vacuum concentrator

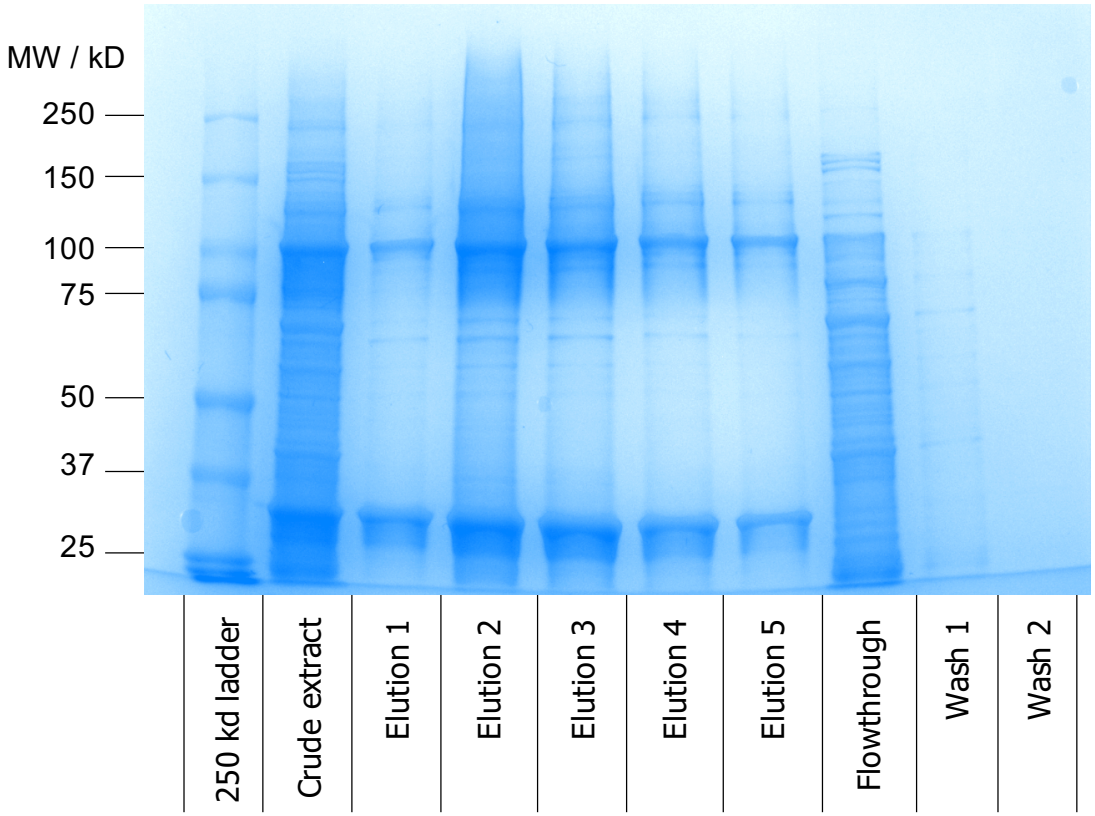


Figure 2.1: SDS-PAGE gel of elutions after His-tag purification of αHL. All elutions contained a mixture of αHL monomers and heptamers

system, with no heating. As the solvent was water, this process took several hours. With SDS-PAGE gel electrophoresis, we determined that some protein was being lost during the washing process. However, by visual inspection of the gel and comparison to the protein that was loaded to the columns (Fig. 2.2, Elution #3 crude), this loss did not seem to account for all the protein that was lost.

Next, we tried using centrifugal columns with cutoff values of 30K and 50K. From the experiments discussed above, we hypothesised that the protein might be sticking to the cellulose membrane, resulting in a loss of sample. Therefore, in addition to testing the process with the same buffer as above, we also tested it with 0.006% w/v sodium dodecyl sulfate (SDS) added to the buffer. The addition of a detergent such as SDS may solubilise the protein and aid in sample recovery. However, after four washes, we still did not detect any protein in either the elute or the concentrated filtrates (Fig. 2.3).

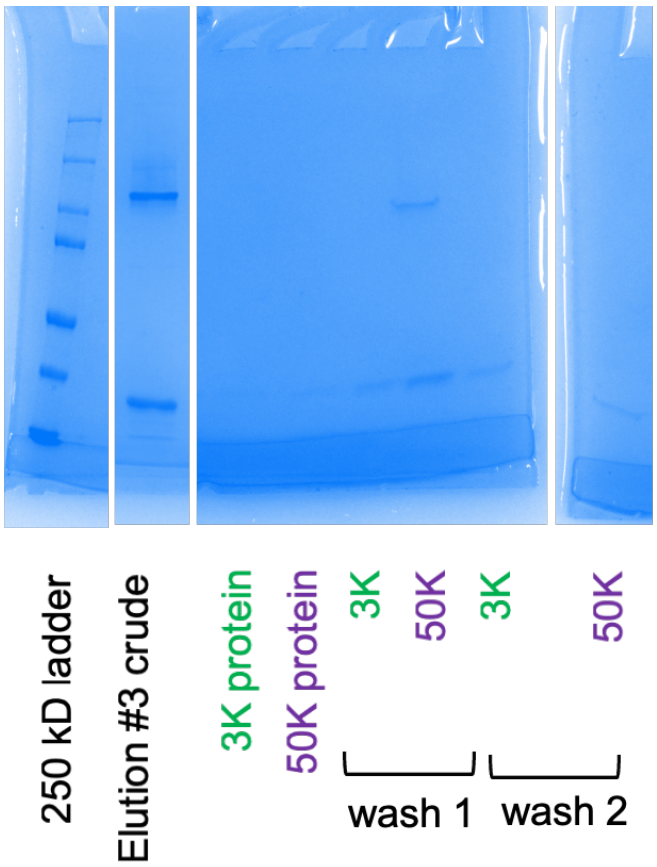


Figure 2.2: SDS-PAGE gels of αHL ran through centrifugal filtration columns with cutoff values of 3K and 50K. a. b-d.

Examining the SDS-PAGE gel of the products and concentrated filtrates from the columns with cutoff values of 50K (Fig. 2.4), we detected no protein in samples washed with 0.006% w/v SDS (Fig. 2.4a) or with no SDS (Fig. 2.4c). However, we detected protein in the sample washed once with 0.06% w/v SDS and three times with 0.006% w/v SDS. This result indicated that increasing the SDS concentration by 10 times may solubilise the αHL and reduce the amount of αHL sticking to the membrane of the centrifugal device. We also detected the lost protein in the concentrated filtrates from the first round of washing of the samples in Fig. 2.4b and c.

Based on the more promising results with higher concentration of SDS, we

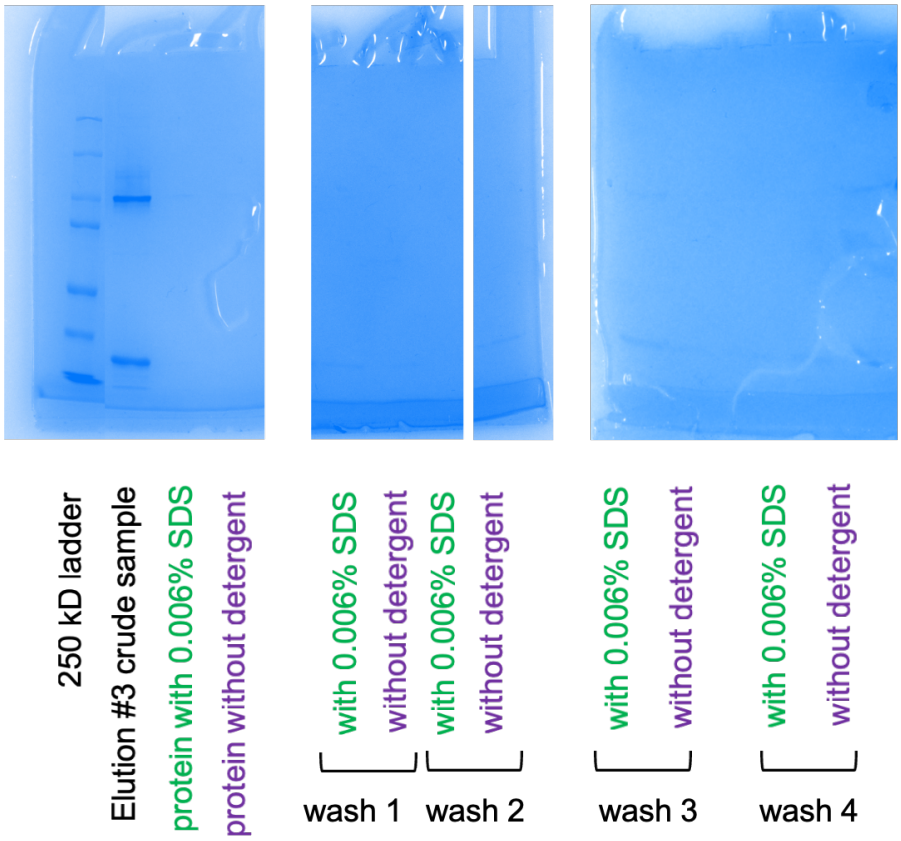


Figure 2.3: SDS-PAGE gels of αHL ran through centrifugal filtration columns with cutoff values of 30K with 0.006% w/v or no SDS. a. b-d.

washed αHL four times with buffer containing 0.06% SDS using centrifugal filtration devices with cutoff values of 30K, 50K and 100K. We detected a mixture of αHL monomers and heptamers in the samples from all three columns by SDS-PAGE gel electrophoresis (Fig. 2.5). We also concentrated the filtrates and found no detectable lost protein from the column with the 30K cutoff value, lost monomers from the column with the 50K cutoff value and a mixture of lost monomers and heptamers from the column with the 100K cutoff value. We measured the concentrations of the resulting protein using a Nanodrop device as 6.81, 8.73 and 8.59 mg mL^{-1} for the samples from 30K, 50K and 100K columns, respectively. For comparison, we detected 4.18 mg mL^{-1} of protein in the crude elution before loading into the centrifugal concentration devices.

One of our goals was to determine whether monomeric or spontaneously

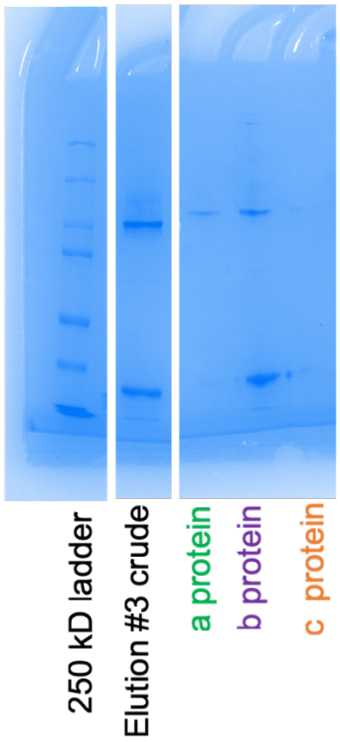


Figure 2.4: SDS-PAGE gels of αHL ran through centrifugal filtration columns with cutoff values of 50K with or without SDS. a-c αHL was washed in the device with buffer containing 0.006% w/v SDS four times, 0.06% w/v SDS once and 0.006% w/v SDS three times (b) or no SDS four times (c).

heptamerised αHL would show a higher rate of insertion into lipid bilayers. However, none of the centrifugal columns separated the monomeric and heptameric forms of αHL. To obtain concentration of αHL in the range of a few hundreds of micrograms per millilitre to be used in DIBs, we would need to dilute the purification products by only one order of magnitude. As a result, we would obtain a concentration of SDS of 0.006% w/v, which could interact with the lipid bilayers[121,122] and destabilise the DIB system. Additionally, via the same mechanism through which SDS is able to solubilise αHL during purification, it may prevent or slow down the protein insertion into the DIB. On the other hand, with lower concentrations of SDS or no SDS in the wash buffer, we did not recover any αHL from the centrifugal columns. It therefore appeared that purification and separation of αHL monomers and heptamers using the centrifugal filtration devices might not be feasible. An alternative method that would allow us to both

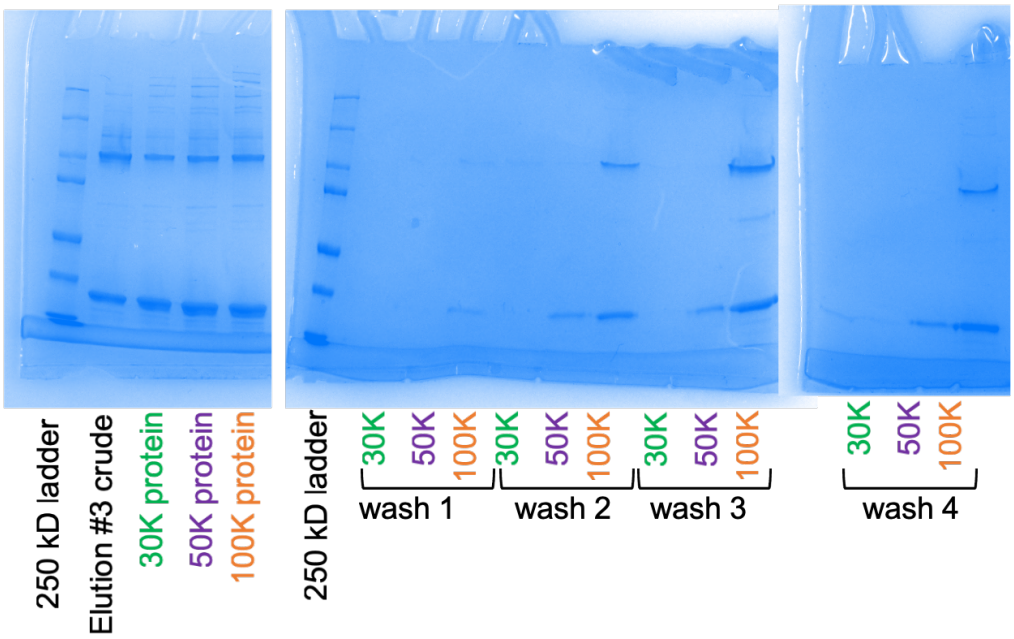


Figure 2.5: SDS-PAGE gels of αHL ran through centrifugal filtration columns with cutoff values of 30K, 50K and 100K with 0.06% w/v SDS. αHL was washed in the devices with buffer containing 0.06% w/v SDS four times.

purify and separate monomers and heptamers without the need of a detergent would therefore be ideal.

2.2.2 Fast Protein Liquid Chromatography (FPLC) Purification

We decided to investigate another purification method, fast protein liquid chromatography (FPLC). With FPLC, we could monitor the purification process in real-time using UV monitors. We chose size exclusion chromatography (also known as gel filtration) so that we could separate the monomers and heptamers based on their size while also purifying them into the new buffer. This method employs porous beads. The smaller the molecule, the more likely it is to penetrate through the beads, resulting in a delay in elution. Larger molecules are unable to penetrate through the beads, so they elute faster. For αHL, we therefore expect heptamers to elute before monomers, and the buffer components to elute at the very end. We used a column that contains a composite matrix of dextran

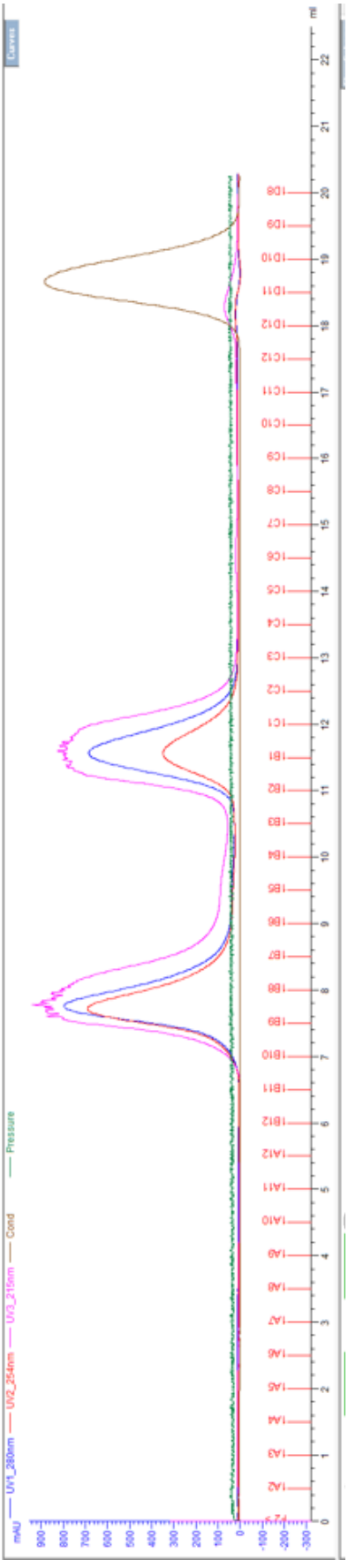


Figure 2.6: FPLC trace of αHL purified with size exclusion chromatography. The UV absorption of fractionated monomers and heptamers were monitored. Heptamers eluted first and monomers eluted later.

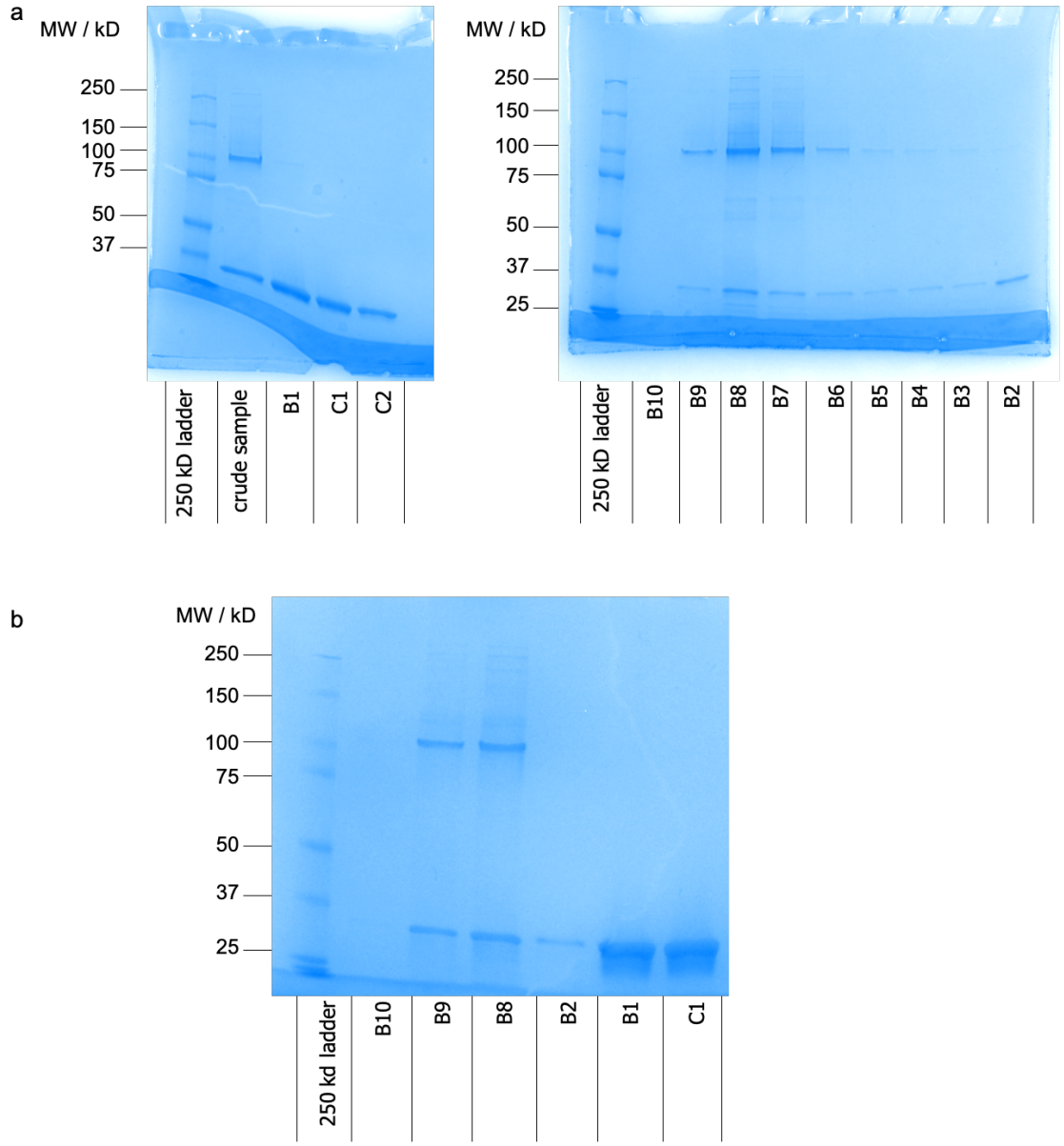


Figure 2.7: SDS-PAGE gel of elutions after an example purification of αHL by size exclusion chromatography. B10 contains negligible amount of αHL. B8 and B9 contain a mixture of αHL monomers and heptamers. B2, B1 and C1 contain monomers only.

and agarose, (Superdex 75 100/300 GL, GE Healthcare).

We observed separate peaks for αHL monomers and heptamers in the chromatograms (an example chromatogram is shown in Fig. 2.6). We also visualised the purified αHL fractions with the highest concentrations using SDS-PAGE gel electrophoresis (two example gels are shown in Fig. 2.7) and measured their concentrations using a Nanodrop. The peak fractions typically had concentrations of 200-400 μg mL^{-1}.

FPLC purification of αHL was successful. With this method, we were able to separate αHL monomers and heptamers at high purity, and at high concentrations, without the use of detergents.

2.3 Fast molecular diffusion through αHL heptamerised in situ

We then employed DIBs as a model system to study molecular diffusion through pores formed by the αHL we generated here. We formed a signal release compartment containing 1 mM 2-[*N*-(7-nitrobenz-2-oxa-1,3-diazol-4-yl) amino]-2-deoxy-D-glucose (2-NBDG) and a signal transmission compartment containing 200 μg mL^{-1} αHL monomers or 200 μg mL^{-1} heptamers, or no αHL, within an oil environment containing 1,2-diphytanoyl-s*n*-glycero-3-phosphatidylcholine (DPhPC). This concentration of αHL is high compared to previous examples of DIBs in oil which were 20[94], 50[93] and 83[101] μg mL^{-1} maximum. Mimicking the arrangement in a processor with multiple smaller compartments surrounding a larger signal transmission compartment, we used a 250-300 μm diameter (8-14 nL volume) signal release compartment with a 500-650 μm diameter (65-144 nL volume) signal transmission compartment. We then brought the compartments together to form DIBs (Fig. 2.8a), and observed 2-NBDG diffusion across the DIBs. Using purified αHL monomers, we observed fast molecular diffusion, with complete equilibration of 2-NBDG molecules within 6 minutes in our specific

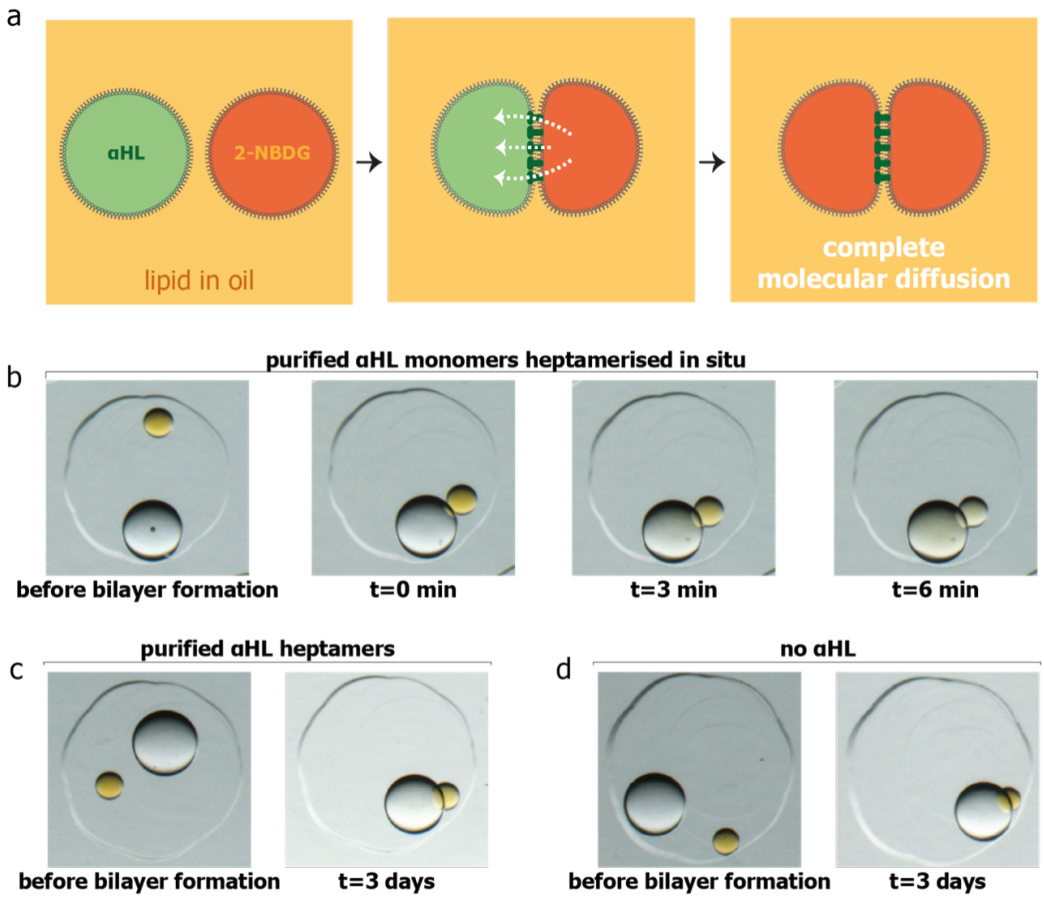


Figure 2.8: Fast molecular diffusion through αHL heptamerised in DIBs. a. Formation of a DIB between a signal transmission compartment and a signal release compartment within a lipid-oil external environment, and diffusion of 2-NBDG molecules through α-hemolysin (αHL) pores. **b-d** Bright-field microscopy images of diffusion of 2-NBDG molecules across DIBs using purified αHL monomers (b), purified αHL heptamers (c), or no αHL (d).

setup (n = 5, Fig. 2.8b). With αHL heptamers (n = 3, Fig. 2.8c) or no αHL (n = 3, Fig. 2.8d), diffusion of 2-NBDG was not visible over 3 days.

2.4 Effect of fatty acyl chain branching on in situ αHL heptamerisation

We also investigated the effect of the composition of the lipid bilayer, specifically the branching on the fatty acyl chain(s) of the lipids on the insertion of αHL into the bilayer. DPhPC has methyl branches on the two fatty acyl chains. A lipid with unbranched fatty acyl chains, such as 1-palmitoyl-2-oleoyl-s*n*-glycero-

3-phosphocholine (POPC) may form more tightly packed arrangements in the bilayers[123–125] and higher DIB area[99]. A larger number of αHL pores could insert into this larger DIB area. We made DIBs consisting of a signal transmission droplet containing 200 µg mL^{-1} αHL monomers and a signal release droplet containing 1 mM 2-NBDG. We formed DIBs in oil containing 1.2 mM lipid in total at POPC:DPhPC ratios of 0:1 (no POPC), 0.2:0.8 and 0.4:0.6. Even though the DIBs indeed became larger with increasing POPC concentration, the diffusion of 2-NBDG became slower (Figure 2.9). We attributed this slower diffusion to the more dense packing of POPC lipids, allowing a fewer number of αHL heptamerisations on the lipid bilayer. Therefore, we confirmed that the use of POPC lipids, despite forming larger bilayers, reduced the rate of molecular diffusion.

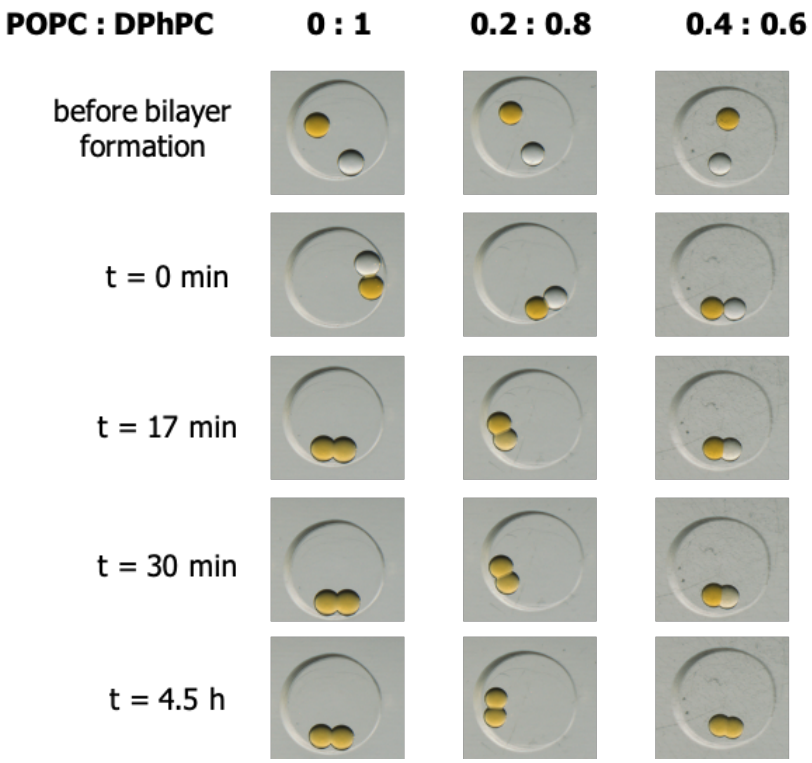


Figure 2.9: Diffusion of 2-NBDG through in-situ heptamerised αHL in various lipid conditions. The lipid-oil mix contained -palmitoyl-2-oleoyl-s*n*-glycero-3-phosphocholine (POPC):1,2-diphytanoyl-s*n*-glycero-3-phosphatidylcholine (DPhPC) ratios of 0:1, 0.2:0.8 and 0.4:0.6.

2.5 Additional observations on molecular diffusion through αHL heptamerised in situ

We used epifluorescence microscopy to further study molecular diffusion using αHL monomers heptamerised in a DIB. We formed a signal release compartment containing 1 mM 2-NBDG and a signal transmission compartment containing 200 µg mL^{-1} αHL monomers, both 410 µm in diameter (36 nL in volume). We observed 2-NBDG diffusion as soon as the two compartments were brought together to form a DIB, while bilayer expansion was still in progress. Interestingly, we were able to observe the gradients of molecular diffusion into the αHL-containing compartment. For example, we initially observed a plume of fluorescence near the bilayer inside the αHL-containing compartment, followed by homogenisation of the fluorescence inside this compartment as the contents mixed (Fig. 2.10).

We then quantified the fluorescence in the signal transmission compartment receiving the 2-NBDG molecules and the contact angle between the two compartments as an indication of the bilayer size[99]. The bilayer formation lasted ~20 min, starting relatively faster and slowing down as the bilayer approached its maximum size. Molecular diffusion began as soon as bilayer formation began. As observed from the fluorescence in the receiving compartment, the rate of molecular diffusion increased exponentially at the start as the number of inserted pores increased, continued at a constant rate once the maximum number of pores had formed in the bilayer, and slowed down as the concentration of 2-NBDG across the DIB approached equilibrium (Fig. 2.11).

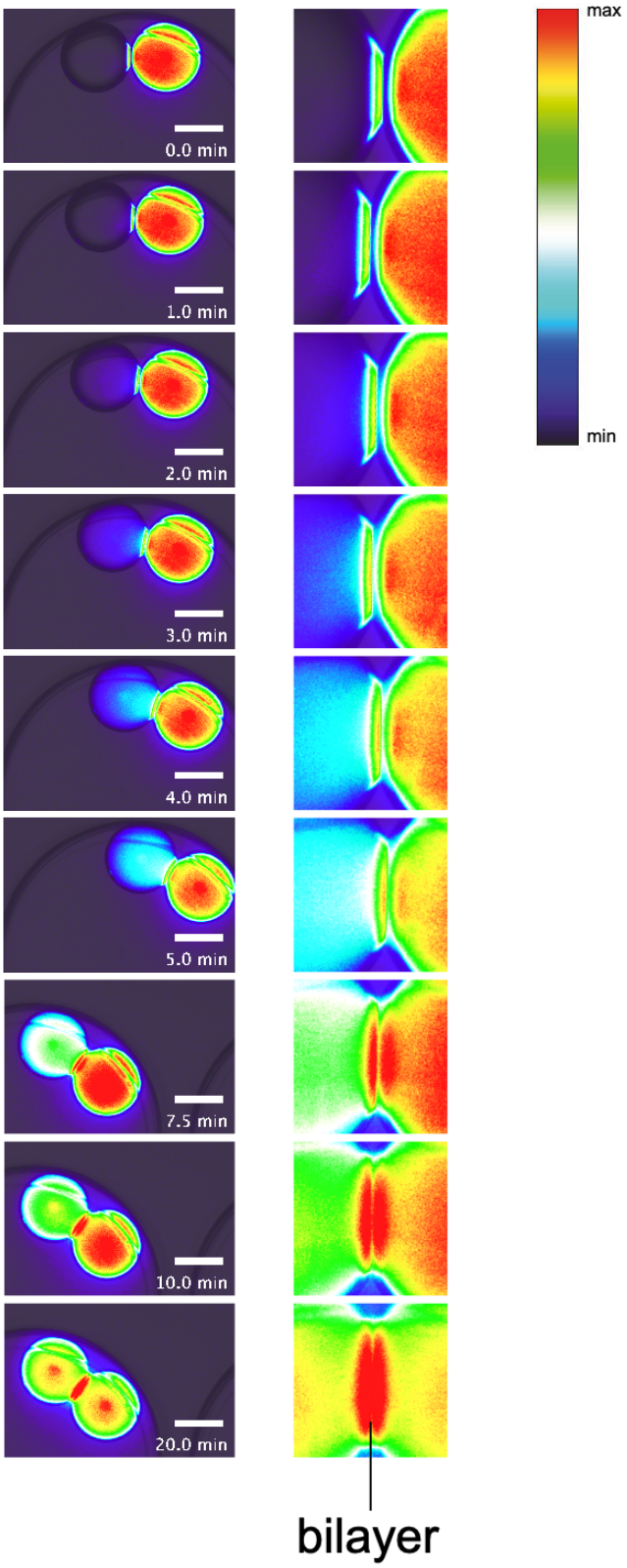


Figure 2.10: Molecular diffusion through αHL pores followed by mixing inside the receiving compartment. Composite bright-field and epifluorescence microscopy images of time-dependent molecular diffusion of 2-NBDG across a DIB containing in situ heptamerised recombinant αHL. Magnified images of DIBs are also shown at each time point.

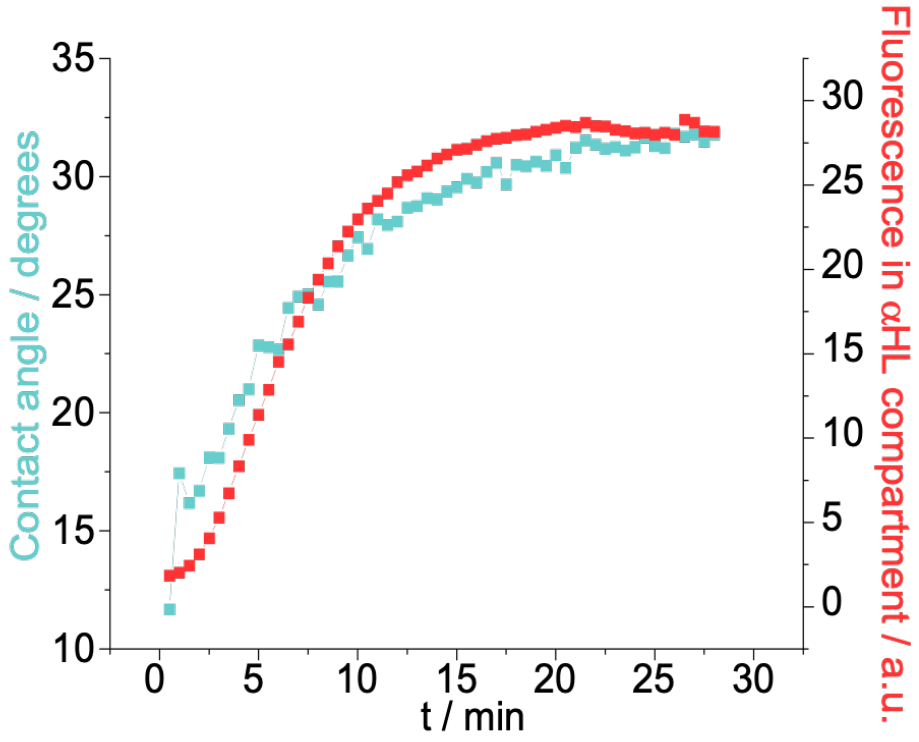


Figure 2.11: Simultaneous DIB expansion and molecular diffusion through αHL pores. Plots of contact angle as an indication of bilayer size between the two compartments and fluorescence in the receiving compartment, over time.

2.6 Additional considerations on molecular diffusion across DIBs

2.6.1 Diffusion between compartments

In our systems, compartments communicate with one another and with the external environment via diffusion of chemical signals through aqueous solutions and αHL pores in DIBs. Therefore, the chemical properties of the signal and the properties of the bilayer can lead to different times for the equilibration of the signal molecule. Three scenarios are depicted in Fig. 2.12.

For simplicity, we consider diffusion in one dimension. In the absence of membranes (Fig. 2.12a), the time of equilibration t of a solute in solution with a diffusion coefficient D over a mean distance x can be approximated by the time lag equation[126]:

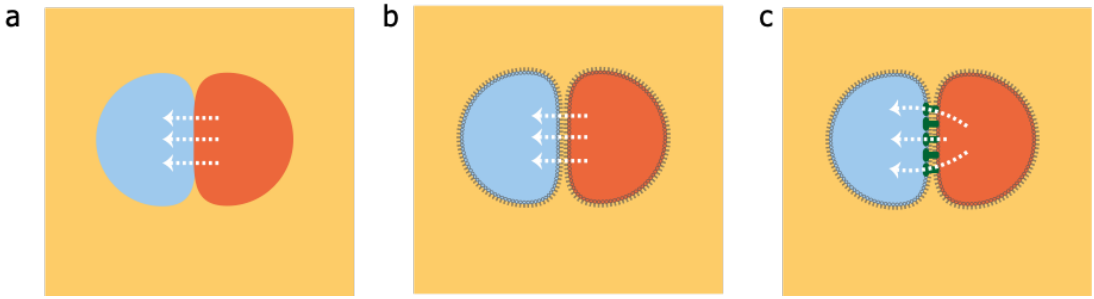


Figure 2.12: Equilibration of a chemical signal between compartments under various scenarios. a. Diffusion of a chemical signal in the absence of a membrane. **b.** Diffusion of a chemical signal by permeation through a lipid membrane. **c.** Diffusion of a chemical signal through a lipid membrane permeabilised by αHL pores.

$$t \approx \frac{\bar{x}^2}{6D} \tag{2.1}$$

Let us consider the hypothetical case of diffusion of glucose within two spherical compartments of diameter $d = 410$ µm with no membrane at their interface. In water, glucose has a diffusion coefficient D of 650 µm^2 s^{-1}. In a pair of compartments of these dimensions, the mean distance of diffusion is $\bar{x} \approx d = 410$ µm (Fig. 2.13). From Equation 2.1, we obtain $t \approx 43$ s. Therefore, in the case of glucose diffusion in an aqueous solution without a membrane, an equilibration time of the order of tens of seconds is expected.

Next, we consider the case where a membrane with permeability P separates the two compartments (Fig. 2.12) where the difference in concentrations of the solute across the membrane is ΔC. The diffusive flux J of the solute through the membrane is[127]:

$$J = -P\Delta C \tag{2.2}$$

Considering the case in Fig. 2.10 of two compartments containing 2-NBDG of concentrations of $C_1 = 1$ mM and $C_2 = 0$ mM respectively, we obtain $\Delta C =$ -1 µmol cm^{-3}. P depends on the molecular properties and varies widely. For example, a membrane-permeant molecule, indole has $P_{\text{indole}} \approx 10^{-4}$ cm s^{-1} while a membrane-impermeant molecule, glucose, has $P_{\text{glucose}} \approx 10^{-7}$ cm s^{-1}.

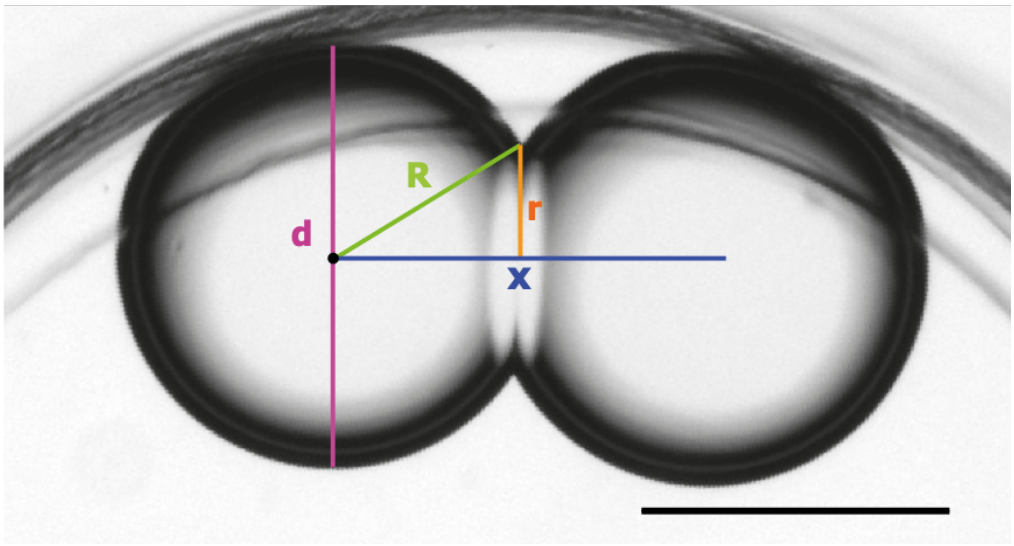


Figure 2.13: Distances in a DIB system. Overlays on an optical microscopy image of a DIB system consisting of two compartments, illustrating the compartment diameter, d; the compartment radius, R; and the DIB radius, r. Scale bar = 300 μm.

Let us now calculate the time t required to equilibrate N number of moles of solute across two compartments of diameter d separated by a bilayer of area A. For compartments of $d = 410$ μm, the radii will be $R = d/2 = 205$ μm. If we assume a circular interface bilayer of radius $r = R/2 = 102.5$ μm, the DIB area between the two compartments will be $A = \pi R^2 = 3.3 \times 10^{-4}$ cm^2. After equilibration of the solute across the membrane, the number of moles of the solute in each compartment will be half the number of moles of solute initially in its original compartment at concentration C_1. Therefore, the number of moles that must diffuse across the membrane is:

$$N = C_1 V/2 \tag{2.3}$$

where V is the compartment volume. For a compartment of $R = 205$ μm, the volume is $V = 6$ nL $= 3.6 \times 10^{-5}$ cm^{-3}. Consequently, the number of moles that must diffuse is $N = 1.8 \times 10^{-5}$ μmol.

For the membrane-permeable small molecule indole, characterised by $P_{\text{indole}} \approx 10^{-4}$ cm s^{-1}, we obtain a flux $J \approx 10^{-4}$ μmol cm^{-2} s^{-1} and a rate of diffusion $JA \approx 3.3 \times 10^{-8}$ μmol s^{-1}. When $N = 1.8 \times 10^{-5}$ μmol, a time $t \approx 550$ s

(~9 min) is required for equilibration. In reality, as ΔC becomes smaller as diffusion progresses, the flux J would also become smaller, leading to a time of equilibration much higher than this estimate.

For the membrane-impermeable small molecule glucose, characterised by $P_{\text{glucose}} \approx 10^{-7}$ cm s^{-1}, we obtain a flux $J \approx 10^{-7}$ µmol cm^{-2} s^{-1} and a rate of diffusion $JA \approx 3.3\times10^{-11}$ µmol s^{-1}. When $N = 1.8\times10^{-5}$ µmol, a time $t \approx 5.5\times10^{5}$ s (~6.3 days) is required for equilibration. In reality, as ΔC becomes smaller during diffusion, the flux J would also become smaller, leading to a time of equilibration much higher than this estimate.

Membrane-impermeant molecules can diffuse across the bilayer if it is permeabilised with αHL pores (Fig. 2.12). We showed equilibration of 2-NBDG across a lipid bilayer within $t \approx$ 20 minutes experimentally in Fig. 2.10. This demonstrates that the addition of αHL pores permeabilised the bilayer to the otherwise membrane-impermeant solute 2-NBDG.

We can calculate the permeability coefficient $P_{\text{2-NBDG, DIB+}\alpha\text{HL}}$ of the membrane permeabilised by αHL pores in Fig. 2.10 using the equilibration time $t \approx$ 20 min, as:

$$P_{\text{2-NBDG, DIB+}\alpha\text{HL}} = \frac{-J}{\Delta C} = \frac{-N}{At\Delta C} \tag{2.4}$$

Therefore, $P_{\text{2-NBDG, DIB+}\alpha\text{HL}} \approx 4.6 \times 10^{-5}$ cm s^{-1}.

$P_{\text{2-NBDG, DIB+}\alpha\text{HL}}$ is underestimated in these calculations because the 20 min equilibration time includes the time during which the bilayer is still forming and the pores are still inserting (Fig. 2.11).

2.6.2 Effect of DIB size

In Section 2.6.1, we assumed $r/R =$ 0.5 to discuss the equilibration of a chemical signal between compartments in an oil environment. However, the rate of diffusion also depends on the membrane area. Using $\Delta C = -1$ µmol cm^{-3}, $N = 1.8 \times 10^{-5}$ µmol and $P_{\text{2-NBDG, DIB+}\alpha\text{HL}} \approx 4.6 \times 10^{-5}$ cm s^{-1} from Section 2.6.1, the equilibration time can be calculated as:

$$t \approx \frac{-N}{AP\Delta C} \tag{2.5}$$

We now perform calculations with varying DIB areas of 0.1 $\leq r/R \leq$ 0.9 (Table 2.1). The expected time for equilibration of 2-NBDG ranges between minutes and hundreds of minutes. The equilibration time of 2-NBDG across a DIB permeabilised by αHL quickly decreases as the DIB area increases (Fig. 2.14).

Table 2.1: Effect of bilayer area A_{DIB} on 2-NBDG equilibration by diffusion across a DIB permeabilised by αHL, with constant compartment size.

r/R	r / μm	A_{DIB} / cm^2	t / min
0.1	20.5	1.32×10^{-5}	500.0
0.2	41	5.28×10^{-5}	125.0
0.3	61.5	1.19×10^{-4}	55.6
0.4	82	2.11×10^{-4}	31.3
0.5	102.5	3.30×10^{-4}	20.0
0.6	123	4.75×10^{-4}	13.9
0.7	143.5	6.47×10^{-4}	10.2
0.8	164	8.45×10^{-4}	7.8
0.9	184.5	1.07×10^{-3}	6.2

2.6.3 Effect of compartment size

In Section 2.6.2, the DIB radius r was varied for compartments of constant size (R = 205 μm) and the time for equilibration of 2-NBDG across our DIB system was estimated. The compartment size also affects the equilibration times of a chemical signal across the bilayer. We now vary the radius of the compartments, R, to calculate the expected equilibration times of 2-NBDG across the DIB permabilised by αHL, assuming $r = R/2$. We use Equation 2.3 to calculate N for each compartment size. We use the values of ΔC and $P_{\text{2-NBDG, DIB+}\alpha\text{HL}}$ from Section 2.6.1. For a range of compartment radii where 50 μm $\leq$ R $\leq$ 400 μm (0.5 nL $\leq$ V $\leq$ 268 nL), we obtain the equilibration times of 2-NBDG across a DIB permeabilized by αHL ranging from minutes to tens of minutes (Table

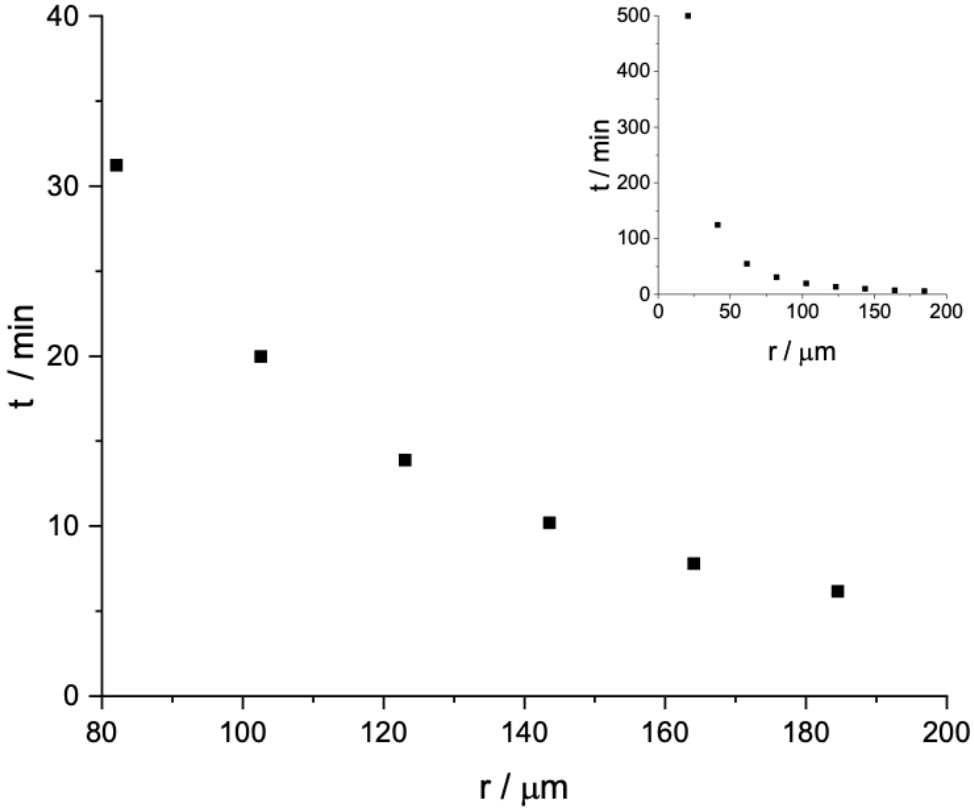


Figure 2.14: Effect of bilayer area on the equilibration time of a chemical signal across a DIB permeabilized by αHL. Effect of bilayer area, as indicated by bilayer radius r, on the equilibration time t of 2-NBDG across a DIB permeabilised by αHL. Inset: Equilibration times for a wider range of r.

2.2). As the compartment volume increases with compartment radius R, the number of molecules inside the compartment increases by R^3 and the DIB area increases by R^2. Therefore, the equilibration time for a chemical signal across the compartments increases by $R^3/R^2 = R$ (Fig. 2.15).

Table 2.2: Effect of bilayer area on 2-NBDG equilibration by diffusion across a DIB permeabilised by αHL, with constant compartment size.

R / µm	r / µm	V / nL	A_{DIB} / cm^2	N	t / min
50	25	0.52	1.96×10^{-5}	2.62×10^{-7}	4.9
100	50	4.19	7.85×10^{-5}	2.09×10^{-6}	9.8
150	75	14.14	1.77×10^{-4}	7.07×10^{-6}	14.6
200	100	33.51	3.14×10^{-4}	1.68×10^{-5}	19.5
250	125	65.45	4.91×10^{-4}	3.27×10^{-5}	24.4
300	150	113.10	7.07×10^{-4}	5.65×10^{-5}	29.3

Continued on next page

Table 2.2 – *Continued from previous page*

R / µm	r / µm	V / nL	A_{DIB} / cm²	N	t / min
350	175	179.59	9.62×10^{-4}	8.98×10^{-5}	34.2
400	200	268.08	1.26×10^{-3}	1.34×10^{-4}	39.0

2.6.4 Estimation of αHL pore number and density

Given our results, we can also estimate the number and density of inserted αHL pores in the DIBs. We calculated the permeability of the DIB permeabilised with αHL for 2-NBDG, $P_{\text{2-NBDG, DIB+}\alpha\text{HL}}$, in Section 2.6.1. This value is the 'apparent' permeability, ie. it treats the bilayer as a homogenous semi-permeable membrane. In reality, the bilayer contains areas of lipids where the permeability is negligible and αHL pores where the permeability, $P_{\text{2-NBDG, }\alpha\text{HL}}$, is much higher. We will use this aspect of the system to estimate the number and density of the pores.

From Equation 2.2, $P_{\text{2-NBDG, DIB+}\alpha\text{HL}}$ and ΔC from Section 2.6.1, $J_{\text{2-NBDG, DIB+}\alpha\text{HL}} = 4.6\times10^{-5}$ µmol cm^{-2} s^{-1}. Using A_{DIB} from Section 2.6.1, the rate of of diffusion of 2-NBDG through the semipermeable bilayer is $R_{\text{2-NBDG, DIB+}\alpha\text{HL}} = J_{\text{2-NBDG, DIB+}\alpha\text{HL}} A_{\text{DIB}} = 1.52 \times 10^{-8}$ µmol s^{-1}.

Since the diffusion of 2-NBDG through the areas of the DIB with no pores is negligible, rate of diffusion of 2-NBDG through the αHL pores, $R_{\text{2-NBDG, }\alpha\text{HL}}$, is equal to the rate of diffusion of 2-NBDG through the entire DIB:

$$R_{\text{2-NBDG, }\alpha\text{HL}} = R_{\text{2-NBDG, DIB+}\alpha\text{HL}} \tag{2.6}$$

Therefore, rate of diffusion of 2-NBDG through the αHL pores is:

$$R_{\text{2-NBDG, }\alpha\text{HL}} = J_{\text{2-NBDG, }\alpha\text{HL}} A_{\alpha\text{HL}} \tag{2.7}$$

where $R_{\text{2-NBDG, }\alpha\text{HL}} = 1.52 \times 10^{-8}$ µmol s^{-1}, $J_{\text{DIB+}\alpha\text{HL}}$ is the flux of 2-NBDG through the pores and $A_{\alpha\text{HL}}$ is the total area of the pores in the DIB. We can then calculate $J_{\text{2-NBDG, }\alpha\text{HL}}$ from:

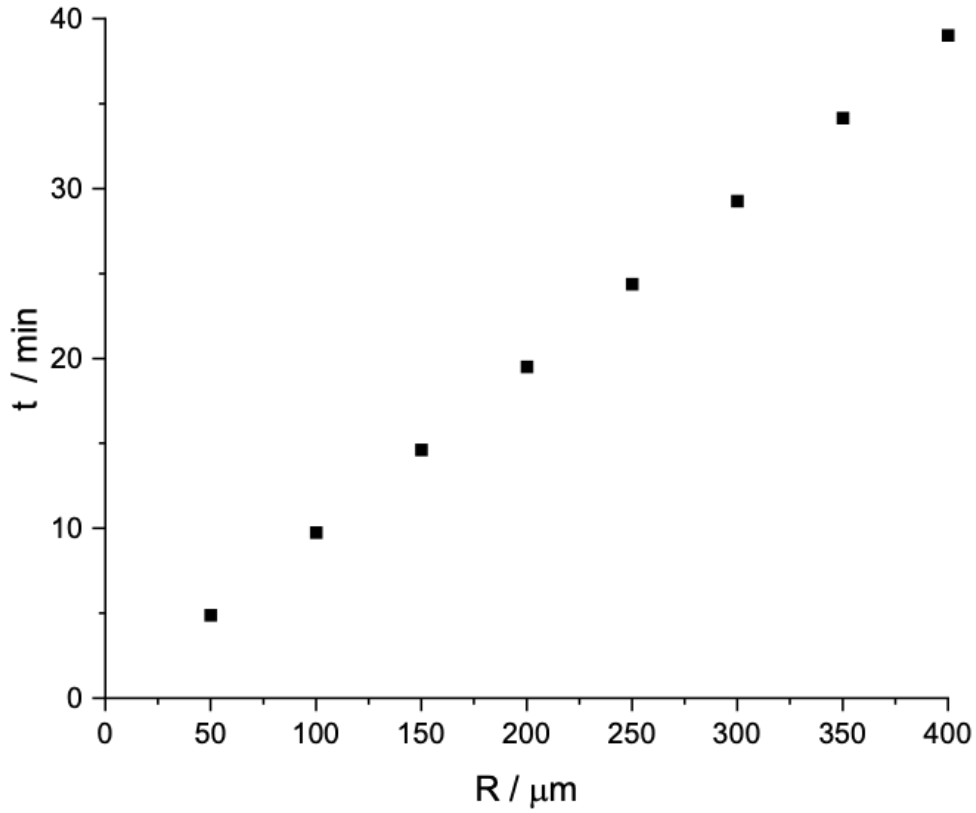


Figure 2.15: Effect of compartment size on the equilibration time of a chemical signal across a DIB permeabilised by αHL. Effect of compartment size, as indicated by compartment radius R, on the equilibration time t of 2-NBDG across a DIB permeabilised by αHL.

$$J_{\text{2-NBDG, }\alpha\text{HL}} = \frac{-D\Delta C}{L} \tag{2.8}$$

where D is the diffusion coefficient of the solute in bulk aqueous solution and L is the distance over which the molecules diffuse[128]. For diffusion through αHL pores, L is the length of the pore. Using D = 650 μm^2 s^{-1} for a water impermeable molecule and $L = 5 \times 10^{-9}$ m for αHL[129], $J_{\text{2-NBDG, }\alpha\text{HL}} = 1.30 \times 10^5$ μmol m^2 s^{-1}.

Using the values of $R_{\text{2-NBDG, }\alpha\text{HL}}$ and $J_{\text{2-NBDG, }\alpha\text{HL}}$ in Equation 2.7, we obtain $A_{\alpha\text{HL}} = 1.17 \times 10^{-13}$ m^2. Based on a pore diameter of 1.2 nm[47], the area of each pore $a_{\alpha\text{HL}} = 1.13 \times 10^{-18}$ m^2. The number of αHL pores in the DIB can then be estimated as $N_{\alpha\text{HL}} = A_{\alpha\text{HL}}/a_{\alpha\text{HL}} = 103000$. The pore density can be estimated as $\rho = N_{\alpha\text{HL}}/A_{\text{DIB+}\alpha\text{HL}} = 3.13 \times 10^{12}$ pores m^{-2}. For comparison, a previous study investigating αHL synthesised with cell-free expression at the stabilised DIB

used similar calculations and estimated a pore density of 4.90×10^{10} pores m^{-2}, which is two orders of magnitude smaller than achieved in our system[128].

The values for pore density and the number of inserted pores are underestimates. The 20 min equilibration time used for 2-NBDG in these calculations includes the time of bilayer formation and pore insertion. The actual rate of diffusion in the stabilised system is higher, therefore the number and density of αHL pores are higher than the estimations here.

2.7 Conclusion

We have achieved fast rates of molecular equilibration by diffusion through αHL pores within minutes in our system. Diffusion of molecules such as pyranine[101], guanine[93], glucose[115], and 3-carboxyumbelliferyl-β-D-galactopyranoside (CUG)[112], were previously observed over tens of minutes, hours or days. Using purified recombinant monomers, we were able to encapsulate 200 µg mL^{-1} of αHL inside the signal transmission compartment here and in the structures shown later in this work, without any adverse effects on the structures. This concentration is much higher than those used in previous studies[12,70,93,94,101,114,115], which were tens of µg mL^{-1}. We attribute the ability to include high concentrations of αHL in this work to the absence of additives in the purified protein sample. The rapid molecular diffusion allowed by high concentrations of αHL will be crucial when building the droplet processors in the following chapters.

We have also visualised the diffusion of 2-NBDG across DIBs permeabilised by αHL. We characterised the changing rates of molecular diffusion and pore insertion as the DIB forms and the concentration gradient of the chemical signal changes. We have also demonstrated the effect of different lipids used on the diffusion of 2-NBDG across DIBs permeabilised by αHL. We discussed diffusion scenarios with no membrane, with a membrane, and with a membrane permeabilised by αHL. We highlighted the effects of compartment size and DIB area on the diffusion rate of a chemical signal across the DIB. We then quantified

the permeability of our DIBs and pores to 2-NBDG and estimated the number and density of αHL pores inserted into the DIB.

In addition, we demonstrated molecular diffusion using recombinant αHL for the first time, with expression in *E. coli* and straightforward His-tag purification followed by size exclusion chromatography. As the previous examples demonstrating ionic or molecular diffusion employed αHL isolated from the natively expressing *S. aureus*, they relied on the wild-type form of the protein. The ability to use recombinant αHL from *E. coli* opens up the possibility of easy genetic modification and bulk production of these pores in a well-established host organism[130]. Novel pores could therefore be generated at low cost and used for controlled diffusion of molecules (see Chapter 6).

3

Exchange of chemical signals with the external environment

Contents

3.1 Introduction 49
3.2 Signal release to an external aqueous environment by two-compartment structures 50
3.3 Signal intake and sensing from an external aqueous environment by two-compartment processors 51
3.4 Conclusion 54

3.1 Introduction

We established fast molecular diffusion across DIBs containing in situ heptamerised recombinant αHL within a lipid-oil external environment in Chapter 2. Here, we turn to structures within an external aqueous environment and establish exchange of chemicals between the structures and their environment. In our processors, chemical signals must diffuse not only between the compartments within the structure, but also between the structure and its external aqueous environment. Therefore, a chemical output released from a processing compartment must diffuse through two bilayers: first through the internal

bilayer joining this compartment and the signal transmission compartment, then through the external bilayer joining the signal transmission compartment and the external aqueous environment. Similarly, a chemical input received from the external environment must diffuse through two bilayers: first through the external bilayer joining the external aqueous environment and the signal transmission compartment, then through the internal bilayer joining the signal transmission compartment and the relevant processing compartment.

In this chapter, we make two-compartment structures within an external aqueous environment. We first form the two aqueous compartments separately in a lipid-containing oil external environment, and then transfer them into a lipid-containing oil drop suspended on a wire loop within an aqueous environment. The aqueous compartments sink to the bottom of the oil drop and form lipid bilayers with the external aqueous compartment. The signal transmission compartment contains αHL which forms pores in the bilayers joining this compartment to the other internal aqueous compartment and to the external aqueous environment. Using two-compartment structures, we show release of molecules through two bilayers into the external environment, and intake of external ions through two bilayers into a sensing compartment.

3.2 Signal release to an external aqueous environment by two-compartment structures

In droplet processors with molecular outputs, the product molecules would need to diffuse through the αHL pores into the external aqueous environment. To mimic the release of a molecular output generated inside a processing compartment to the external environment, we made two-compartment structures comprising a signal transmission compartment with 200 μg mL^{-1} αHL monomers and a signal release compartment with 1 mM 2-NBDG (Fig. 3.1a). Diffusion of 2-NBDG through the internal bilayer, observed as colour change in the signal transmission compartment, began while the external bilayer was still forming,

observed as a growing circle in the signal transmission compartment. The 2-NBDG molecules were completely released to the external aqueous environment within 10 min (n = 3, Fig. 3.1b). As a negative control, we constructed two-compartment processors with no αHL in the signal transmission compartment and did not observe release of 2-NBDG (n = 3, Fig. 3.1c) after 1 h.

3.3 Signal intake and sensing from an external aqueous environment by two-compartment processors

Droplet processors with external activation would need to receive a chemical signal from the external aqueous environment. If used as sensors, they would also need to produce a fluorescence signal as an output. To show the intake and sensing of an external chemical signal by a processing compartment, we chose Ca^{2+} as an external signal and Rhod-2, a dye that shows increased fluorescence upon binding to Ca^{2+}, as a reporter. We made two-compartment structures comprising a signal transmission compartment with 200 μg mL^{-1} αHL monomers and a sensing compartment containing 20 μM dextran-conjugated fluorescent Ca^{2+} indicator Rhod-2 (MW $\approx$ 11,000) (Fig. 3.2a). As the output in this case is fluorescence rather than release of a molecule, we chose to minimise reagent use by employing a 300-350 μm diameter (14-23 nL volume) sensing compartment, along with the 500-650 μm diameter (65-144 nL volume) signal transmission compartment. As we expected trace metal ions to be present in the aqueous solutions, we included 2 μM 1,2-bis(o-aminophenoxy)ethane-N,N,N',N'-tetraacetic acid (BAPTA), a non-fluorescent chelator, in the sensing compartment and the external aqueous environment. The K_d for Ca^{2+} of BAPTA[131] is ~160 nM while that of Rhod-2[132] is ~3.8 μM, therefore the BAPTA should bind to the trace metal ions much more strongly than Rhod-2. With addition of Ca^{2+}, the 2 μM BAPTA should quickly become saturated, allowing the Rhod-2 to also bind to the added Ca^{2+} and exhibit higher fluorescence. BAPTA was chosen as a chelator

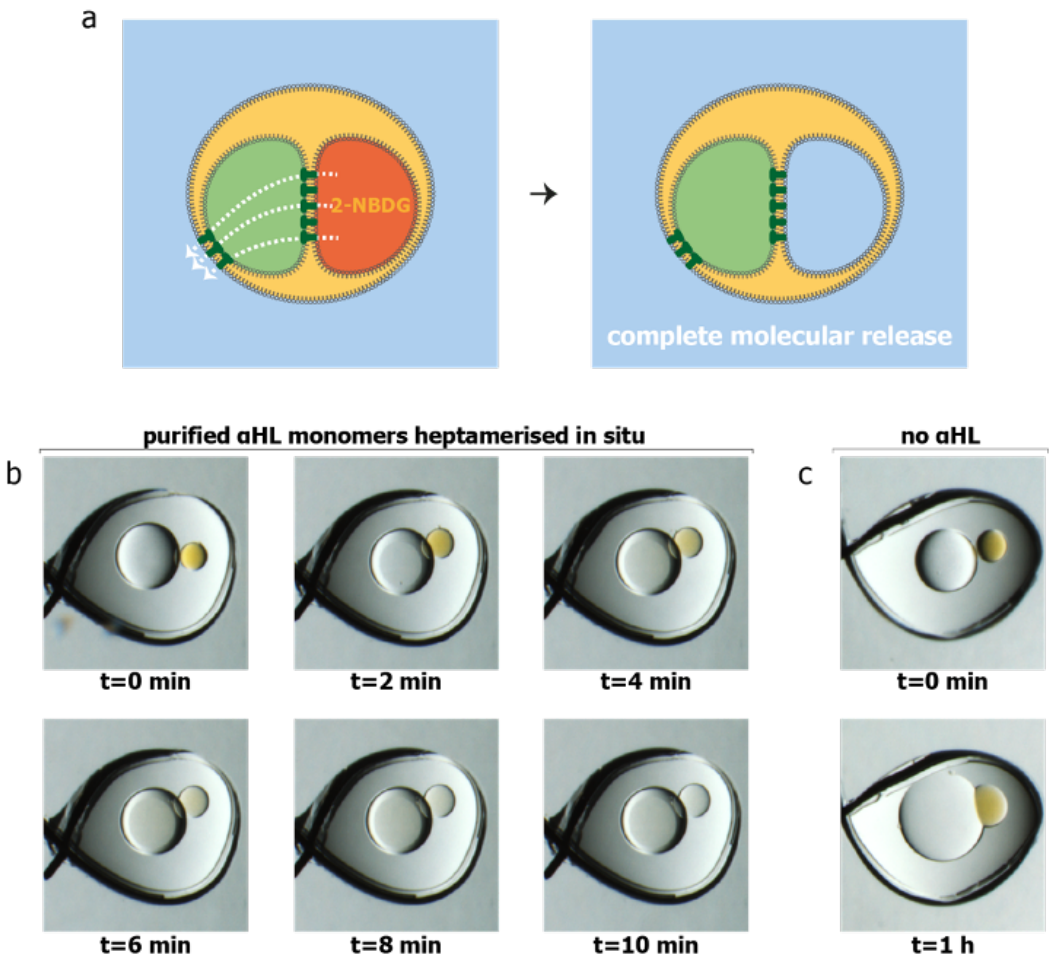


Figure 3.1: Output of a molecular signal from two-compartment structures to an external aqueous environment. a. Diffusion of 2-NBDG through a signal transmission compartment, followed by its release into the external aqueous environment. **b-c** Bright-field microscopy images of 2-NBDG diffusion into the external aqueous environment through a signal transmission compartment containing purified αHL monomers (b) or no αHL (c). Wire diameter = 76 µm.

instead of ethylenediaminetetraacetic acid (EDTA) and ethylene glycol-bis(β-aminoethyl ether)-N,N,N',N'-tetraacetic acid (EGTA) due to its higher selectivity for Ca^{2+} and lower sensitivity to pH compared to EDTA and EGTA, and higher rate of binding to Ca^{2+} compared to EGTA[131].

After addition of 10 mM Ca^{2+} to the external aqueous environment and 1 h incubation, we observed a 3-fold increase in the fluorescence in the sensing compartment (n = 4, Fig. 3.2b, c). Without Ca^{2+} addition, we observed not an increase, but a decrease in fluorescence in the sensing compartment (n = 3,

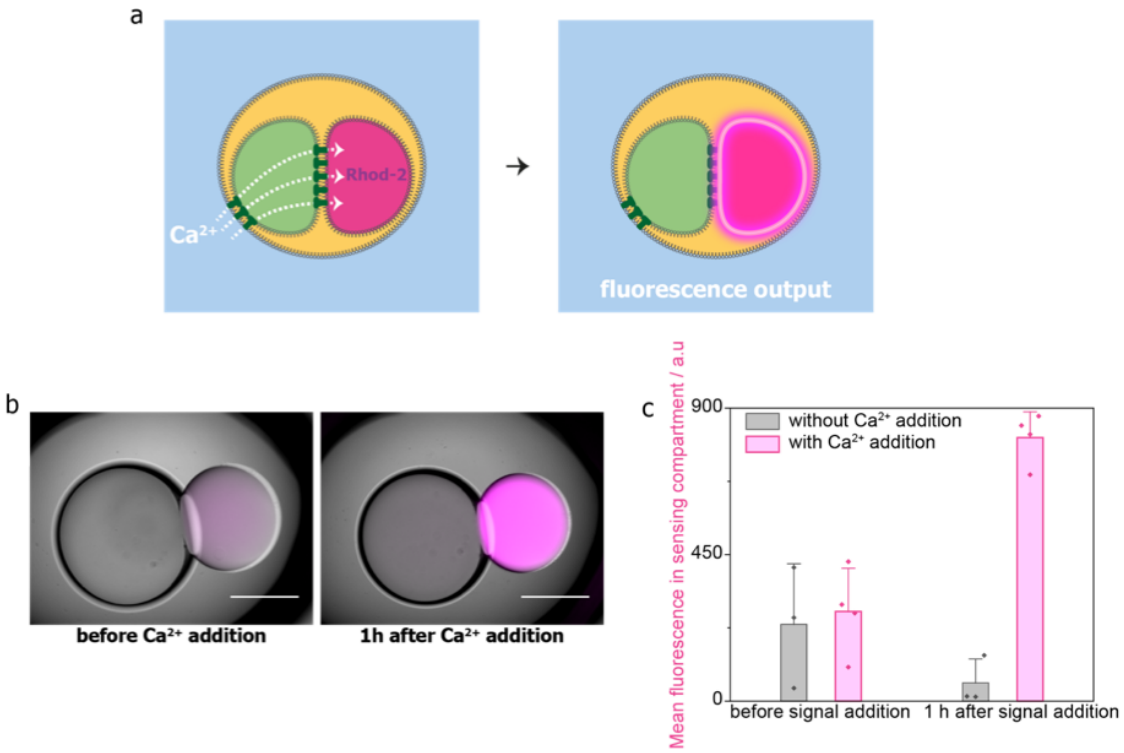


Figure 3.2: Intake and sensing of an external ionic signal by two-compartment structures. a. Intake of ionic signal Ca^{2+} through the signal transmission compartment into the sensing compartment which contains dextran-conjugated Rhod-2, and production of a fluorescence output in the sensing compartment. **b.** Composite bright-field and epifluorescence images of two-compartment structures before and 1 h after Ca^{2+} addition to the external aqueous environment. Scale bars = 300 µm. **c.** Mean fluorescence values of the sensing compartment before and after Ca^{2+} addition and 1 h incubation, without (n = 3) and with (n = 4) Ca^{2+} addition. Error bars = standard deviation.

Fig. 3.2c). In this case, excess BAPTA from the external aqueous environment diffused through the αHL pores and competed with Rhod-2 to bind the trace metal ions, reducing the fluorescence in the sensing compartment even further. These experiments also demonstrate that an output signal can be not only positive but also negative. The diffusion of BAPTA (MW ≈ 472), once again demonstrates the fast diffusion of molecular signals through the αHL pores in this work. In previous setups with lower αHL concentration[93,101,112], molecules with MW similar to or less than that of BAPTA had slower rates of diffusion, observed over hours to days.

3.4 Conclusion

In this chapter, we have demonstrated release of a molecular signal and intake of an ionic signal by two-compartment structures. Using recombinant αHL monomers, we have demonstrated fast release of a molecular output signal from a two-compartment structure to its external aqueous environment. The molecules diffused through the internal bilayer to reach the signal transmission compartment and through the external bilayer to reach the external aqueous environment. In this setup, the encapsulated 2-NBDG was completely released within 10 min. We have also demonstrated diffusion of an ionic input signal from the external aqueous environment into a sensing compartment. The ions diffused through the external bilayer to reach the signal transmission compartment and through the internal bilayer to reach the sensing compartment, resulting in a fluorescence output. Exchange of chemicals with the external aqueous environment is crucial for this work, where chemical input and output signals must diffuse through several bilayers, and the chemical output signals become diluted upon release into the external environment.

4

Two-compartment processors

Contents

4.1 Introduction 55
4.2 Enzymatic process with a fluorescence output: DNA cleavage . 56
4.2.1 Reaction design 56
4.2.2 Reaction tests in bulk 58
4.2.3 Encapsulation in two-compartment processors 59
4.3 Enzymatic process with a molecular output: Hydrolysis 62
4.3.1 Reaction and product detection 62
4.3.2 Reaction tests in bulk 64
4.3.3 Encapsulation in two-compartment processors 66
4.4 Conclusion 69

4.1 Introduction

Having shown fast diffusion of molecules through recombinant αHL pores in a lipid-oil environment in Chapter 2, and exchange of chemical signals with an external aqueous environment in Chapter 3, we next couple signalling with internal processes. In this chapter, we build two-compartment processors containing a signal transmission compartment and an enzymatic processing compartment. We first demonstrate intake of an ionic signal, Mg^{2+}, and its processing to initiate DNA cleavage by EcoRI with a fluorescence output signal.

Then, we demonstrate intake of a molecular signal, lactose, and its enzymatic hydrolysis by β-galactosidase. We show the release of the molecular output signal, glucose, into the external aqueous environment.

4.2 Enzymatic process with a fluorescence output: DNA cleavage

4.2.1 Reaction design

As the first enzyme, we selected EcoRI, a type II restriction endonuclease from *E. coli* which requires Mg^{2+} as a co-factor[133] to cleave double stranded DNA at the site G ↓AATTC (with the palindromic complementary sequence of CTTAA ↓G). We chose this enzymatic reaction to exemplify the case where an ionic input signal activates an internal process, resulting in a fluorescence output signal. To our knowledge, this reaction has not been previously encapsulated in synthetic biological systems.

As the substrate for the EcoRI reaction, we designed a molecular beacon, hairpin-shaped DNA molecule with loop and stem regions containing a fluorophore (donor chromophore) and a quencher (acceptor chromophore) attached at either end of the stem region. Upon illumination at suitable wavelengths, energy from the excited fluorophore is transferred nonradiatively to the quencher, a mechanism known as to Förster resonance energy transfer (FRET)[134]. The excited quencher dissipates this energy as heat rather than light. A 'dark' quencher has no native fluorescence[135]. The FRET efficiency is inversely proportional to the 6th power of the distance between the fluorophore and quencher[134]. As the pair separates, FRET efficiency rapidly decreases and the fluorescence of the fluorophore is observed. Therefore, fluorescence measurements serve as a sensitive indication of the distance between the pair. The degree of overlap between the fluorophore's emission spectrum and the quencher's absorption spectrum is an important factor in quenching efficiency[134].

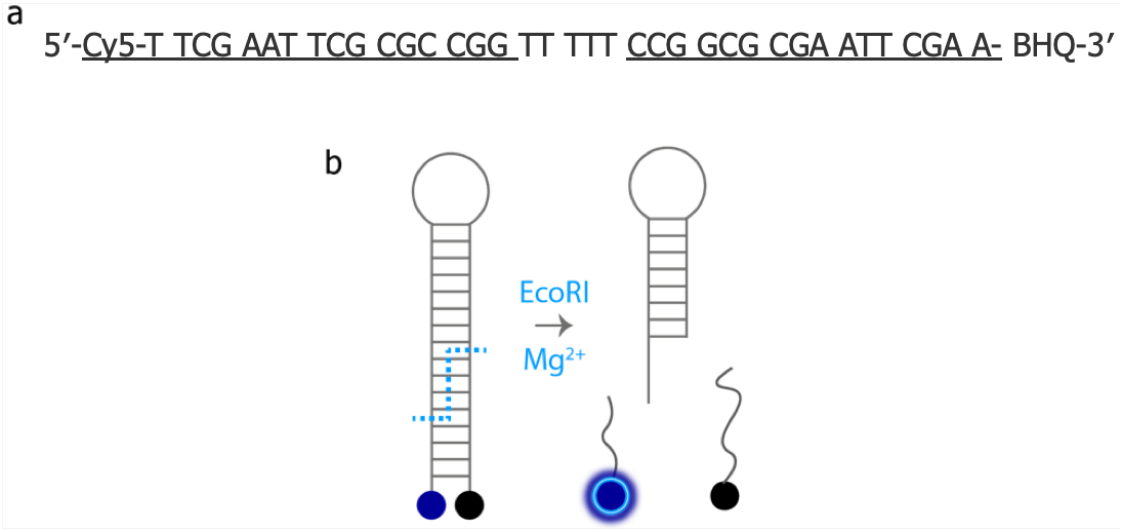


Figure 4.1: Mg^{2+}-activated DNA cleavage by EcoRI with a fluorescence output. a. DNA sequence forming the molecular beacon substrate with the fluorophore Cy5 and quencher BHQ-3 attached on 5' and 3' ends, respectively. Underlined bases represent the stem region. **b.** Activated by its Mg^{2+} cofactor, EcoRI cleaves at its recognition site, leading to strand separation and a fluorescence output signal.

We designed the substrate based on a previously published DNA sequence with an EcoRI cleavage site 4 and 8 bases away from 5' and 3' ends, respectively (Fig. 4.1a)[136]. Upon cleavage of the DNA molecule by EcoRI, the fluorophore-quencher pair remains on a short piece of dsDNA with only 4 nucleotide pairs. As this DNA piece has a low melting temperature, the double strand separates into two single strands, separating the fluorophore-quencher pair and resulting in a fluorescent signal (Fig. 4.1b). The previously published molecular beacon contained 5(6)-carboxytetramethylrhodamine (TAMRA) as the fluorophore and 4-(dimethylaminoazo)benzene-4-carboxylic acid (DABCYL) as the quencher[136]. TAMRA has an emission maximum at 575 nm while DABCYL has an absorption maximum at 475 nm[137], so this pair would not provide optimal quenching. As we aimed for a strong difference in fluorescence between the off and on states of the EcoRI enzyme, we chose a fluorophore-quencher pair with large spectral overlap: Cyanine 5 (Cy5) and Black Hole Quencher-3 (BHQ-3), with an emission and absorption maxima at 670 nm, respectively[137]. Cyanine dyes and BHQs have been reported to engage in static quenching in addition to FRET quenching[138]. In static quenching, the fluorophore and quencher aggregate and

stick together, forming a ground state complex prior to excitation[139,140]. Static quenching results from electrostatic, steric, and hydrophobic forces between the pair[139]. The resulting complex has a unique absorption spectrum and is non-fluorescent. Therefore, static quenching suppresses the background fluorescence of the fluorophores[139], enabling strong differences between the 'on' and 'off' states in our system.

4.2.2 Reaction tests in bulk

Prior to encapsulating the enzymatic DNA cleavage reaction in processors, we tested it in bulk. We used 364 U mL^{-1} EcoRI, 364 nM DNA and 91 µg mL^{-1} bovine serum albumin (BSA) with 0 or 10 mM Mg^{2+} and at pH values 5.5, 6.5 or 8.0. Using a fluorescence microplate reader, we measured the fluorescence generated in each reaction mix for 3 h at 37 °C (Fig. 4.2). We confirmed that no fluorescence was generated without Mg^{2+} at any of the pH conditions (n = 3 for each pH condition). At pH 5.5, no fluorescence signal was generated with Mg^{2+} either, indicating that this pH condition was not suitable for the reaction. Fluorescence signals were generated at both pH 6.5 and pH 8.0. The increase in signal was faster at pH 8.0, where the signal saturated at a maximum in ~1 h. Despite increasing more slowly, over 2 h the fluorescence signal at pH 6.5 reached the same maximum as pH 8.0. Due to pH requirements of three-compartment processors encapsulating EcoRI and β-galactosidase reactions (see Fig. 4.9), we decided to use pH 6.5 for the two-compartment processors in this section.

We also tested the reaction in bulk with varying concentrations of BSA which is typically included in restriction enzyme buffers such as EcoRI. We observed no activity without BSA, and increasing activity with increasing BSA concentration (Fig. 4.3). We therefore decided to use 100 µg mL^{-1} BSA in all remaining experiments. Since our work, buffers containing recombinant albumin instead of BSA have also become available[141], so recombinant albumin could be used in future work.

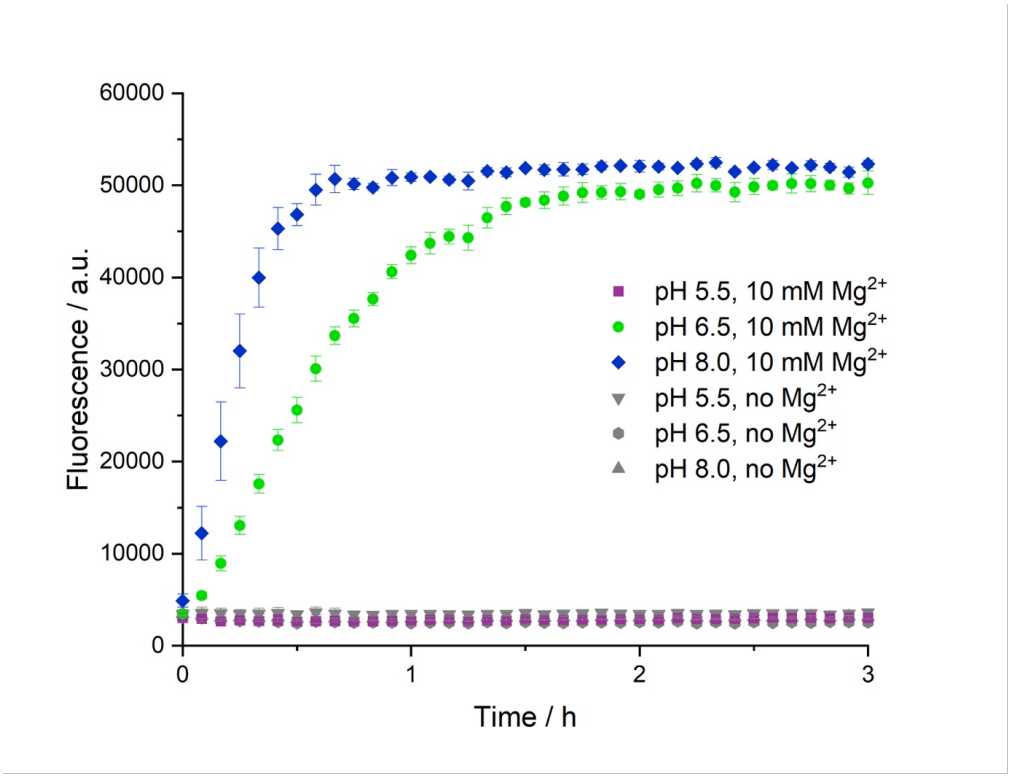


Figure 4.2: DNA cleavage activity of EcoRI at various pH values, with or without Mg^{2+}. The fluorescent product was measured in bulk. DNA cleavage by EcoRI did not proceed without Mg^{2+} (n = 3 for each pH condition). The EcoRI enzyme was highly active at pH 8.0 (n = 3). Reduced activity rate but complete reaction was observed at pH 6.5 (n = 3), whereas no activity was observed at pH 5.5 (n = 3). Error bars = standard deviation.

4.2.3 Encapsulation in two-compartment processors

We built two-compartment processors containing a signal transmission compartment along with an enzymatic processing compartment with 400 U mL^{-1} EcoRI and 400 nM DNA substrate. We also included 100 µg mL^{-1} bovine serum albumin (BSA) in the enzymatic processing compartment and obtained stable structures despite the known ability of BSA to bind lipids[142,143]. As the process in these structures had a fluorescence output, we used a 300-350 µm diameter enzymatic processing compartments to minimise reagent use, and 500-650 µm diameter signal transmission compartments. Mg^{2+} added into the external aqueous environment should diffuse through the external and internal bilayers, activating EcoRI in the enzymatic processing compartment and leading to cleavage of the DNA molecule and generation of a fluorescence output signal (Fig. 4.4a).

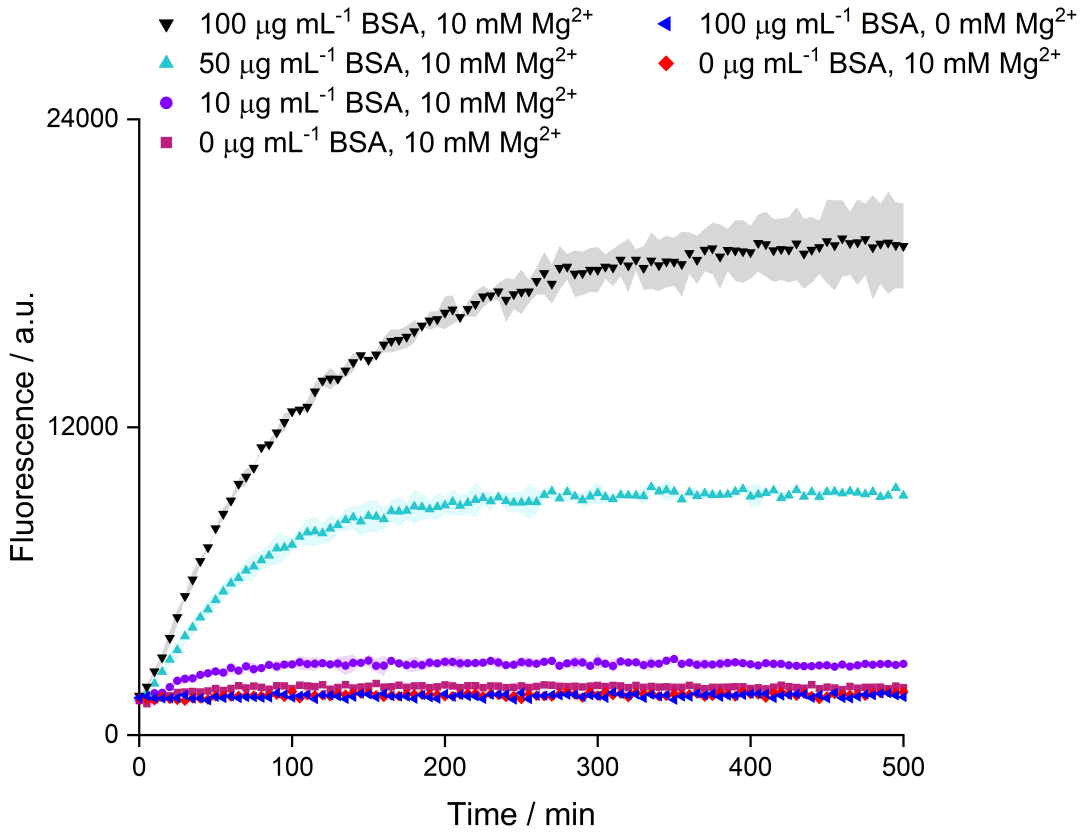


Figure 4.3: DNA cleavage activity of EcoRI at various with various concentrations of BSA, with or without Mg^{2+}. The fluorescent product was measured in bulk containing 10 mM $Mg^{2+}$with 0, 10, 50 or 100 μg mL^{-1} BSA (n = 2 for each BSA concentration) and containing no Mg^{2+} with 0 or 100 μg mL^{-1} BSA (n = 2 for each BSA concentration). Shaded areas = standard deviation.

We carried out initial experiments with 200 μg mL^{-1} αHL monomers in the signal transmission compartment. We added 10 mM Mg^{2+} into the external aqueous environment and incubated the processors at 37 °C for 2 h. Even though similar reaction conditions had resulted in a fluorescence output signal in bulk experiments (Fig. 4.2), we did not detect any fluorescence signal in the EcoRI+DNA compartment. We hypothesised that the fluorescent product could be diffusing out through the αHL pores. To test this hypothesis, we made structures with a lower αHL concentration in the signal transmission compartment (see Section 7.2), with no changes to other experimental conditions. We were then able to detect a fluorescence output signal after Mg^{2+} addition and incubation at 37 °C (Fig. 4.4b, c). We did not observe any fluorescence output

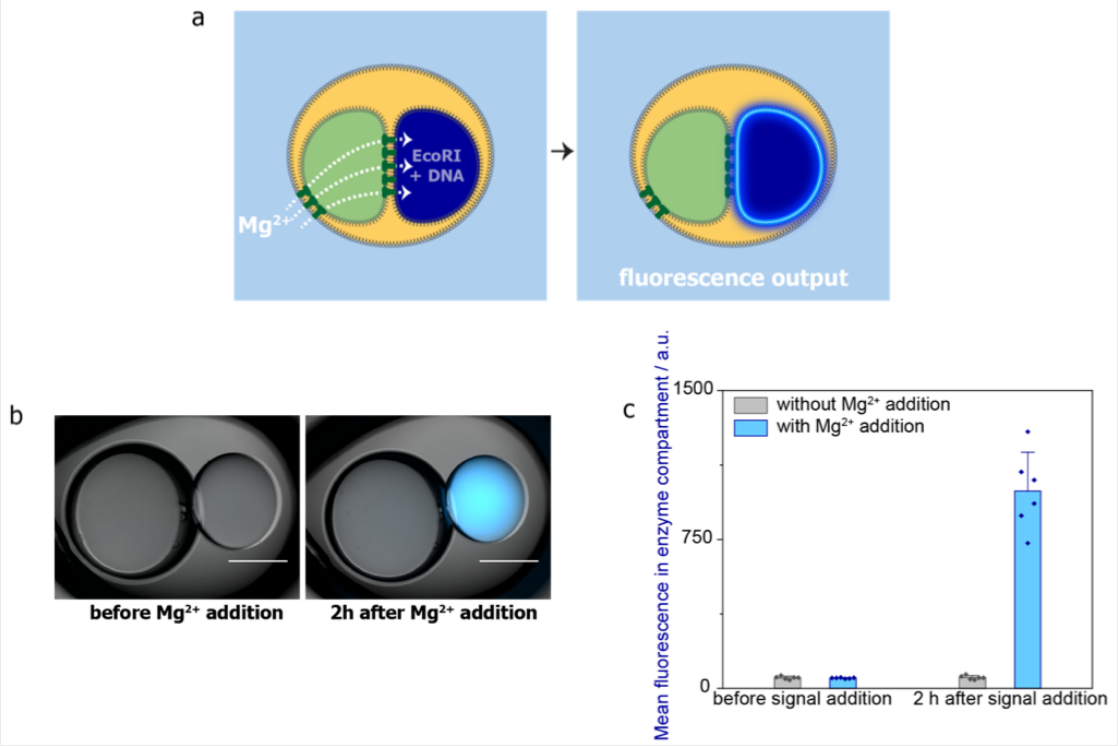


Figure 4.4: Enzymatic DNA cleavage in two-compartment processors with a fluorescence output. a. Mg^{2+} input signal diffused through the external and internal pores and activates DNA cleavage by EcoRI. **b.** Composite bright-field and epifluorescence images of a two-compartment processor containing EcoRI and DNA before and after Mg^{2+}addition into the external aqueous environment and 2 h incubation at 37 °C. Scale bars = 300 µm. **c.** Mean fluorescence values of the enzymatic processing compartment before and after Mg^{2+} addition and 2 h incubation at 37 °C without (n = 6) and with (n = 6) Mg^{2+} addition. Error bars = standard deviation.

signal without Mg^{2+} addition (Fig. 4.4c).

The improvement of the fluorescence signal with a lower αHL concentration indicated that the fluorescent product was diffusing out of the reaction compartment through the pores. We analysed the fluorescence along the diameters of the signal transmission compartments (Fig. 4.5a). Our analysis confirmed that when Mg^{2+} input signal was added in the external environment and a fluorescence output was generated in the EcoRI+DNA compartment, some fluorescence could be detected also in the signal transmission compartment (n = 6, Fig. 4.5b). The fluorescent product in the stuctures with high αHL concentration diffused out through the pores, preventing the detection of the fluorescence output signal.

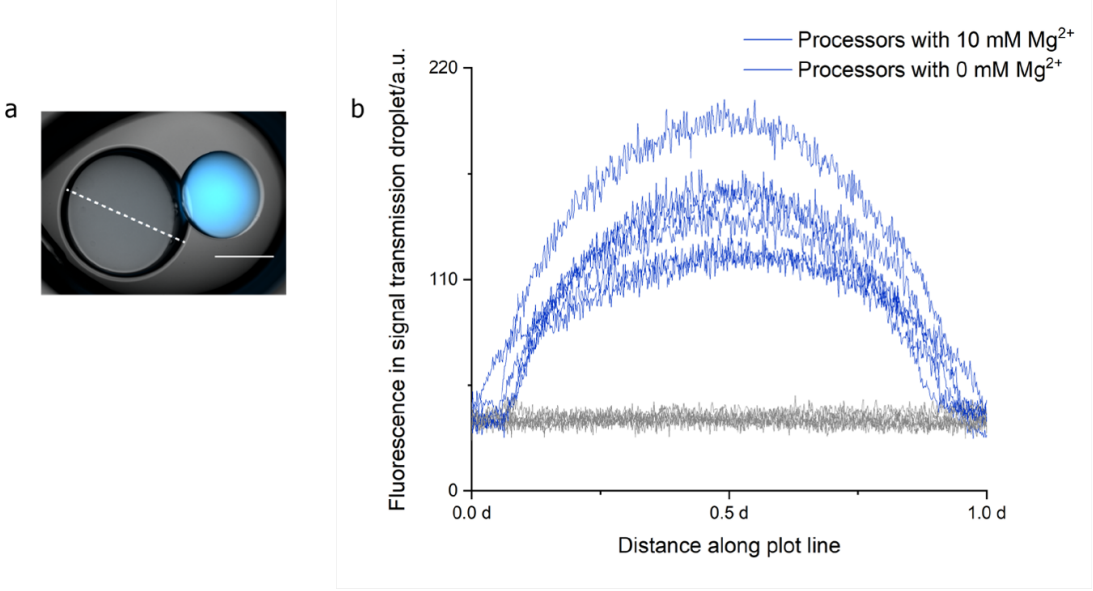


Figure 4.5: Fluorescence in the signal transmission compartment after enzymatic DNA cleavage in two-compartment processors. **a.** Fluorescence of each signal transmission compartment with reduced αHL concentration was analysed by drawing a line across the compartment diameter, indicated as a white dashed line. **b.** Fluorescence values across the diameter (d) of each signal transmission compartment. Processors that received a Mg^{2+} input signal showed fluorescence in their signal transmission compartments (n = 6). Processors with no Mg^{2+} addition showed no fluorescence in their signal transmission compartments (n = 6).

4.3 Enzymatic process with a molecular output: Hydrolysis

4.3.1 Reaction and product detection

As the second internal process, we used enzymatic hydrolysis of lactose by β-galactosidase. Lactose is a sugar molecule formed by the covalent linkage of

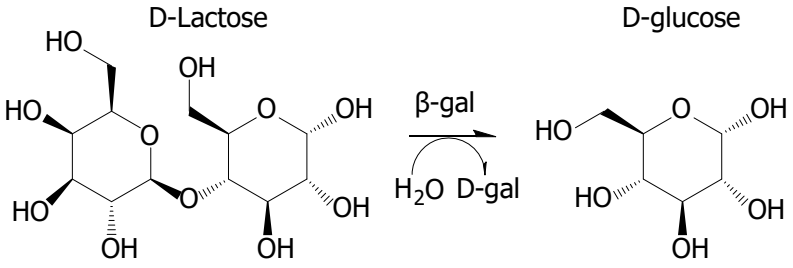


Figure 4.6: Enzymatic processing with a molecular output. D-lactose is hydrolysed by β-galactosidase (β-gal) into D-galactose (D-gal) and D-glucose.

two simple sugars: glucose and galactose. β-galactosidase hydrolyses sugar molecules that contain a galactose into their constituent simple sugars. We chose this enzymatic reaction to exemplify the case where a molecular input signal produces a molecular output signal that then diffuses through the αHL pores into the external aqueous environment. The output signal glucose can be detected with a commercially available assay kit. This enzyme is very common in nature and is found a wide range of organisms: in plants, animals, yeast, bacteria and fungi[144,145]. It also has various industrial applications[145]. Upon activity by the β-galactosidase enzyme, D-lactose becomes hydrolysed into D-glucose and D-galactose (D-gal) (Fig. 4.6). In this work, we used β-galactosidase from the fungus *A. oryzae*.

We detected the molecular output glucose using the ThermoFisher Amplex Red Glucose/Glucose Oxidase Assay Kit. The assay kit contains glucose oxidase, horseradish peroxidase and amplex red. Glucose oxidase generates hydrogen peroxide from glucose, and horseradish peroxidase uses the generated hydrogen peroxide to convert amplex red into fluorescent resorufin (Fig. 4.7). A glucose calibration curve is employed to calculate the glucose concentration corresponding to the detected fluorescence values for each sample.

As the glucose detection also relies on enzymatic reactions, we tested the effect of lactose and pH on these reactions. We prepared glucose standards with 0 or 40 mM lactose and at pH 5.5, 6.5 or 8.0 and used the glucose detection kit to measure fluorescence values from each condition (n = 3 for each condition, Fig. 4.8). We made and analysed separate glucose calibration curves for every

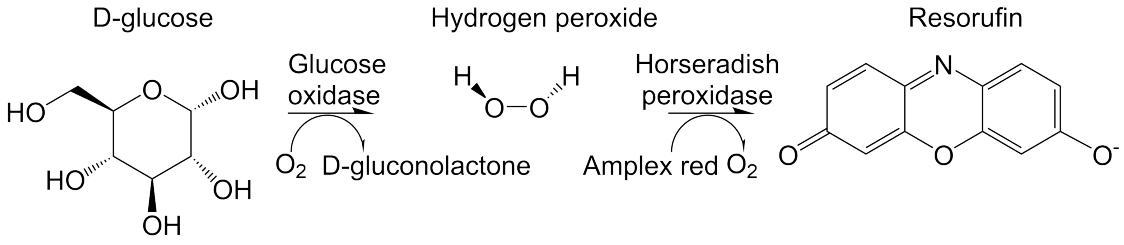


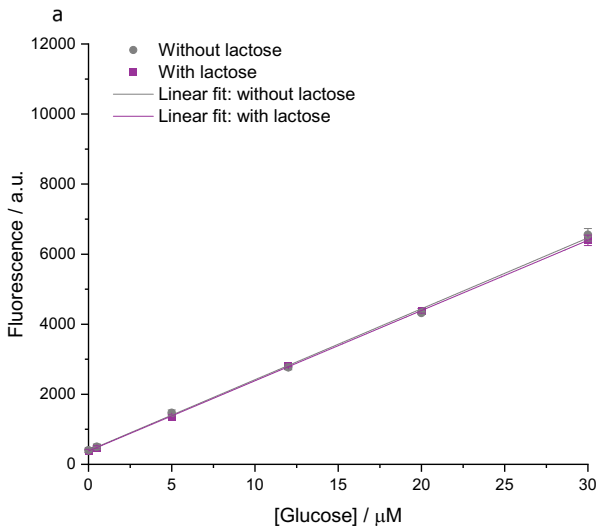
Figure 4.7: Enzymatic conversion of glucose into fluorescent resorufin. The glucose detection assay kit performs an enzymatic cascade reaction to generate fluorescent resorufin from glucose.

pH condition with and without lactose using linear regression. For the same concentrations of glucose, the fluorescence values at pH 5.5 were lower than those at pH 6.5 or 8.0. However, the data shown in the three plots (Fig. 4.8) were collected in three different experiments and aimed to investigate any effect of lactose on the detection of glucose using the glucose detection kit, i.e. to compare each pair of linear regressions within itself and not between different pairs in different graphs. Therefore, while this data seem to indicate partial inhibition of the glucose to resorufin reaction by low pH, other factors such as enzyme batch activity or intensity of the microplate reader light source might be responsible for the differences. Upon comparison of the 'without lactose' and 'with lactose' samples at each pH value, we did not observe an effect of lactose on the detected fluorescence at any of the pH conditions tested. However, to maximise precision, we used a separate calibration curve precisely matching the lactose as well as pH conditions in each sample for all glucose detection experiments in this work.

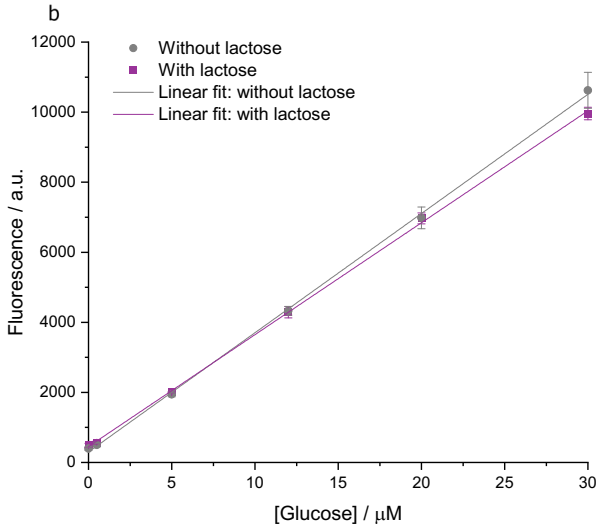
4.3.2 Reaction tests in bulk

Having tested the effect of pH and lactose on the detection of glucose from calibration standards, we then assessed the effect of pH on the generation of glucose from lactose by β-galactosidase. As in Section 4.3.3, we purified the enzyme using a desalting column and used 40 mM lactose as the substrate. In Section 4.3.3, each ~40 nL compartment contained 700 μg mL^{-1} (30 U mL^{-1}) β-galactosidase within an 800 μL external solution, giving an overall β-galactosidase concentration of ~35 ng mL^{-1}(1.5 U mL^{-1}). We therefore used ~35 ng mL^{-1} β-galactosidase for these bulk experiments.

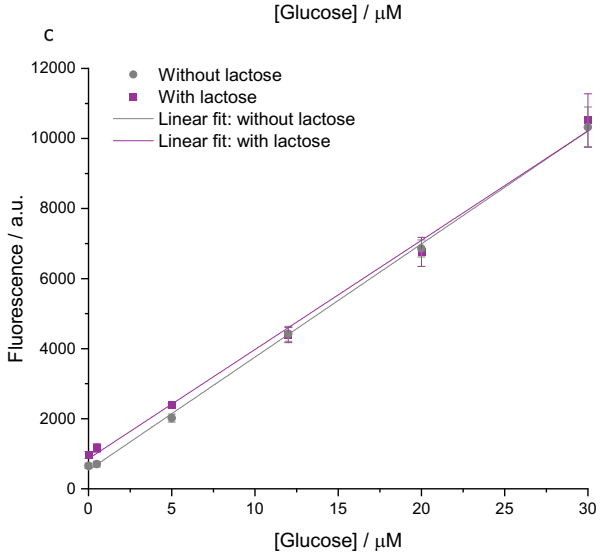
We tested the β-galactosidase with and without lactose and at pH 5.5, 6.5 and 8.0 in bulk solutions. We prepared reaction mixes (n = 3 for each condition) and incubated them at 37 °C. We took samples out of each reaction mix and placed the samples at 4 °C at 0, 1, 2 and 24 h. These time points were selected to match the expected time points of sample collection from the processors at later stages



Equation	y = a + b*x	
Plot	Without lactose	With lactose
Intercept	392.922 ± 50.438	379.506 ± 8.902
Slope	202.372 ± 3.223	200.533 ± 0.569
R-Square (COD)	0.999	1.000



Equation	y = a + b*x	
Plot	Without lactose	With lactose
Intercept	300.60979 ± 62.00064	453.33844 ± 47.86019
Slope	340.29641 ± 3.96209	319.47115 ± 3.05846
R-Square (COD)	0.99946	0.99963



Equation	y = a + b*x	
Plot	Without lactose	With lactose
Intercept	529.063 ± 71.404	858.183 ± 156.631
Slope	323.066 ± 4.563	311.791 ± 10.009
R-Square (COD)	0.999	0.996

Figure 4.8: Detection of glucose standards without or with lactose at various pH conditions. ThermoFisher Amplex Red Glucose/Glucose Oxidase Assay Kit was used to carry out a reaction producing fluorescent resorufin from 0-30 µM glucose standards. Fluorescence values of glucose standards with 0 or 40 mM lactose at **a.** pH = 5.5, **b.** pH = 6.5, **c.** pH = 8.0 (n = 3 for each condition). Error bars = standard deviation.

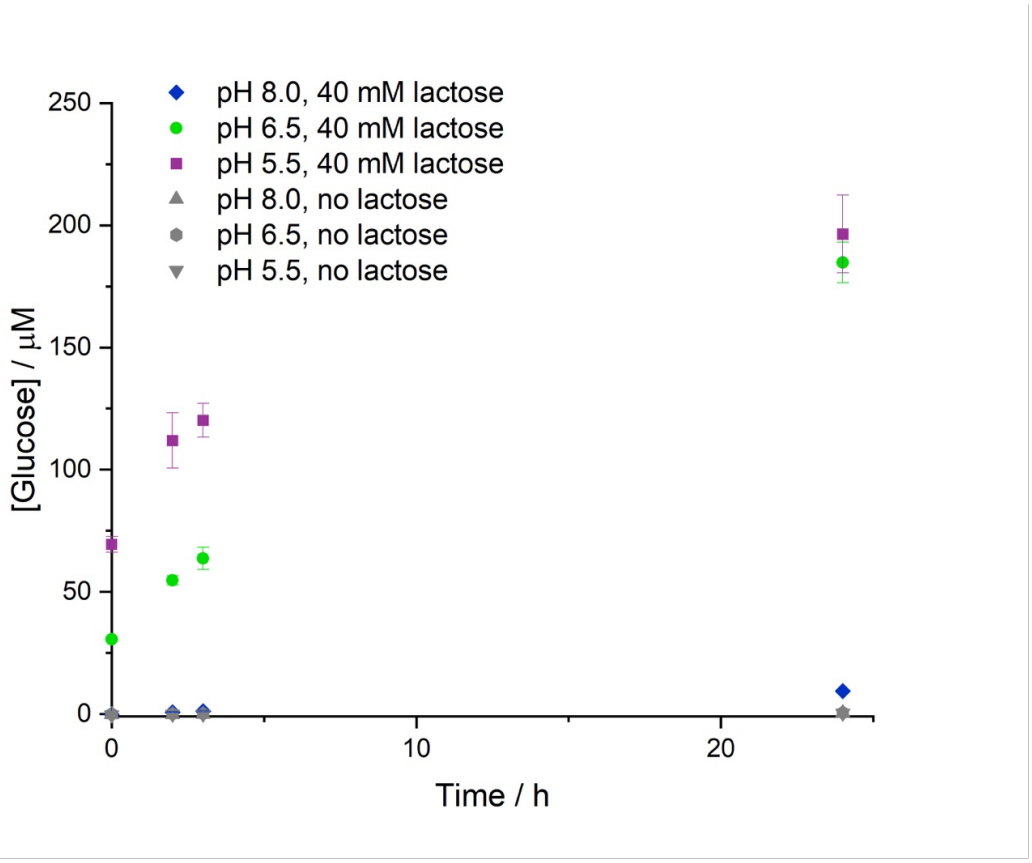


Figure 4.9: Glucose production by β-galactosidase at various pH values without and with lactose Glucose concentration from reaction mixes at pH 5.5, 6.5, 8.0. Error bars = standard deviation.

of this work. We then used the glucose detection kit to measure the concentration of glucose in each sample. We did not detect glucose when the lactose input signal was absent. We observed highest activity of β-galactosidase at pH 5.5, reduced activity at pH 6.5, and very low activity at pH 8.0. We therefore decided to use pH 5.5 for the two-compartment processors containing β-galactosidase.

4.3.3 Encapsulation in two-compartment processors

Having established the β-galactosidase reaction conditions in bulk, we made two-compartment processors containing a signal transmission compartment with 200 µg mL^{-1} αHL monomers, and an enzymatic processing compartment containing β-galactosidase. We initially used the commercially purified β-galactosidase with no further purification and were able to encapsulate maximum

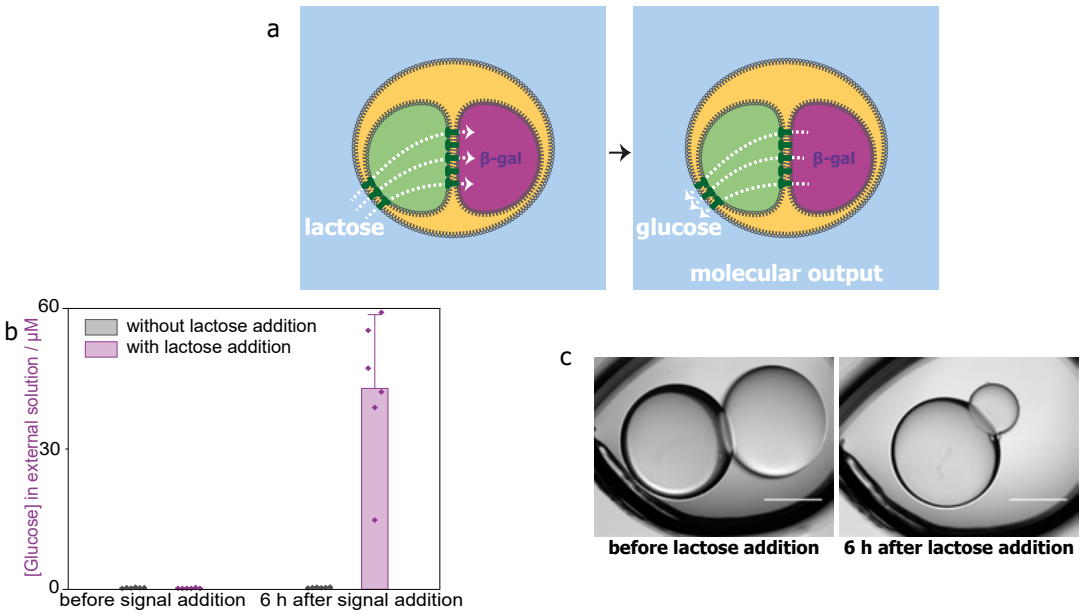


Figure 4.10: Enzymatic hydrolysis in two-compartment processors with a molecular output. **a.** Lactose input signal diffused through the external and internal pores and is hydrolysed by β-galactosidase (β-gal). The product glucose released through the internal and external pores into the external aqueous environment. **b.** Glucose concentration detected in the external aqueous environment before and 6 h after lactose addition and incubation at 37 °C, without (n = 6), and with (n = 6) lactose addition. Error bars = standard deviation. **c.** Bright-field microscopy images of a two-compartment processor containing β-galactosidase before and 6 h after lactose addition and incubation at 37 °C. Scale bars = 300 µm.

~290 µg mL^{-1} (12.5 U mL^{-1}) of this enzyme in the processors. Above this concentration, the β-galactosidase compartment coalesced with the external aqueous environment. We then purified the enzyme using a desalting column and were able to encapsulate 700 µg mL^{-1} (30 U mL^{-1}) in our processors.

Upon addition, lactose input signal should diffuse through the external pores to reach the signal transmission droplet and through the internal pores to reach the enzymatic processing compartment that contains β-galactosidase. After hydrolysis of lactose by β-galactosidase, the product glucose should diffuse through the internal pores to reach the signal transmission compartment and through the external pores to finally be released into the external aqueous environment. Therefore, from signal input to output, molecules must diffuse through 4 bilayers permeabilised by αHL (Fig. 4.10a). The released glucose

would be greatly diluted when mixed with the external aqueous environment. We therefore made enzymatic compartments of 400-470 μm in diameter, ~40 nL in volume, larger than those we had used for processors with a fluorescence output. With an external environment 800 μL in volume, these sizes still resulted in a ~20,000-fold dilution of the glucose upon release. We used signal transmission compartments 500-650 μm in diameter.

After formation of the processors, we added 0 or 40 mM lactose into the external aqueous environment of each processor and incubated the processors at 37 °C for 6 h. Using the glucose detection kit, we measured the glucose concentration in the external aqueous environment (Fig. 4.10b). We did not detect glucose in the external environment of processors without a lactose input (n = 6) and detected an average of 43 μM glucose with the lactose input (n = 6).

We also observed that the β-galactosidase compartments in processors that received a lactose input shrank following incubation (Fig. 4.10c). We attribute this observation to increased osmotic pressure of the external aqueous environment after the lactose was added. The signal transmission compartment was interfaced directly with the external environment through αHL pores. Therefore, it received solutes from the external environment to reach osmotic equilibrium. The β-galactosidase compartment, on the other hand, relied on diffusion of solutes through pores in two different bilayers. Therefore, it reached osmotic equilibrium with the external environment and with the signal transmission compartment by expelling water through its bilayers. The processors remained intact despite these volume changes, demonstrating their structural stability.

We also observed that the β-galactosidase compartments in processors that received a lactose input shrank following incubation (Fig. 4.10c). We attribute this observation to increased osmotic pressure of the external aqueous environment after the lactose was added. The compartments could reach osmotic equilibrium with the external aqueous environment in two ways: through exchange of water through the lipid bilayers (osmosis) or exchange of solutes through the pores. The signal transmission compartment was interfaced directly

with the external environment through αHL pores. Therefore, it received solutes from the external environment to reach osmotic equilibrium. The β-galactosidase compartment, on the other hand, relied on diffusion of solutes through pores in two different bilayers, so its exchange of solutes with the external aqueous environment was slower. Therefore, it reached osmotic equilibrium with the external environment by expelling water through its bilayers and shrinking in size, making its contents more concentrated. The processors remained intact despite these volume changes, demonstrating their structural stability. The system is dynamic, with continuous turnover of lactose to glucose and continuous exchange of solutes and water between the compartments and their environment. The osmotic effects resulting in size change are also expected to be dynamic with the constantly changing conditions of the system.

4.4 Conclusion

In this chapter, we have built two-compartment processors encapsulating an enzymatic process activated by an ionic or molecular external signal to produce a fluorescence or molecular output. We have demonstrated DNA cleavage by EcoRI using an external Mg^{2+} signal to generate a fluorescence output signal. We have shown hydrolysis of lactose input signal by β-galactosidase, generation and release of glucose into the external aqueous environment. In this case, molecular signals diffused through pores in 4 bilayers. In the next chapter, we will combine different processing compartments to generate processors that handle two signals.

5 Three-compartment processors

Contents

5.1 Introduction 71
5.2 Effect of Ca^{2+} and Mg^{2+} input signals on glucose detection . . 72
5.3 Orthogonal processing in three-compartment processors . . . 73
5.4 Simultaneous processing by enzymes in three-compartment processors 75
5.5 Conclusion 77

5.1 Introduction

In previous chapters, we have shown rapid molecular diffusion through αHL pores in lipid bilayers, release and sensing of chemical signals to and from the external environment by two-compartment structures, and enzymatic processing of single external signals by two-compartment structures. We now have all the parts to build a processor that can process two external signals in parallel. In this chapter, we combine various compartments from previous chapters to build two types of three-compartment processors with a signal transmission compartment and two processing compartments. The first type of three-compartment processor contains sensing (Rhod-2) and enzymatic processing (hydrolysis

by β-galactosidase) compartments as processing units. Using this processor, we show orthogonal processing of external Ca^{2+} and lactose signals. The second type of three-compartment processor contains two enzymatic processing compartments: DNA cleavage (EcoRI+DNA) and hydrolysis (β-galactosidase). With this processor, we demonstrate simultaneous enzymatic processing of external Mg^{2+} and lactose even under suboptimal reaction conditions.

5.2 Effect of Ca^{2+} and Mg^{2+} input signals on glucose detection

Our study on the effect of lactose on the detection of glucose by the Thermo Fisher Amplex Red Glucose/Glucose Oxidase Assay kit in Section 4.3.2 was performed without Ca^{2+} or Mg^{2+}. For the three-compartment processors we build in this chapter, we use Ca^{2+} in the form of $CaCl_2$ or Mg^{2+} in the form of $MgCl_2$ as the input signal for one of the processing compartments. In order to ensure that the presence of these input signals would not affect the detection of glucose produced by the β-galactosidase compartment, we performed tests using glucose standards of known concentrations with 0 or 10 mM $CaCl_2$ and 0 or 10 mM $MgCl_2$. These concentrations are the same as the final concentrations of each input signal added into the processors. As each processor would also receive 0 or 40 mM lactose as the other input signal, we also performed tests at these lactose concentrations.

$CaCl_2$, in the absence of lactose, reduced the y-intercept of the calibration curve (shifted the calibration curve down) but did not change the slope significantly (Fig. 5.1a). In the presence of lactose, $CaCl_2$ reduced the y-intercept and increased the slope of the calibration curve (Fig. 5.1b). The addition of $MgCl_2$ and lactose increased both the y-intercept and the slope of the calibration curve (Fig. 5.2). As a result of these effects, for glucose detection from all processors, we compared each sample to a calibration curve made with buffer

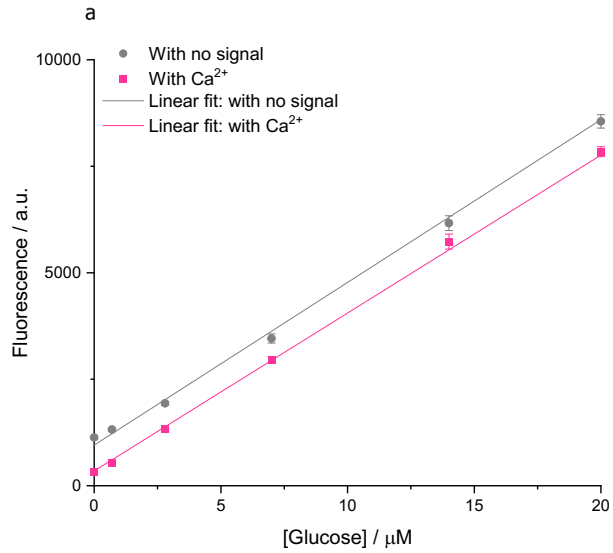
conditions that exactly match the sample's conditions, including $CaCl_2$, $MgCl_2$ and lactose concentrations.

5.3 Orthogonal processing in three-compartment processors

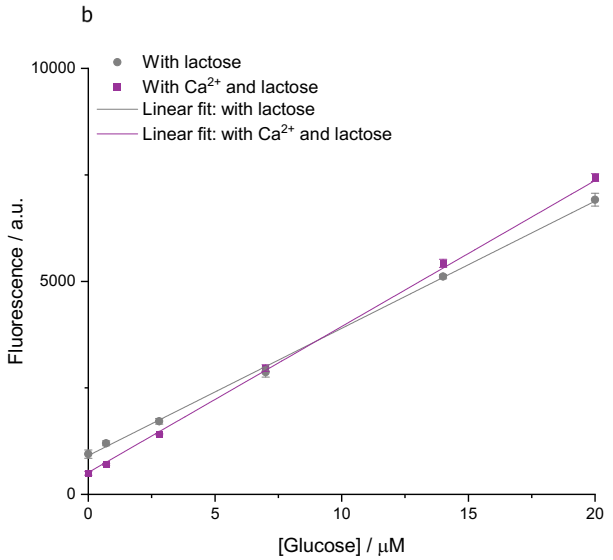
To demonstrate orthogonal processing of two input signals in three-compartment processors, we combined a 500-650 µm diameter signal transmission compartment containing 200 µg mL^{-1} αHL monomers, a 300-350 µm diameter sensing compartment containing 20 µM dextran-conjugated Rhod-2, and a 400-470 µm diameter enzymatic processing compartment containing 700 µg mL^{-1} β-galactosidase (Fig. 5.3a). To maximise the glucose production, we used pH 5.5 which we had previously found to result in high β-galactosidase activity (Fig. 4.9). To each processor, we added one of all four possible input signal combinations: none, only Ca^{2+}, only lactose, and both Ca^{2+} and lactose (Fig. 5.3b) and incubated the processors at 37 °C for 3 h. For these input signals, we used 10 mM Ca^{2+} and 40 mM lactose, the same final concentrations as in the two-compartment processors presented in Chapters 3 and 4.

With no input signals, fluorescence in the sensing compartment decreased and no glucose was detected in the environment (n = 4, Fig. 5.3b). With only the Ca^{2+} input signal, a fluorescence output signal was generated in the sensing compartment but no glucose was detected in the environment (n = 5, Fig. 5.3b). With only the lactose input signal, fluorescence in the sensing compartment decreased and glucose was detected in the environment (n = 4, Fig. 5.3b). With both input signals, both a fluorescence output in the sensing compartment and glucose in the external environment were detected (n = 5, Fig. 5.3b, c). Therefore, the two input signals were processes orthogonally in these processors.

We detected an average of 48 µM glucose in the external solution of these processors using pH 5.5, after the addition of 40 mM lactose and 3 h incubation at 37 °C. These experimental conditions are the same as those in Section 4.3.2

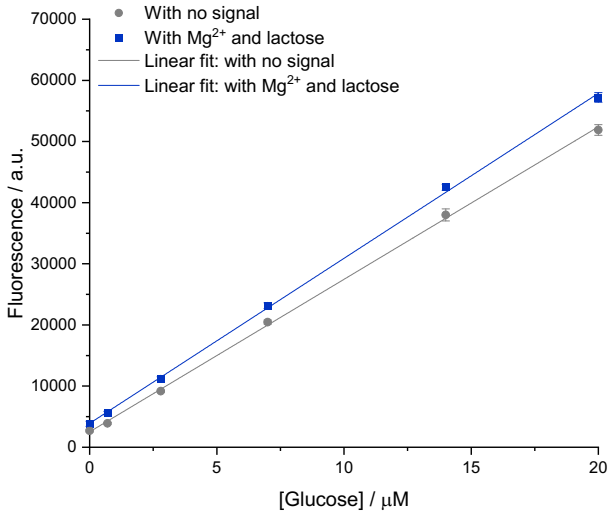


Equation	y = a + b*x	
Plot	With no signal	With Ca^{2+}
Intercept	952.61294 ± 76.83029	346.91566 ± 64.33993
Slope	381.991 ± 4.656	370.673 ± 3.899
R-Square (COD)	0.999	0.999



Equation	y = a + b*x	
Plot	With lactose	With Ca^{2+} and lactose
Intercept	910.833 ± 48.044	513.606 ± 40.313
Slope	298.644 ± 4.604	342.698 ± 2.443
R-Square (COD)	0.999	1.000

Figure 5.1: Effect of $CaCl_2$ on detection of glucose standards. a. Detection of glucose standards without lactose and without or with $CaCl_2$ (n = 3 for each condition). **b.** Detection of glucose standards with lactose and without or with $CaCl_2$ (n = 3 for each condition). Error bars = standard deviation.



Equation	y = a + b*x	
Plot	With no signal	With Mg^{2+} and lactose
Intercept	2522.194 ± 301.823	3905.586 ± 337.208
Slope	2493.846 ± 28.924	2698.573 ± 32.315
R-Square (COD)	0.999	0.999

Figure 5.2: Effect of $MgCl_2$ on detection of glucose standards. a. Detection of glucose standards with lactose and without or with $MgCl_2$ (n = 3 for each condition). Error bars = standard deviation.

where we analysed the glucose production in bulk and detected an average of 120 μM glucose. These results indicate that the diffusion rate of lactose and glucose between the compartments and the external environment was the limiting factor determining the amount of glucose detected in the external environment. The reduction of the generated glucose by only 2.5-fold, especially considering the 4 bilayers involved in the overall signalling process, demonstrates the fast diffusion of these chemical signals through the αHL pores.

5.4 Simultaneous processing by enzymes in three-compartment processors

We also made three-compartment processors to show simultaneous enzymatic processing of two input signals. We combined a signal transmission compartment containing 200 μg mL^{-1} αHL monomers, and two enzymatic processing compartments: one containing 400 U mL^{-1} EcoRI and 400 nM DNA, and the other containing 700 μg mL^{-1} β-galactosidase (Fig. 5.4a). To make both processes work, we used a pH value that would allow both reactions to proceed. We had previously found that EcoRI activity increased (Fig. 4.2) while β-galactosidase

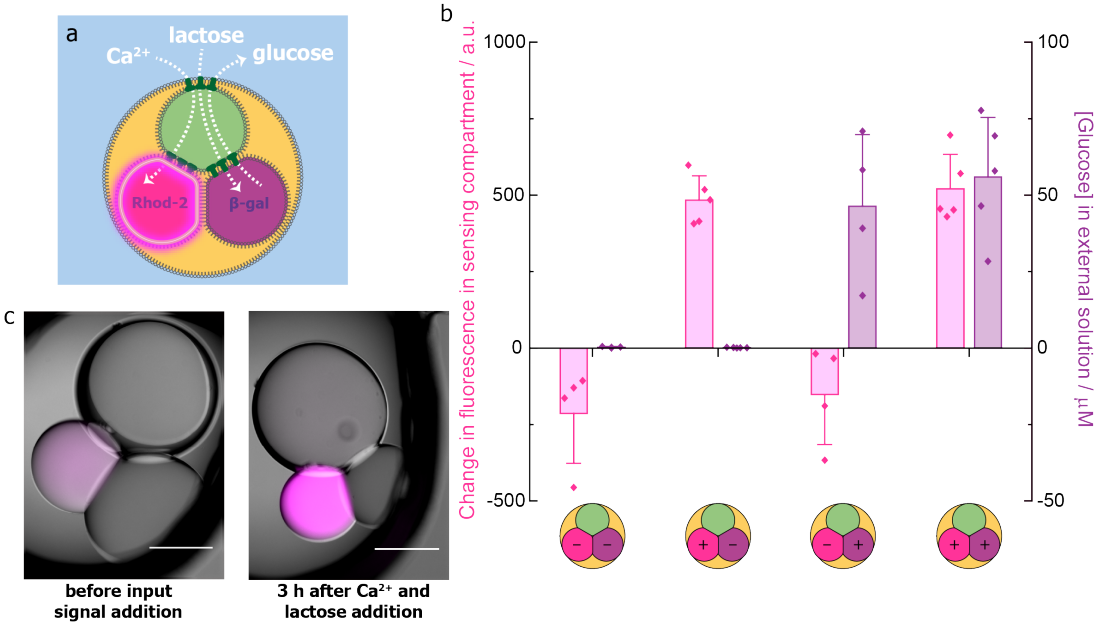


Figure 5.3: Orthogonal processing of two input signals in three-compartment processors. a. Three-compartment processor comprising signal transmission, sensing and enzymatic processing compartments. Ca^{2+} input generates a fluorescence output in the sensing compartment containing Rhod-2, whereas lactose input leads to glucose production by β-galactosidase followed by glucose release into the external environment. **b.** Changes in the mean fluorescence of Rhod-2 compartments and the mean concentration of glucose in the external solution after 3 h incubation at 37 °C for processors with no input signals (n = 4), with an input of only Ca^{2+} (n = 5), only lactose (n = 4), and both Ca^{2+} and lactose (n = 5). Error bars = standard deviation. **c.** Composite bright-field and epifluorescence images of a processor before and after addition of both Ca^{2+} and lactose and and incubation for 3 h at 37 °C. Scale bars = 300 μm.

(Fig. 4.9) activity decreased with increasing pH between 5.5 and 8. The use of the optimal pH for one enzymatic reaction would completely suppress the other. From these activity trends, we selected pH 6.5 as a suitable compromise. Addition of both Mg^{2+} and lactose input signals and incubation for 3 h at 37 °C generated a fluorescence output in the EcoRI compartment (Fig. 5.4b, c) and glucose in the external environment (Fig. 5.4b) simultaneously (n=3), even though the reaction conditions were not ideal for either of the enzymatic processes.

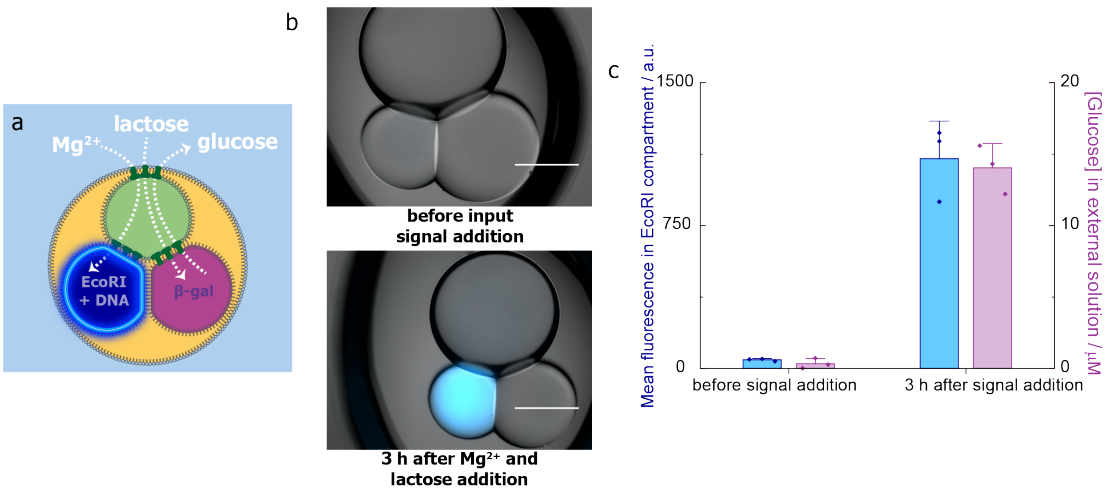


Figure 5.4: Simultaneous enzymatic processing of two input signals in three-compartment processors. a. Three-compartment processor comprising one signal transmission and two enzymatic processing compartments, with EcoRI and β-galactosidase. Mg^{2+} input generates a fluorescence output in the EcoRI+DNA compartment, whereas lactose input leads to glucose production by β-galactosidase, followed by glucose release into the external environment. **b.** Composite bright-field and epifluorescence images of a processor before and after simultaneous addition of Mg^{2+} and lactose input signals and incubation at 37 °C for 3 h. Scale bars = 300 μm. **c.** Mean fluorescence of EcoRI+DNA compartments and the mean concentration of glucose detected in the external solution after 3 h at 37 °C for processors before and after simultaneous input signal addition and processing. Error bars = standard deviation.

5.5 Conclusion

We have built three-compartment processors combining various compartments from previous chapters in a modular fashion. We have demonstrated orthogonal processing of two chemical input signals, Ca^{2+} and lactose, by sensing and enzymatic hydrolysis compartments. We have also built three-compartment processors for simultaneous enzymatic processing of two chemical input signals, Mg^{2+} and lactose, by DNA cleavage and hydrolysis compartments. We have demonstrated that even when two processes are not perfectly compatible, it may still be possible to build functional processors by finding suitable compromise conditions. We have shown a combination of fluorescence and molecular output signals in our processors.

Similar to our observation on two-compartment processors (Fig. 4.10c),

the compartments of the three-compartment processors shrank as a result of increased external osmotic pressure after signal addition and incubation (Fig. 5.3c and 5.4b). Direct comparisons of the shrinking events were not performed as the two-compartment processors in Fig. 4.10c were incubated for 3 h and the three-compartment processors in Fig. 5.3c and 5.4b were incubated for 6 h. In addition, different combinations of compartments and chemical input signals were used for the three systems, which could also affect the overall osmotic effects and resulting size changes. In the three-compartment processors, the β-galactosidase compartment shrank the most, followed by the Rhod-2 or EcoRI+DNA compartment. The signal transmission compartment, interfaced directly with the external environment through αHL pores, was able to reach osmotic equilibrium by taking in solutes rather than expelling water. Therefore, the signal transmission compartment shrank very little, in consistency with the observation in two-compartment processors in Section 4.3.3. Despite these volume changes, the three-compartment processors were structurally stable and generated the expected output signal for each combination of input signals.

This demonstration of a three-compartment droplet processor carrying two different processes is an important step towards multi-functional synthetic biological systems. We would expect the pairs of processes chosen here to work even in the absence of compartmentalisation. However, for incompatible processes, the compartmentalisation demonstrated here will be crucial.

6
Conclusions

We have built lipid-based parallel processors from the bottom up, in a modular fashion.

In Chapter 1, we reviewed the previously generated bottom-up synthetic biological structures that respond to external signals. Compared to single-compartment structures, multi-compartment structures have the potential to encapsulate higher numbers of functions as well as exhibit emergent properties. Multi-compartment structures within an oil environment are limited to electrical, mechanical or light stimuli, whereas those within an aqueous environment can also respond to chemical stimuli. Even though natural cells and tissues process and respond to many external signals, bottom-up synthetic biological structures have been generated to process only one external signal so far. We therefore set out to build a lipid-based, bottom-up synthetic biological structure with two parallel and independent signalling pathways. We designed a multi-compartment modular system where each compartment is optimised for a distinct task such as signal transmission, sensing or enzymatic processing.

As our system relies on diffusion of chemical signals through multiple lipid bilayers, we required high numbers of αHL pores in the bilayers. In Chapter 2, we showed fast diffusion of 2-NBDG through in-situ heptamerised recombinant αHL pores, resulting in equilibration of the molecule across the bilayer within

minutes. We also explored the processes of bilayer formation and molecular diffusion upon contact of two compartments within a lipid-oil environment. A bilayer began forming immediately after two compartments were brought in contact, and expanded its area over several minutes. The rate of this expansion decreased as the bilayer approached its maximum size. Molecular diffusion also began immediately upon bilayer formation, with the formation of the first pores. As more pores formed, the rate of molecular diffusion increased. After the maximum number of pores had formed, molecular diffusion continued at a constant rate, then slowed down when the concentration gradient between the two compartments became small. In this chapter, we also consider various scenarios of chemical signal diffusion: without a membrane, across a membrane, and across a membrane permeabilised by αHL. We estimate the permeability of our DIBs permeabilised by αHL to 2-NBDG. We consider the effect of DIB size and compartment size on the diffusion. We also estimate the number and density of αHL pores in our system and show that over a hundred thousand active pores have inserted into the DIBs.

In Chapter 3, we demonstrated exchange of chemical signals between two-compartment structures and their external aqueous environment. The structure consisted of a signal transmission compartment and a signal release or a sensing compartment. We first showed rapid release of a molecule through two bilayers into the external environment. We then showed intake of an ionic signal through two bilayers and sensing to generate a fluorescence output signal.

After demonstrating exchange of chemical signals with the environment, we coupled chemical exchange to enzymatic processes in Chapter 4. We first built a system requiring one-way diffusion of chemicals: intake of an ionic signal through two bilayers and its enzymatic processing to produce a fluorescence output. In this system, we encapsulated and activated the endonuclease EcoRI with its co-factor Mg^{2+}. Then, we built a system requiring two-way diffusion of chemicals: intake of a molecular signal through two bilayers, its enzymatic processing to produce a molecular output, and release of the molecular output through two

bilayers into the external environment. For this system, we encapsulated the hydrolase β-galactosidase and converted a lactose input signal into a glucose output signal released into the environment.

In Chapter 5, we combined compartments from previous chapters to build three-compartment structures with two processing compartments. Using sensing and β-galactosidase compartments, we demonstrated orthogonal processing of Ca^{2+} and lactose input signals with fluorescence and/or molecular outputs. Using EcoRI and β-galactosidase compartments, we demonstrated simultaneous enzymatic processing of Mg^{2+} and lactose under conditions selected to enable both processes.

In Chapter 7, we provide experimental details.

In this work, we have not only shown modulation of internal processes with external signals, but have also opened the way to modulation of signal transmission. In Chapter 2, we have shown expression of recombinant αHL monomers in *E. coli*, their purification and effective insertion into lipid bilayers. Using the methods we developed, stimuli-responsive αHL mutants may be generated and incorporated into similar systems at high concentrations (~200 μg mL^{-1}) as shown in this work. Previously engineered αHL mutants respond to physical, chemical and biochemical stimuli. For example, αHL-R104C, αHL with a single cysteine mutation at residue 104, loses its pore-forming activity when caged with α-carboxy-2-nitrobenzyl (CNB) as a result of 2-bromo-2-(2-nitrophenyl)acetic acid (BNPA), but regains it upon removal of this protecting group with light[146]. Pores formed by αHL-4H and αHL-H5, two mutants with respectively 4 and 5 residues in the β barrel that are replaced by histidine, are blocked by Zn^{2+}. Addition of a chelator such as ethylenediaminetetraacetic acid (EDTA) removes the Zn^{2+} and opens the pore[113,147]. αHL mutants containing redundant amino acids form pores only upon cleavage by proteases such as endo C, clostripain[148], and matrix metalloproteinase-2 (MMP-2)[149]. Therefore, processors with engineered αHL pores should be achievable. The engineered pores could be used to regulate all signalling processes together, or regulate

signalling only to/from a selected compartment introducing directionality to the signalling processes.

Directional signalling could also be achieved by incorporating additional membrane proteins, such as the mechanosensitive channel of large conductance (MscL)[70,103,150] which gates in response to tensions in the membrane, including those introduced by osmotic shock[151]. Photopolymerisable lipids could also be used to form pores only in selected bilayers[152,153]. Such lipids in the same leaflet of a bilayer cross-link into tightly packed arrangements upon UV exposure. When both leaflets of a bilayer contain these lipids, the tight packing results in structural pores.

Our processors are modular. The contents and size of each compartment are optimized for a distinct task such as signal transmission, sensing or enzymatic processing. Various compartments are combined to generate processors in a modular fashion. The compartments do not require re-optimisation to be combined with other compartments, unless re-optimisation is required for an internal process such as enzymatic activity.

Lipid-bounded aqueous compartments within an external aqueous environment often coalesce with the external environment[112,114]. Balancing the internal and external osmotic pressures during the construction of these structures may produce more stable systems[112,115]. However, these structures, without the ability to tolerate changes in osmotic pressures, are inherently limited to static environments and cannot carry out high turnover reactions which would shift the osmotic conditions and result in coalescence of the structures. Our processors are functionalised with fast signal processing capabilities and involve enzymatic turnover of chemical signals. The compartments incorporate high concentration of enzymes and membrane proteins and do not need to be osmotically balanced with each other or with the external environment. Our processors withstand changing osmotic pressures and are stable at 37 °C as well as at room temperature. During formation, the yield of structures shown in Fig. 5.1 were $\approx$ 90%. For the experiments described in this work, we

monitored the stability of our structures for a maximum of 6 h. However, in other experiments not discussed in this thesis, we monitored the structures for up to two days and observed that they were stable. Depending on their purpose, future structures might need to be stable for shorter or longer time periods. For example, structures aimed at quick, one-off delivery of therapeutics via injection might need to be stable for only minutes, whereas structures aimed at continuously monitoring their environment, such as sensors and biomarker monitors as discussed below, might need to be stable for weeks or even years.

The modularity and robustness of our processors make them suitable for diverse applications. Several processing units could be connected to a large signal transmission compartment to receive and process a high number of input signals in parallel. We envision systems where a central larger signal transmission compartment is surrounded by several processing compartments in a flower arrangement (Fig. 6.1). In this way, each small processing unit can exchange signals with the external environment through the signal transmission compartment. Such a platform could be used to build sensors and micro-reactors. For sensors, the compartments would encapsulate suitable reporters for external signals, such as fluorescent indicators. If a size-selective pore such as αHL is used for signal transmission, the reporters would need to be large molecules that would not diffuse out of the pores. These sensors could be used as parallel processors in medical diagnostics, sensing of bacteria, or water quality analysis. Micro-reactors could be constructed in a similar way, by encapsulating reactions rather than reporters inside the compartments. The reactors could be engineered so that each compartment carries out an independent reaction, collaborates with other compartments to form part of a cascade reaction, or both. Sensing and micro-reaction compartments could also be combined in one system, as we have demonstrated with our three-compartment processors.

To demonstrate the feasibility of structures as in Fig. 6.1, we formed a processor mimic with one large signal transmission compartment and 6 small

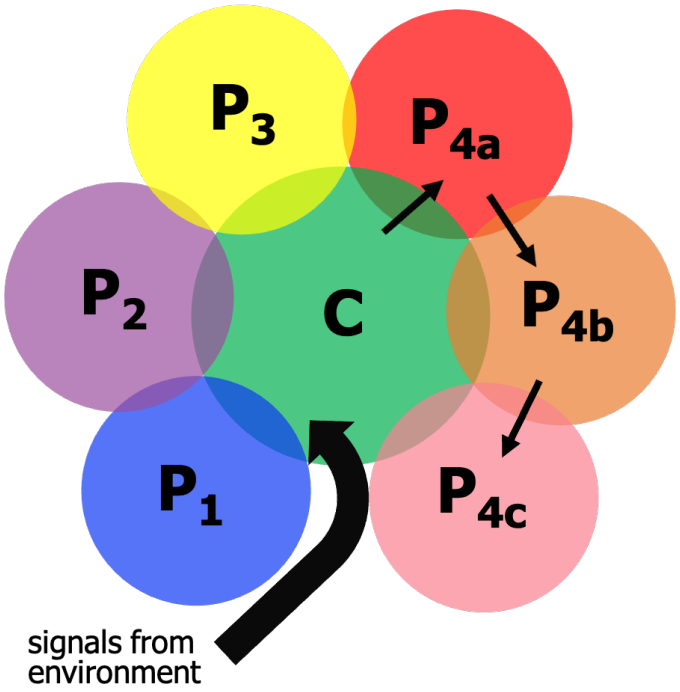


Figure 6.1: A versatile multi-compartment parallel processor with several processing units. A large signal transmission compartment and smaller processing units are expected to self-assemble into a desired flower arrangement with the signal transmission compartment connected to each processing unit. Such structures may serve as sensors or micro-reactors. Compartments can act independently ($P_{1\text{-}3}$) or coordinate with each other for complex functions ($P_{4a\text{-}4c}$).

processing compartments (Fig. 6.2). As we expected, the compartments self-assembled into a flower arrangement with the large compartment in the middle and the small compartments around it and connected to it. With our setup, the self-assembly was complete within 270 s.

Currently, the droplet processors are assembled by manual manipulation, a low-throughput method requiring prior training. Alternative methods such as microfluidics[73,111,154] and 3D-printing[94,99] would enable high throughput production as well as further miniaturisation of the compartments. In its current version, our system relies on a Teflon-coated silver wire to hold the compartments and the surrounding oil within the external aqueous environment. This wire must ideally be eliminated, or at least replaced with a softer and biocompatible material in the next iteration of the system. Similarly, the lipids, oils and pores must be revised to ensure biocompatibility where necessary. The selection of

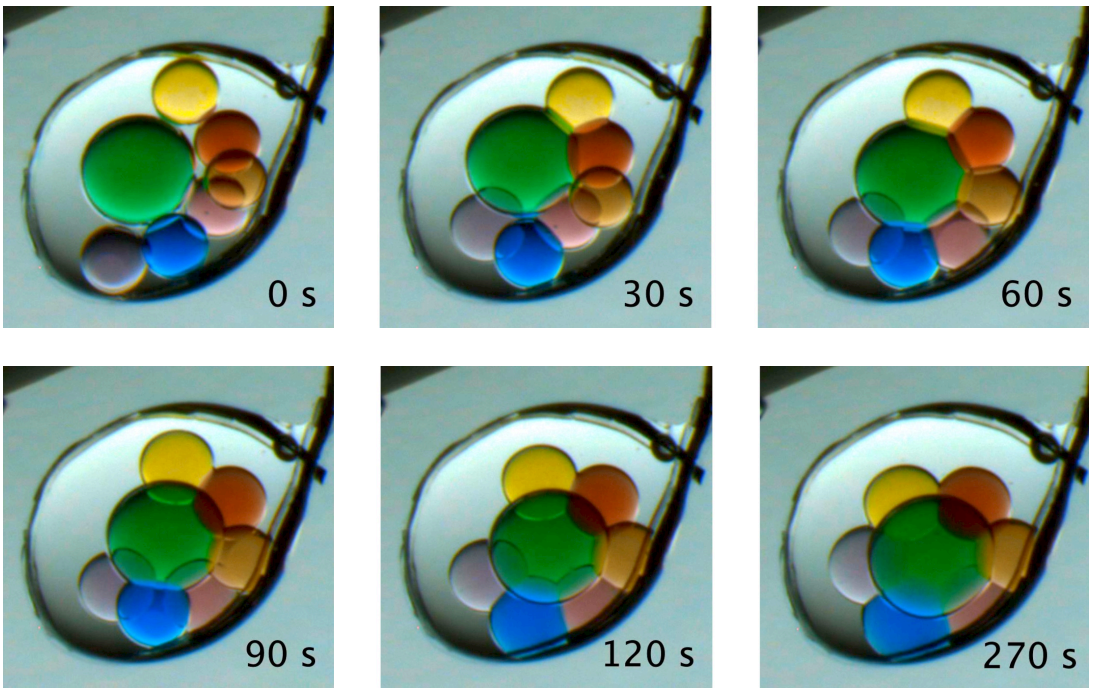


Figure 6.2: Self-assembly of a multi-compartment processor mimic with several processing units. A larger signal transmission compartment mimic in the middle (green dye) connects to each of the 6 processing compartment mimics (various colours). The compartments self-assembled into a flower arrangement within 4.5 min. Wire diameter = 76 µm.

molecular output based on the availability of an assay kit, as done in this work, limits the processes that could be encapsulated and monitored in the droplet processors. Alternative analytical methods, such as mass spectrometry, should be used to diversify the processes that can be tested.

Once the multi-compartment processors are revised for biocompatibility and further miniaturised, they might also be employed to monitor multiple biomarkers within the body for smart drug delivery. Internal processes could be activated with biomarkers and lead to in-situ production and release of drugs, or release of pre-loaded drugs. The drug delivery processors might also be engineered to process input signals in more complex ways. For example, they could generate drugs at doses that depend on the biomarker concentration, the timing of biomarker detection, or the concentration ratios of multiple biomarkers.

In the future, the processors could be incorporated into synthetic tissues or

hybrid systems and handle signals between synthetic and living tissues. They not only could transmit signals but also could convert or amplify them where needed. As we have demonstrated, the processors can readily exchange signals with the environment. Therefore, they do not need to be attached to the synthetic or living tissues, and can pick up and process signals from the environment for long-distance communication. For example, processors could trigger cell-free expression in response to external signals. This could drive differentiation of localised cell-like compartments within synthetic tissues. Processors on synthetic tissues could also drive movement towards specific stimuli, such as sources of reagents required for internal processes, or biomarkers indicating the location of a damaged tissue nearby. These processors could also prompt localised release of cargo from synthetic tissues to provide drugs to or regulate gene expression in interfacing tissues or organisms. By enabling communication between synthetic and living tissues, the processors could coordinate them to act as functional hybrid systems.

The work presented in this thesis has been published in a peer-reviewed journal article[155].

7 Experimental Details

Contents

7.1 Materials and Instruments 87
7.2 Compositions of solutions 90
7.3 αHL expression and purification 91
7.4 αHL buffer exchange attempts using centrifugal filtration devices 93
7.5 Formation of DIBs 93
7.6 Formation of processors and processor mimics 93
7.7 Fluorescence output detection and analysis 94
7.8 Glucose detection and analysis 95
7.9 Contact angle measurements 95
7.10 EcoRI assays 96
7.11 Code for Image Analyses 96
7.11.1 Compartment Detection 96
7.11.2 Compartment Measurement 97
7.11.3 Contact Angle Measurement and Fluorescence Analysis 98

7.1 Materials and Instruments

Table 7.1: List of materials and sources.

Material	Source
2-NBDG	Invitrogen
96-well plates	Corning
β-galactosidase from *A. oryzae*	Sigma-Aldrich

Continued on next page

Table 7.1 – *Continued from previous page*

Material	Source
Agar	Sigma-Aldrich
Amicon centrifugal filters	Merck
Amplex Red Glucose/Glucose Oxidase Assay Kit	Invitrogen
BAPTA tetrapotassium salt	Invitrogen
Benzonase	Sigma-Aldrich
BSA	Sigma-Aldrich
Carbenicillin disodium	Sigma-Aldrich
$CaCl_2$ dihydrate	Sigma Aldrich
Centrifuge tubes	Thermo Fisher Scientific
Chloramphenicol	Sigma-Aldrich
Cy5 & BHQ-3 labelled DNA substrate	ATDBio
D-lactose	Sigma-Aldrich
DNA ladder 100 or 1000 bp	New England Biolabs
DPhPC	Avanti Polar Lipids
E. coli BL21(DE3)pLysS cells	Agilent
EcoRI-HF	New England Biolabs
EDTA	Sigma-Aldrich
Glucose	Sigma-Aldrich
HCl, 6 M	Honeywell Fluka
Hexadecane	Sigma-Aldrich
Imidazole	Sigma-Aldrich
Instant Blue	Expedion
IPTG	Fluorochem
Laemmli buffer	Bio-Rad
LB	Sigma-Aldrich
MES	Sigma-Aldrich
$MgCl_2$ hexahydrate	Sigma-Aldrich
Microtubes	Eppendorf
Millex-GP 0.22 µm polyethersulfone syringe Filters	Millipore
Mini-PROTEAN TGX Precast Gels	Bio-Rad
NaCl	Sigma-Aldrich
NaOH, 8 M	Honeywell Fluka
Ni-NTA resin	HisPur
PD-10 Desalting Columns	GE Healthcare
POPC	Avanti Polar Lipids
Protein LoBind tubes	Eppendorf
Protein standards 10-250 kD	Bio-Rad
Rhod-2, MW ~11,000	AAT Bioquest
Silicone oil AR20	Wacker
Superdex 75 100/300 GL	GE Healthcare
Teflon-capped glass vials	Supelco
Teflon-coated silver wire,	A-M Systems

Continued on next page

Table 7.1 – *Continued from previous page*

Material	Source
diameter 0.003" bare, 0.0055" coated	
TGS buffer	Bio-Rad
Tris-HCl	Sigma-Aldrich
Triton-X100	Sigma-Aldrich

Table 7.2: List of instruments and manufacturers.

Instrument	Manufacturer	Address
DMi8 epifluorescence microscope	Leica	Wetzlar, Germany
Infinite M1000 Pro microplate reader	Tecan	Zurich, Switzerland
SZX10 upright stereo microscope	Olympus	Tokyo, Japan
NanoDrop 1000 for αHL	Thermo Fisher Scientific	Waltham, MA, USA
NanoDrop One for β-galactosidase	Thermo Fisher Scientific	Waltham, MA, USA
Nanophotometer N60 for DNA	Implen	Munich, Germany
AKTA FPLC Chromatographic System	GE Healthcare	Chicago, IL USA
Zerostat 3 antistatic gun	Milty	Genilac, France
Model 1545 Incubator	VWR	Radnor, PA, USA
Innova 44 Incubator Shaker	New Brunswick Scientific (Eppendorf)	Hamburg, Germany
Centrifuge 5810 R	Eppendorf	Hamburg Germany

Continued on next page

Table 7.2 – *Continued from previous page*

Instrument	Manufacturer	Address
MiniSpin Centrifuge	Eppendorf	Hamburg Germany
Vibra-Cell ultrasonic liquid processor	Sonics	Newtown, CT, USA
Ultrasonic cleaner 2800	Branson (Emerson)	Brookfield, CT, USA
Speed Vac Concentrator	Savant (Thermo Fisher Scientific)	Waltham, MA, USA

7.2 Compositions of solutions

We stored lipids as powder at -80 °C. We filtered hexadecane and silicone oil AR20 under vacuum using 0.22 µm polyethersulfone filters. To prepare lipid films, we dissolved the lipids in chloroform inside glass vials and evaporated the chloroform under a stream of nitrogen gas at low pressure, while rotating the vial. We desiccated the lipids under vacuum for at least 16 h, then stored them under argon gas at -80 °C. On the way of use, we dissolved a final concentration of 2 mM (5 mM for Fig. 2.10) lipid in 65:35 v:v silicone oil:hexadecane by sonication for 45 min (Ultrasonic cleaner 2800, Branson).

For each experiment, we dissolved β-galactosidase from powder and purified the solution using a PD-10 desalting column in the buffer required for the specific experiment. We verified the concentration of β-galactosidase in each fraction using a Nanodrop One. We thawed an individual aliquot of αHL on ice and diluted it with 10 mM Tris-HCl pH 8.0, 200 mM NaCl to give the desired concentration. To minimise diffusion of the fluorescent product in processors involving the EcoRI reaction, we diluted the αHL to a concentration at which the equilibration of 2-NBDG across a bilayer as in Fig. 2.8 took 20-30 min. For all

other processors, we used 200 μg mL^{-1} αHL, which gave 2-NBDG equilibration time across a bilayer as in Fig. 2.8 of ~6 min.

Signal release compartments contained 1 mM 2-NBDG. Sensing compartments contained 20 μM Rhod-2 and 2 μM BAPTA. β-galactosidase compartments contained 700 μg mL^{-1} β-galactosidase and, when they were coupled with a Rhod-2 compartment, 2 μM BAPTA. EcoRI compartments contained 400 U mL^{-1} EcoRI, 400 nM DNA substrate labelled with Cy5 and BHQ-3, and 100 μg mL^{-1} BSA. Except the signal transmission compartment, all compartments and external aqueous environments contained 50 mM MES and 100 mM NaCl as the buffer. The pH was 6.5 for experiments involving EcoRI or 2-NBDG, and 5.5 for all other experiments. For experiments involving Rhod-2, all processing compartments and external environments contained 2 μM BAPTA. We prepared each input signal in the same buffer composition as the external environment where they were added. We added input signals to give final concentrations of 0 or 10 mM $CaCl_2$ (for Rhod-2), 0 or 10 mM $MgCl_2$ (for EcoRI), and 0 or 40 mM D-lactose (for β-galactosidase).

7.3 αHL expression and purification

We transformed *E. coli* BL21(DE3)pLysS cells with αHL-D8H6 plasmid on ice for 30 min, without a heat shock. We spread the transformed cells on LB-agar plates containing 25 g L^{-1} lysogeny broth (LB) and 15 g L^{-1} agar, 50 μg mL^{-1} carbenicillin disodium and 34 μg mL^{-1} chloramphenicol. We incubated the plates for 16 h at 37 °C (Model 1545 Incubator, VWR). We picked single colonies, inoculated each colony into 50 mL centrifuge tubes containing 15 g L^{-1} LB with the antibiotics and incubated the cultures at 37 °C with shaking at 250 rpm until the OD reached ~0.7 (Innova 44 Incubator Shaker, New Brunswick). We then induced the cultures in the same tubes, with a final concentration of 1 mM isopropyl β-d-1-thiogalactopyranoside (IPTG) and incubated them for 16 h at 18 °C with shaking at 250 rpm. We centrifuged the cultures at 3800 rpm at 4

°C for 20 min to obtain cell pellets (Centrifuge 5810 R, Eppendorf) and lysed the cells using 50 mM Tris-HCl, pH 8.0, 0.5 M NaCl, 10 mM imidazole, 0.1% Triton X-100 and ice-cold $MgCl_2$ at a final concentration of 5 mM, hen egg white lysozyme at a final concentration of 1 mg mL^{-1} and 250 units benzonase.

We sonicated the lysate on ice using an ultrasonic probe (Vibra-Cell ultrasonic liquid processor, Sonics) with 30 s pulses and 30 s intervals for 3 min. We then centrifuged the lysate 29 000 g for 45 min at 4 °C to separate the supernatant and cell debris (Centrifuge 5810 R, Eppendorf). We loaded a 20 mL column with 2 mL Ni-NTA resin, added the supernatant, and rotated the loaded column on a rotator disk for 1 h at 4 °C. We then washed the column twice with ice-cold 15 mL of 50 mM Tris-HCl pH 8.0, 0.5 M NaCl, 10 mM imidazole and 0.1% Triton X-100. We collected the eluted proteins in 1.5 mL microtubes as 5 batches of 1 mL using 50 mM Tris-HCl pH 8.0, 0.5 M NaCl, 250 mM imidazole and 0.1% Triton X-100. Using SDS-PAGE gel electrophoresis, we confirmed that the His-tag purification was successful. We also observed that the eluted batches contained both monomers and heptamers of αHL (Fig. 2.1).

We stored the His-tag purified protein batches at -80 °C until FPLC purification. We performed size exclusion chromatography to separate the monomers and heptamers and exchange the buffer. We equilibrated a Superdex 75 100/300 GL gel filtration column with 10 mM Tris-HCl pH 8.0, 200 mM NaCl. We loaded 500 µL of an elution with high protein concentration, ran the system with this buffer at a flow rate of 0.5 mL min^{-1} and eluted each fraction at 0.5 mL. We monitored monomeric and heptameric αHL by ultraviolet absorption at 215, 254 and 280 nm (Fig. 2.6). We also visualised the purified αHL fractions with the highest concentrations using SDS-PAGE gel electrophoresis (Fig. 2.7) and measured their concentrations using a Nanodrop. We aliquoted the fractions with highest concentrations (200-400 µg mL^{-1}) as 5-10 µL in 0.5 mL Protein LoBind tubes and stored them at -80 °C.

7.4 αHL buffer exchange attempts using centrifugal filtration devices

We loaded the centrifugal filtration device within a microcentrifuge tube provided by the manufacturer with 50 µL of αHL obtained after the Ni-NTA purification and 450 µL of the new buffer (10 mM Tris-HCl, pH 8, 200 mM NaCl) with which to replace the Ni-NTA purification buffer. We centrifuged the device at 4 °C for 10 min at 14000 g (MiniSpin centrifuge, Eppendorf). We discarded the filtrate or stored it for vacuum concentration (Speed Vac Concentrator, Savant) and used a clean microcentrifuge tube for the next wash. We repeated this washing process for a number of times as indicated in Chapter 2 for individual cases, each time using 450 µL of the new buffer. We then inverted the filtration device in a clean microcentrifuge tube and centrifuged it for 2 min at 1000 g to collect the final product.

7.5 Formation of DIBs

Under an upright stereo microscope (SZX10, Olympus), we filled poly(methyl methacrylate) (PMMA) wells with lipid-oil mix. Using a Gilson P2 pipette, we made aqueous compartments of desired contents and sizes inside the wells. A monolayer of lipids formed around each compartment. To form DIBs, we brought the compartments together by tilting the wells or using a plastic tip.

7.6 Formation of processors and processor mimics

We made the processor chambers as previously described[112] SZX10 upright stereo microscope, Olympus. We glued the bottom section of a plastic cuvette to a glass microscope slide, then glued a ~3 cm long Teflon-coated silver wire to the edge of the cuvette and dried overnight. We then bent the wire to form a loop. Before and after each use, we washed the chambers with water and ethanol and air-dried them.

To form the processors, we added external aqueous solution into each chamber and placed a ~1.5 µL of lipid-containing oil drop onto the wire loop in each chamber. We we neutralised static charges on the chambers using an anti-static gun (Zerostat 3, Milty) and incubated them for at least 5 min to allow the formation of a lipid monolayer between the oil drop and the external aqueous environment.

We formed the aqueous compartments of desired contents and sizes using a Gilson P2 pipette, inside PMMA wells filled with lipid-containing oil. We formed 2-NBDG, β-galactosidase and Rhod-2 compartments first and incubated them in the PMMA wells for at least 10 min. We formed the EcoRI and αHL compartments later and did not incubate them. To make each processor, we aspirated all compartments into the pipette tip and simultaneously transferred them into the oil drop.

We imaged each processor using brightfield and/or epifluorescence microscopy before and after signal addition and processing. For processors with a molecular output, we pipetted sample solution out of each chamber before signal addition for analysis. After signal addition, all processors had a total external solution of 800 µL. We incubated the processors for the specified time and at 37 °C where indicated. We then pipetted sample solutions out of each chamber again for analysis.

7.7 Fluorescence output detection and analysis

We detected fluorescence outputs using a Leica DMi8 epifluorescence microscope. We used the filter cube GFP (ex: 450–490 nm, em: 500–550 nm) for 2-NBDG), DSRED (ex: 540–552, em: 567–643 nm) for Rhod-2, and DAPI (ex: 325-375, em: 435–485) for EcoRI+DNA.

We detected and analysed the fluorescent compartments on Fiji/ImageJ using custom scripts (Sections 7.11.1 and 7.11.2) followed by manual verification. Rarely, artefacts were caused by an air bubble or the silver wire, and required

manual correction. Using the script, we applied a Gaussian blur with a standard deviation of 4 and the Moments automatic thresholding to each fluorescence image. We then called the built-in particle analysis algorithm of Fiji/ImageJ to detect and save a region of interest (ROI) for each fluorescent compartment with area = 20000-70000 μm^2 and circularity = 0.15-1.00. We applied each resulting ROI to the corresponding original epifluorescence image and measured the average fluorescence within the ROI.

To measure the diffusion of fluorescent reaction product out of EcoRI+DNA compartments, we defined an additional ROI by drawing a line across of each signal transmission compartment. We then applied each ROI to its corresponding fluorescence image to obtain fluorescence values across the diameter of each signal transmission compartment.

7.8 Glucose detection and analysis

For detection of glucose, we used the Thermo Fisher Amplex Red Glucose/Glucose Oxidase Assay Kit. We prepared glucose standards to make a calibration curve with each of the buffer conditions used and loaded them in 3 wells of a 96-well plate at 50 µL each. We added 50 µL of each sample in the same plate as each set of calibration standards. We then mixed each well with 50 µL of reaction mix containing glucose oxidase, horseradish peroxidase and amplex red. We measured fluorescence from all wells at 30 min, and performed linear regression to determine concentrations of glucose in the samples. If a sample had a glucose concentration higher than 30 µM, we diluted it and re-measured its fluorescence within the linear range of the assay.

7.9 Contact angle measurements

We measured the contact angles between two compartments forming a DIB as previously described[99]. We employed the formula relating the radius of

each compartment (R_1 and R_2) and the centre-to-centre distance (L) to the contact angle (θ):

$$2\theta = \cos^{-1}\left(\frac{L^2 - R_1^2 - R_2^2}{2R_1R_2}\right) \tag{7.1}$$

We used a custom-written script in MATLAB (Section 7.11.3) on the bright-field microscopy images to estimate R_1 and R_2 by circle fitting around the compartments and L from the distance between the fitted circles. We also used the script to measure the average fluorescence value each compartment area.

7.10 EcoRI assays

We prepared 110 µL reaction mixes containing 364 U mL^{-1} EcoRI and 354 nM DNA substrate labelled with Cy5 and BHQ-3 in 45 mM buffer, 91 mM NaCl and 91 µg mL^{-1} BSA inside wells of a 96-well plate. The 45 mM buffer was MES pH 5.5, MES pH 6.5 or Tris pH 8.0. We added 0 or 10 mM $MgCl_2$ in each well, covered the well plate and placed it inside a Tecan Infinite M1000 Pro microplate reader pre-heated to 37 °C. We took fluorescence measurements from the bottom of each well every 5 min with ex = 645-655 nm and em = 665-675 nm, with automatic shaking before measurements at each time point.

7.11 Code for Image Analyses

7.11.1 Compartment Detection

```
% Detecting fluorescent compartments of desired size and circularity
% Author: Idil Cazimoglu
% Date: 25.05.2020

finish=nImages;

for (i=0;i<finish;i++) {
```

```
        selectImage(i+1);
        title=getTitle();

        if (indexOf(title, "C=1") >= 0) {
                run("Duplicate...", " ");
                run("Gaussian Blur...", "sigma=4");
                setAutoThreshold("Moments dark");
                run("Threshold...");
                setOption("BlackBackground", false);
                run("Convert to Mask");
                run("Close");
                run("Analyze Particles...", "size=20000-70000
                circularity=0.15-1.00
                display exclude include add");
        }
}
```

7.11.2 Compartment Measurement

```
% Measuring values of interest from the compartments analysed by the
Compartment Detection script
% Author: Idil Cazimoglu
% Date: 25.05.2020

ROIfinish=nImages*2/3;

for (i=0;i<ROIfinish;i++) {
        selectImage(i+1);
        title=getTitle();
```

```
        if (indexOf(title, "C=0") >= 0) {
                roiManager("Select", (i+1)/2);
        }

        //select C=number for the appropriate channel
        else if (indexOf(title, "C=1") >= 0) {
        roiManager("Select", i/2);
        run("Measure");
        }
}
```

7.11.3 Contact Angle Measurement and Fluorescence Analysis

```
% Measuring dynamic contact angle and molecular diffusion in DIBs
% Author: Dr Alessandro Alcinesio
% Date: 14 Jan 2021

inFileBW = 'pathname';
inFileC = 'pathname';
verbose = true;

tiff_info = imfinfo(inFileBW);
stackBW = imread(inFileBW, 1);
stackC = imread(inFileC, 1);

for ii = 2 : size(tiff_info, 1)
        temp_tiffBW = imread(inFileBW, ii);
        stackBW = cat(3 , stackBW, temp_tiffBW);
```

```
        temp_tiffC = imread(inFileC, ii);
        stackC = cat(3 , stackC, temp_tiffC);
end

img = stackBW(:,:,1);

contactAngleTimelapse = zeros(size(tiff_info, 1),1);
fluo1 = zeros(size(tiff_info, 1),1);
fluo2 = zeros(size(tiff_info, 1),1);

for ii = 1 : size(tiff_info, 1)

                img = stackBW(:,:,ii);
                imgC = stackC(:,:,ii);
                [centres,radii,metric] = imfindcircles(max(img(:))
                -img,[130,300],
                'Sensitivity',0.97);

        if size(centres,1) == 2
                L = pdist(centres);
                R1 = radii(1);
                R2 = radii(2);

                contactAngle = acos(((L*L) - (R1*R1) - (R2*R2))/(2*R1*R1));

        elseif size(centres,1) > 2
                warning('Number of droplets detected is greater than 2.
                Using closest pair...');

                dists = pdist2(centres,centres);
```

```
                for i = 1:size(dists,1)
                        dists(i,i) = NaN;
                end

        [L,minInd] = min(dists(:));

        [circle1,circle2] = ind2sub(size(dists),minInd);
        R1 = radii(circle1);
        R2 = radii(circle2);

        contactAngle = acos(((L*L)
         - (R1*R1) - (R2*R2))/(2*R1*R1));

elseif size(centres,1) < 2
        warning('Number of droplets detected is less than 2.
        Skipping...');

        contactAngle = NaN;
end

contactAngleDeg = rad2deg(contactAngle)/2;

contactAngleTimelapse(ii) = contactAngleDeg;
imshow(img,[]);
viscircles(centres,radii,'EdgeColor','r')

CR = [centres(1,:), R1; centres(2,:), R2];
CRSorted = sortrows(CR);
roi1 = images.roi.Circle(gca,'Center',CRSorted(1,[1,2]),
```

```
        'Radius',CRSorted(1,3));
        mask1 = createMask(roi1);

        roi2 = images.roi.Circle(gca,'Center',CRSorted(2,[1,2]),
        'Radius',CRSorted(2,3));
        mask2 = createMask(roi2);

        fluo1(ii) = mean(imgC(mask1));
        fluo2(ii) = mean(imgC(mask2));

        if ii == 12
                C12 = [mean(centres(:,1)), mean(centres(:,2))];
        end

        if ii == 13
                C13 = [mean(centres(:,1)), mean(centres(:,2))];
        end
end

roiBG1 = images.roi.Circle(gca,'Center',C12,'Radius',R2);
roiBG2 = images.roi.Circle(gca,'Center',C13,'Radius',R2);

imgBG1 = stackC(:,:,1);
imgBG2 = stackC(:,:,56);

maskBG1 = createMask(roiBG1);
maskBG2 = createMask(roiBG2);

BG1 = mean(imgBG2(maskBG1));
BG2 = mean(imgBG1(maskBG2));
```

```
if verbose
        imshow(img,[]);
        viscircles(centres,radii,'EdgeColor','r');
end
```

References

1. Su, S. & Kang, P. M. Systemic Review of Biodegradable Nanomaterials in Nanomedicine. *Nanomaterials* **10,** 656 (2020).
2. Monteiro, N., Martins, A., Reis, R. L. & Neves, N. M. Liposomes in tissue engineering and regenerative medicine. *J. R. Soc. Interface* **11** (2014).
3. Sercombe, L. *et al.* Advances and challenges of liposome assisted drug delivery. *Front. Pharmacol.* **6,** 286 (2015).
4. Patra, J. K. *et al.* Nano based drug delivery systems: Recent developments and future prospects. *J. Nanobiotechnology* **16,** 71 (2018).
5. VegaVasquez, P., Mosier, N. S. & Irudayaraj, J. Nanoscale drug delivery systems: from medicine to agriculture. *Front. Biomed. Biotechnol.* **8,** 79 (2020).
6. Li, J. & Mooney, D. J. Designing hydrogels for controlled drug delivery. *Nature Rev. Mater.* **1,** 1–17 (2016).
7. Sharma, A. K. *et al.* Emerging era of "somes": polymersomes as versatile drug delivery carrier for cancer diagnostics and therapy. *Drug. Deliv. Transl. Res.* **10,** 1171–1190 (2020).
8. Johnson, N. R. & Wang, Y. Coacervate delivery systems for proteins and small molecule drugs. *Expert Opin. Drug Deliv.* **11,** 1829–1832 (2014).
9. Bulbake, U., Doppalapudi, S., Kommineni, N. & Khan, W. Liposomal Formulations in Clinical Use: An Updated Review. *Pharmaceutics* **9,** 12 (2017).
10. Muller, W. E. G. *et al.* Nanoparticle-directed and ionically forced polyphosphate coacervation: a versatile and reversible core–shell system for drug delivery. *Sci. Rep.* **10,** 1–16 (2020).
11. Lee, Y. & Thompson, D. Stimuli-responsive liposomes for drug delivery. *Wiley Interdiscip. Rev. Nanomed. Nanobiotechnol.* **9,** e1450 (2017).
12. Villar, G., Heron, A. J. & Bayley, H. Formation of droplet networks that function in aqueous environments. *Nat. Nanotechnol.* **6.** 10.1038/nnano.2011.183, 803–808 (2011).
13. Li, M., Huang, X., Tang, T. Y. & Mann, S. Synthetic cellularity based on non-lipid micro-compartments and protocell models. *Curr. Opin. Chem. Biol.* **22,** 1–11 (2014).
14. Rideau, E., Dimova, R., Schwille, P., Wurm, F. R. & Landfester, K. Liposomes and polymersomes: a comparative review towards cell mimicking. *Chem. Soc. Rev.* **47,** 8572–8610 (2018).
15. Wertheimer, A. I., Santella, T. M., Finestone, A. J. & Levy, R. A. Drug delivery systems improve pharmaceutical profile and facilitate medication adherence. *Adv Ther.* **22,** 559–577 (2005).

16. Mufamadi, M. S. *et al.* A Review on Composite Liposomal Technologies for Specialized Drug Delivery. *J. Drug Deliv.* **2011,** 1–19 (2011).

17. Zylberberg, C. & Matosevic, S. Pharmaceutical liposomal drug delivery: a review of new delivery systems and a look at the regulatory landscape. *Drug Deliv.* **23,** 3319–3329 (2016).

18. Laohakunakorn, N. *et al.* Bottom-Up Construction of Complex Biomolecular Systems With Cell-Free Synthetic Biology. *Front. Bioeng. Biotechnol.* **8,** 213 (2020).

19. Gopfrich, K., Platzman, I. & Spatz, J. P. Mastering Complexity: Towards Bottom-up Construction of Multifunctional Eukaryotic Synthetic Cells. *Trends Biotechnol.* **36,** 938–951 (2018).

20. Deforest, C. A., Polizzotti, B. D. & Anseth, K. S. Sequential click reactions for synthesizing and patterning three-dimensional cell microenvironments. *Nat. Mater.* **8,** 659–664 (2009).

21. Abbas, M., Wojciech P. Lipinski, J. W. & Spruijt, E. Peptide-based coacervates as biomimetic protocells. *Chem. Soc. Rev.* **50,** 3690 (2021).

22. Huang, X. *et al.* Interfacial assembly of protein-polymer nano-conjugates into stimulus-responsive biomimetic protocells. *Nat. Commun.* **4,** 1–9 (2013).

23. Cruise, G. M., Scharp, D. S. & Hubbell, J. A. Characterization of permeability and network structure of interfacially photopolymerized poly(ethylene glycol) diacrylate hydrogels. *Biomaterials* **19,** 1287–1294 (1998).

24. Mason, M. N., Metters, A. T., Bowman, C. N. & Anseth, K. S. Predicting controlled-release behavior of degradable PLA-b-PEG-b-PLA hydrogels. *Macromolecules* **34,** 4630–4635 (2001).

25. Wallace, M., Adams, D. J. & Iggo, J. A. Analysis of the mesh size in a supramolecular hydrogel by PFG-NMR spectroscopy. *Soft Matter* **9,** 5483–5491 (2013).

26. Rehmann, M. S. *et al.* Tuning and Predicting Mesh Size and Protein Release from Step Growth Hydrogels. *Biomacromolecules* **18,** 3131–3142 (2017).

27. Lin, C. C. & Metters, A. T. Hydrogels in controlled release formulations: Network design and mathematical modeling. *Adv. Drug Deliv. Rev.* **58,** 1379–1408 (2006).

28. Park, N., Um, S. H., Funabashi, H., Xu, J. & Luo, D. A cell-free protein-producing gel. *Nat. Mater.* **8,** 432–437 (2009).

29. Niederholtmeyer, H., Chaggan, C. & Devaraj, N. K. Communication and quorum sensing in non-living mimics of eukaryotic cells. *Nat. Commun.* **9,** 1–8 (2018).

30. Lai, S. N. *et al.* Artificial Cells Capable of Long-Lived Protein Synthesis by Using Aptamer Grafted Polymer Hydrogel. *ACS Synth. Biol.* **9,** 76–83 (2020).

31. Spoelstra, W. K., Deshpande, S. & Dekker, C. Tailoring the appearance: what will synthetic cells look like? *Curr. Opin. Biotechnol.* **51,** 47–56 (2018).

32. Donau, C. *et al.* Active coacervate droplets as a model for membraneless organelles and protocells. *Nat. Commun.* **11,** 1–10 (2020).

33. Mason, A. F., Buddingh, B. C., Williams, D. S. & Hest, J. C. V. Hierarchical Self-Assembly of a Copolymer-Stabilized Coacervate Protocell. *J. Am. Chem. Soc.* **139,** 17309–17312 (2017).
34. Deshpande, S. *et al.* Spatiotemporal control of coacervate formation within liposomes. *Nat. Commun.* **10,** 1–11 (2019).
35. Altenburg, W. J. *et al.* Programmed spatial organization of biomacromolecules into discrete, coacervate-based protocells. *Nat. Commun.* **11,** 1–10 (2020).
36. Huang, X., Li, M. & Mann, S. Membrane-mediated cascade reactions by enzyme-polymer proteinosomes. *Chem. Commun.* **50,** 6278–6280 (2014).
37. Qiao, Y., Li, M., Booth, R. & Mann, S. Predatory behaviour in synthetic protocell communities. *Nat. Chem.* **9,** 110–119 (2017).
38. Liu, X. *et al.* Hierarchical Proteinosomes for Programmed Release of Multiple Components. *Angew. Chem. Int. Ed.* **55,** 7095–7100 (2016).
39. Gobbo, P. *et al.* Programmed assembly of synthetic protocells into thermoresponsive prototissues. *Nat. Mater.* **17,** 1145–1153 (2018).
40. Discher, D. E. & Eisenberg, A. Polymer vesicles. *Science* **297,** 967–973 (2002).
41. Belluati, A., Craciun, I., Meyer, C. E., Rigo, S. & Palivan, C. G. Enzymatic reactions in polymeric compartments: nanotechnology meets nature. *Curr. Opin. Biotechnol.* **60,** 53–62 (2019).
42. Chiu, H.-C., Lin, Y.-W., Huang, Y.-F., Chuang, C.-K. & Chern, C.-S. Polymer Vesicles Containing Small Vesicles within Interior Aqueous Compartments and pH-Responsive Transmembrane Channels. *Angew. Chem. Int. Ed.* **47,** 1875–1878 (2008).
43. Peters, R. J. *et al.* Cascade reactions in multicompartmentalized polymersomes. *Angew. Chem. Int. Ed.* **53,** 146–150 (2014).
44. Shum, H. C., Zhao, Y.-j., Kim, S.-H. & Weitz, D. A. Multicompartment Polymersomes from Double Emulsions. *Angew. Chem. Int. Ed.* **50,** 1648–1651 (2011).
45. Belluati, A. *et al.* Multicompartment Polymer Vesicles with Artificial Organelles for Signal-Triggered Cascade Reactions Including Cytoskeleton Formation. *Adv. Funct. Mater.* **30,** 2002949 (2020).
46. Kamat, N. P., Katz, J. S. & Hammer, D. A. Engineering polymersome protocells. *J. Phys. Chem. Lett.* **2,** 1612–1623 (2011).
47. Song, L. *et al.* Structure of staphylococcal α-hemolysin, a heptameric transmembrane pore. *Science* **274,** 1859–1866 (1996).
48. Cruickshank, C. C., Minchin, R. F., Dain, A. C. L. & Martinac, B. Estimation of the pore size of the large-conductance mechanosensitive ion channel of Escherichia coli. *Biophys. J.* **73,** 1925 (1997).
49. Chang, G., Spencer, R. H., Lee, A. T., Barclay, M. T. & Rees, D. C. Structure of the MscL Homolog from Mycobacterium tuberculosis: A Gated Mechanosensitive Ion Channel. *Science* **282,** 2220–2226 (1998).
50. Henderson, R. The structure of the purple membrane from Halobacterium hallobium: analysis of the X-ray diffraction pattern. *J. Mol. Biol.* **93** (1975).

51. Grigorieff, N., Ceska, T. A., Downing, K. H., Baldwin, J. M. & Henderson, R. Electron-crystallographic Refinement of the Structure of Bacteriorhodopsin. *J. Mol. Biol.* **259,** 393–421 (1996).
52. Onaca, O., Nallani, M., Ihle, S., Schenk, A. & Schwaneberg, U. Functionalized nanocompartments (Synthosomes): Limitations and prospective applications in industrial biotechnology. *Biotechnol. J.* **1,** 795–805 (2006).
53. Alberts, B. *et al. The Lipid Bilayer* 2002.
54. Elani, Y., Law, R. V. & Ces, O. Protein synthesis in artificial cells: Using compartmentalisation for spatial organisation in vesicle bioreactors. *Phys. Chem. Chem. Phys.* **17,** 15534–15537 (2015).
55. Peyret, A., Ibarboure, E., Pippa, N. & Lecommandoux, S. Liposomes in Polymersomes: Multicompartment System with Temperature-Triggered Release. *Langmuir* **33,** 7079–7085 (2017).
56. Gao, W. *et al.* Hydrogel containing nanoparticle-stabilized liposomes for topical antimicrobial delivery. *ACS Nano* **8,** 2900–2907 (2014).
57. Lee, K. Y. *et al.* Photosynthetic artificial organelles sustain and control ATP-dependent reactions in a protocellular system. *Nat. Biotechnol.* **36,** 530–535 (2018).
58. Simmel, F. C. Synthetic organelles. *Emerg. Top. Life Sci.* **3,** 587–595 (2019).
59. Sawant, R. R. & Torchilin, V. P. Multifunctionality of lipid-core micelles for drug delivery and tumour targeting. *Mol. Membr. Biol.* **27,** 232–246 (2010).
60. Akbarzadeh, A. *et al.* Liposome: Classification, preparation, and applications. *Nanoscale Res. Lett.* **8,** 102 (2013).
61. Jesorka, A. & Orwar, O. Liposomes: Technologies and Analytical Applications. *Annual Review of Analytical Chemistry* **1,** 801–832 (2008).
62. Au, J. L., Yeung, B. Z., Wientjes, M. G., Lu, Z. & Wientjes, M. G. Delivery of cancer therapeutics to extracellular and intracellular targets: Determinants, barriers, challenges and opportunities. *Adv. Drug Deliv. Rev.* **97,** 280–301 (2016).
63. Polack, F. P. *et al.* Safety and Efficacy of the BNT162b2 mRNA Covid-19 Vaccine. *N. Engl. J. Med.* **383,** 2603–2615 (2020).
64. Baden, L. R. *et al.* Efficacy and Safety of the mRNA-1273 SARS-CoV-2 Vaccine. *N. Engl. J. Med.* **384,** 403–416 (2021).
65. Reichmuth, A. M., Oberli, M. A., Jeklenec, A., Langer, R. & Blankschtein, D. mRNA vaccine delivery using lipid nanoparticles. *Ther. Deliv.* **7,** 319–334 (2016).
66. Cooper, G. M. *Endocytosis* 2000.
67. Berhanu, S., Ueda, T. & Kuruma, Y. Artificial photosynthetic cell producing energy for protein synthesis. *Nat. Commun.* **10,** 1–10 (2019).
68. Deng, N. N. & Huck, W. T. S. Microfluidic Formation of Monodisperse Coacervate Organelles in Liposomes. *Angew. Chemie - Int. Ed.* (2017).
69. Deng, N. N., Yelleswarapu, M., Zheng, L. & Huck, W. T. Microfluidic assembly of monodisperse vesosomes as artificial cell models. *J. Am. Chem. Soc.* **139,** 587–590 (2017).

70. Hindley, J. W. *et al.* Building a synthetic mechanosensitive signaling pathway in compartmentalized artificial cells. *Proc. Natl Acad. Sci. USA* **116,** 16711–16716 (2019).

71. Thomas, J. M., Friddin, M. S., Ces, O. & Elani, Y. Programming membrane permeability using integrated membrane pores and blockers as molecular regulators. *Chem. Commun.* **53,** 12282–12285 (2017).

72. Ladokhin, A. S., Selsted, M. E. & White, S. H. Sizing membrane pores in lipid vesicles by leakage of co-encapsulated markers: Pore formation by melittin. *Biophys. J.* **72,** 1762–1766 (1997).

73. Deng, N.-N., Yelleswarapu, M. & Huck, W. T. S. Monodisperse Uni- and Multicompartment Liposomes. *J. Am. Chem. Soc.* **138,** 7584–7591 (2016).

74. Haswell, E. S., Phillips, R. & Rees, D. C. Mechanosensitive channels: What can they do and how do they do it? *Structure* **19,** 1356–1369 (2011).

75. Kocer, A., Walko, M., Meijberg, W. & Feringa, B. L. A light-actuated nanovalve derived from a channel protein. *Science* **309,** 755–758 (2005).

76. Van Den Bogaart, G., Krasnikov, V. & Poolman, B. Dual-color fluorescence-burst analysis to probe protein efflux through the mechanosensitive channel MscL. *Biophys. J.* **92,** 1233–1240 (2007).

77. Berendes, R., Burger, A., Voges, D., Demange, P. & Huber, R. Calcium influx through annexin V ion channels into large unilamellar vesicles measured with fura-2. *FEBS Lett.* **317,** 131–134 (1993).

78. Aimon, S. *et al.* Functional Reconstitution of a Voltage-Gated Potassium Channel in Giant Unilamellar Vesicles. *PLOS ONE* **6,** e25529 (2011).

79. Kahya, N., Pecheur, E. I., Boeij, W. P. D., Wiersma, D. A. & Hoekstra, D. Reconstitution of membrane proteins into giant unilamellar vesicles via peptide-induced fusion. *Biophys. J.* **81,** 1464–1474 (2001).

80. Girard, P. *et al.* A new method for the reconstitution of membrane proteins into giant unilamellar vesicles. *Biophys. J.* **87,** 419–429 (2004).

81. Dezi, M., Cicco, A. D., Bassereau, P. & Levy, D. Detergent-mediated incorporation of transmembrane proteins in giant unilamellar vesicles with controlled physiological contents. *PNAS* **110,** 7276–7281 (2013).

82. Fujii, S., Matsuura, T., Sunami, T., Kazuta, Y. & Yomo, T. In vitro evolution of alpha-hemolysin using a liposome display. *PNAS* **110,** 16796–16801 (2013).

83. Muraoka, T. *et al.* A synthetic ion channel with anisotropic ligand response. *Nat. Commun.* **11,** 1–9 (2020).

84. Vorobieva, A. A. *et al.* De novo design of transmembrane β barrels. *Science* **371** (2021).

85. Feng, X., Jia, Y., Cai, P., Fei, J. & Li, J. Coassembly of photosystem II and ATPase as Artificial chloroplast for light-driven ATP synthesis. *ACS Nano* **10,** 556–561 (2016).

86. Toparlak, D. *et al.* Artificial cells drive neural differentiation. *Sci. Adv.* **6,** 4920–4938 (2020).

87. Chen, Z. *et al.* Synthetic beta cells for fusion-mediated dynamic insulin secretion. *Nat. Chem. Biol.* **14,** 86–93 (2018).

88. Adamala, K. P., Martin-Alarcon, D. A., Guthrie-Honea, K. R. & Boyden, E. S. Engineering genetic circuit interactions within and between synthetic minimal cells. *Nature Chemistry* **9,** 431–439 (2017).

89. Rampioni, G., DAngelo, F., Leoni, L. & Stano, P. Gene-expressing liposomes as synthetic cells for molecular communication studies. *Front. Bioeng. Biotechnol.* **7,** 1 (2019).

90. Buddingh, B. C. & van Hest, J. C. M. Artificial Cells: Synthetic Compartments with Life-like Functionality and Adaptivity. *Acc. Chem. Res* **50,** 769–777 (2017).

91. Kretschmer, S., Ganzinger, K. A., Franquelim, H. G. & Schwille, P. Synthetic cell division via membrane-transforming molecular assemblies. *BMC Biology* **17,** 1–10 (2019).

92. Pan, J. *et al.* Mimicking Chemotactic Cell Migration with DNA Programmable Synthetic Vesicles. *Nano Lett.* **19,** 9138–9144 (2019).

93. Dupin, A. & Simmel, F. C. Signalling and differentiation in emulsion-based multi-compartmentalized in vitro gene circuits. *Nat. Chem.* **11,** 32–39 (2019).

94. Villar, G., Graham, A. D. & Bayley, H. A tissue-like printed material. *Science* **340,** 48–52 (2013).

95. Holden, M. A., Needham, D. & Bayley, H. Functional Bionetworks from Nanoliter Water Droplets. *J. Am. Chem. Soc.* **129,** 8650–8655 (2007).

96. Booth, M. J., Schild, V. R., Box, S. J. & Bayley, H. Light-patterning of synthetic tissues with single droplet resolution. *Sci. Rep.* **7,** 9315 (2017).

97. Tamaddoni, N., Freeman, E. C. & Sarles, S. A. Sensitivity and directionality of lipid bilayer mechanotransduction studied using a revised, highly durable membrane-based hair cell sensor. *Smart Mater. Struct.* **24,** 065014 (2015).

98. Booth, M. J., Schild, V. R., Downs, F. G. & Bayley, H. Functional aqueous droplet networks. *Molecular BioSystems* **13,** 1658–1691 (2017).

99. Alcinesio, A. *et al.* Controlled packing and single-droplet resolution of 3D-printed functional synthetic tissues. *Nat. Commun.* **11,** 1–13 (2020).

100. Maglia, G. *et al.* Droplet networks with incorporated protein diodes show collective properties. *Nature Nanotechnology* **4,** 437–440 (2009).

101. Wauer, T. *et al.* Construction and Manipulation of Functional Three-Dimensional Droplet Networks. *ACS Nano* **8,** 771–779 (2014).

102. Booth, M. J., Schild, V. R., Graham, A. D., Olof, S. N. & Bayley, H. Light-activated communication in synthetic tissues. *Sci. Adv.* **2,** e1600056 (2016).

103. Haylock, S. *et al.* Membrane protein mediated bilayer communication in networks of droplet interface bilayers. *Commun. Chem.* **3,** 1–8 (2020).

104. Findlay, H. E., Harris, N. J. & Booth, P. J. In vitro synthesis of a Major Facilitator Transporter for specific active transport across Droplet Interface Bilayers. *Sci. Rep.* **6,** 1–9 (2016).

105. Yasuga, H. *et al.* Logic Gate Operation by DNA Translocation through Biological Nanopores. *PLOS ONE* **11,** e0149667 (2016).

106. Syeda, R., Holden, M. A., Hwang, W. L. & Bayley, H. Screening blockers against a potassium channel with a droplet interface bilayer array. *J. Am. Chem. Soc.* **130,** 15543–15548 (2008).

107. Syeda, R., Santos, J. S., Montal, M. & Bayley, H. Tetrameric assembly of KvLm K+ channels with defined numbers of voltage sensors. *Proc. Natl. Acad. Sci.* **109,** 16917–16922 (2012).

108. Tamaddoni, N. & Sarles, S. A. Toward cell-inspired materials that feel: Measurements and modeling of mechanotransduction in droplet-based, multi-membrane arrays. *Bioinspir. Biomim.* **11,** 36008 (2016).

109. Najem, J. S. *et al.* Activation of bacterial channel MscL in mechanically stimulated droplet interface bilayers. *Sci. Rep.* **5,** 1–11 (2015).

110. Mantripragada, S. A lipid based depot (DepoFoam® technology) for sustained release drug delivery. *Prog. Lipid Res.* (2002).

111. Elani, Y., Solvas, X. C. I., Edel, J. B., Law, R. V. & Ces, O. Microfluidic generation of encapsulated droplet interface bilayer networks (multisomes) and their use as cell-like reactors. *Chem. Commun.* **52,** 5961–5964 (2016).

112. Booth, M. J., Cazimoglu, I. & Bayley, H. Controlled deprotection and release of a small molecule from a compartmented synthetic tissue module. *Commun. Chem.* **2,** 1–8 (2019).

113. Braha, O. *et al.* Designed protein pores as components for biosensors. *Chem. Biol.* **4,** 497–505 (1997).

114. Elani, Y., Gee, A., Law, R. V. & Ces, O. Engineering multi-compartment vesicle networks. *Chem. Sci.* **4,** 3332–3338 (2013).

115. Elani, Y., Law, R. V. & Ces, O. Vesicle-based artificial cells as chemical microreactors with spatially segregated reaction pathways. *Nat. Commun.* **5,** 1–5 (2014).

116. Asthagiri, A. R. & Lauffenburger, D. A. Bioengineering Models of Cell Signaling. *Annu. Rev. Biomed. Eng.* **2,** 31–53 (2000).

117. Kholodenko, B. N. Cell-signalling dynamics in time and space. *Nat. Rev. Mol. Cell Biol.* **7,** 165–176 (2006).

118. Purvis, J. E. & Lahav, G. Encoding and decoding cellular information through signaling dynamics. *Cell* **152,** 945–956 (2013).

119. Bhakdi, S. & Tranum-Jensen, J. Alpha-toxin of Staphylococcus aureus. *Microbiol. Mol. Biol. Rev.* **55** (1991).

120. Gouaux, J. E. *et al.* Subunit stoichiometry of staphylococcal α-hemolysin in crystals and on membranes: A heptameric transmembrane pore. *Proc. Natl. Acad. Sci. USA* **91,** 12828–12831 (1994).

121. Keller, S., Heerklotz, H., Jahnke, N. & Blume, A. Thermodynamics of Lipid Membrane Solubilization by Sodium Dodecyl Sulfate. *Biophys. J.* **90,** 4509 (2006).

122. Ahyayauch, H., Bennouna, M., Alonso, A. & Goni, F. M. Detergent Effects on Membranes at Subsolubilizing Concentrations: Transmembrane Lipid Motion, Bilayer Permeabilization, and Vesicle Lysis/Reassembly Are Independent Phenomena. *Langmuir* **26,** 7307–7313 (2010).

123. Praper, T. *et al.* Human Perforin Employs Different Avenues to Damage Membranes. *J. Biol. Chem.* **286,** 2946 (2011).

124. Gilbert, R. J., Serra, M. D., Froelich, C. J., Wallace, M. I. & Anderluh, G. Membrane pore formation at protein–lipid interfaces. *Trends Biochem. Sci.* **39,** 510–516 (2014).

125. Rojko, N. & Anderluh, G. How Lipid Membranes Affect Pore Forming Toxin Activity. *Acc. Chem. Res.* **48,** 3073–3079 (2015).

126. Dudek, G. & Borys, P. A Simple Methodology to Estimate the Diffusion Coefficient in Pervaporation-Based Purification Experiments. *Polymers* **11** (2019).

127. Ribeiro, A. C. F. *et al.* Binary Mutual Diffusion Coefficients of Aqueous Solutions of Sucrose, Lactose, Glucose, and Fructose in the Temperature Range from (298.15 to 328.15) K. *J. Chem. Eng. Data* **51,** 1836–1840 (2006).

128. Elfaramawy, M. A. *et al.* Quantitative analysis of cell-free synthesized membrane proteins at the stabilized droplet interface bilayer. *Chem. Comm.* **54,** 12226–12229 (2018).

129. Stefureac, R., Long, Y. T., Kraatz, H. B., Howard, P. & Lee, J. S. Transport of α-helical peptides through α-hemolysin and aerolysin pores. *Biochemistry* **45,** 9172–9179 (2006).

130. Rosano, G. L. & Ceccarelli, E. A. Recombinant protein expression in Escherichia coli: Advances and challenges. *Front. Microbiol.* **5** (2014).

131. Invitrogen. *Molecular Probes 11th Edition* <https://www.thermofisher.com/it/en/home/global/forms/mp-handbook-download-request-form-2014.html> (2010).

132. Bioquest, A. *Rhod-2 dextran conjugate *Low affinity with MW 10,000** <https://www.thermofisher.com/it/en/home/global/forms/mp-handbook-download-request-form-2014.html> (2020).

133. Pingoud, V. *et al.* On the Divalent Metal Ion Dependence of DNA Cleavage by Restriction Endonucleases of the EcoRI Family. *J. Mol. Biol.* **393,** 140–160 (2009).

134. Kaur, A., Kaur, P. & Ahuja, S. Förster resonance energy transfer (FRET) and applications thereof. *Anal. Methods* **12,** 5532–5550 (2020).

135. May, J. P., Brown, L. J., Rudloff, I. & Brown, T. A new dark quencher for use in genetic analysis. *Chem. Commun.* **3,** 970–971 (2003).

136. Yang, C. J., Li, J. J. & Tan, W. *Using molecular beacons for sensitive fluorescence assays of the enzymatic cleavage of nucleic acids* 2006.

137. Marras, S. A. *Selection of fluorophore and quencher pairs for fluorescent nucleic acid hybridization probes* 2006.

138. Johansson, M. K. *Choosing reporter-quencher pairs for efficient quenching through formation of intramolecular dimers.* 2006.

139. Johansson, M. K., Fidder, H., Dick, D. & Cook, R. M. Intramolecular dimers: A new strategy to flourescence quenching in dual-labeled oligonucleotide probes. *J. Am. Chem. Soc.* **124,** 6950–6956 (2002).

140. Lakowicz, J. R. *Quenching of Fluorescence* 2006.

141. Biolabs, N. E. *Recombinant Albumin, Molecular Biology Grade* <www.neb.com/BSA-free> (2021).

142. Spector, A. A., Fletcher, J. E. & Ashbrook, J. D. Analysis of Long-Chain Free Fatty Acid Binding to Bovine Serum Albumin by Determination of Stepwise Equilibrium Constants. *Biochemistry* **10,** 3229–3232 (1971).

143. Alsabeeh, N., Chausse, B., Kakimoto, P. A., Kowaltowski, A. J. & Shirihai, O. Cell culture models of fatty acid overload: Problems and solutions. *Biochim. Biophys. Acta Mol. Cell Biol. Lipids* **1863,** 143–151 (2018).

144. Richmond, M. L., Gray, J. I. & Stine, C. M. Beta-Galactosidase: Review of Recent Research Related to Technological Application, Nutritional Concerns, and Immobilization I. *J. Dairy Sci.* **64,** 1759–1771 (1981).

145. Saqib, S., Akram, A., Halim, S. A. & Tassaduq, R. Sources of β-galactosidase and its applications in food industry. *3 Biotech* **7** (2017).

146. Yu Chang, C., Niblack, B., Walker, B. & Bayley, H. A photogenerated pore-forming protein. *Chem. Biol.* **2,** 391–400 (1995).

147. Walker, B., Kasianowicz, J., Krishnasastry, M. & Bayley, H. A pore-forming protein with a metal-actuated switch. *Protein Eng. Des. Sel.* **7,** 655–662 (1994).

148. Walker, B. & Bayley, H. A pore-forming protein with a protease-activated trigger. *Protein Eng.* **7,** 91–97 (1994).

149. Koo, S., Cheley, S. & Bayley, H. Redirecting Pore Assembly of Staphylococcal α-Hemolysin by Protein Engineering. *ACS Cent. Sci.* **5,** 629–639 (2019).

150. Strutt, R. *et al.* Activating mechanosensitive channels embedded in droplet interface bilayers using membrane asymmetry. *Chem. Sci.* **12,** 2138–2145 (2021).

151. Birkner, J. P., Poolman, B. & Kocer, A. Hydrophopic gating of mechanosensitive channel of large conductance evidenced by single-subunit resolution. *Proc. Natl. Acad. Sci. U. S. A* **109,** 12944–12949 (2012).

152. Punnamaraju, S., You, H. & Steckl, A. J. Triggered Release of Molecules across Droplet Interface Bilayer Lipid Membranes Using Photopolymerizable Lipids. *Langmuir* **28,** 7657–7664 (2012).

153. Makhoul-Mansour, M. M., El-Beyrouthy, J. B., Mumme, H. L. & Freeman, E. C. Photopolymerized microdomains in both lipid leaflets establish diffusive transport pathways across biomimetic membranes. *Soft Matter* **15,** 8718–8727 (2019).

154. Czekalska, M. A. *et al.* One-Step Generation of Multisomes from Lipid-Stabilized Double Emulsions. *ACS Appl. Mater. Interfaces* **13,** 6739–6747 (2021).

155. Cazimoglu, I., Booth, M. J. & Bayley, H. A Lipid-Based Droplet Processor for Parallel Chemical Signals. *ACS Nano* (2021).